Large eddy simulation of dual-fuel combustion under ICE conditions

Xu, Shijie

2021

Document Version:
Early version, also known as pre-print

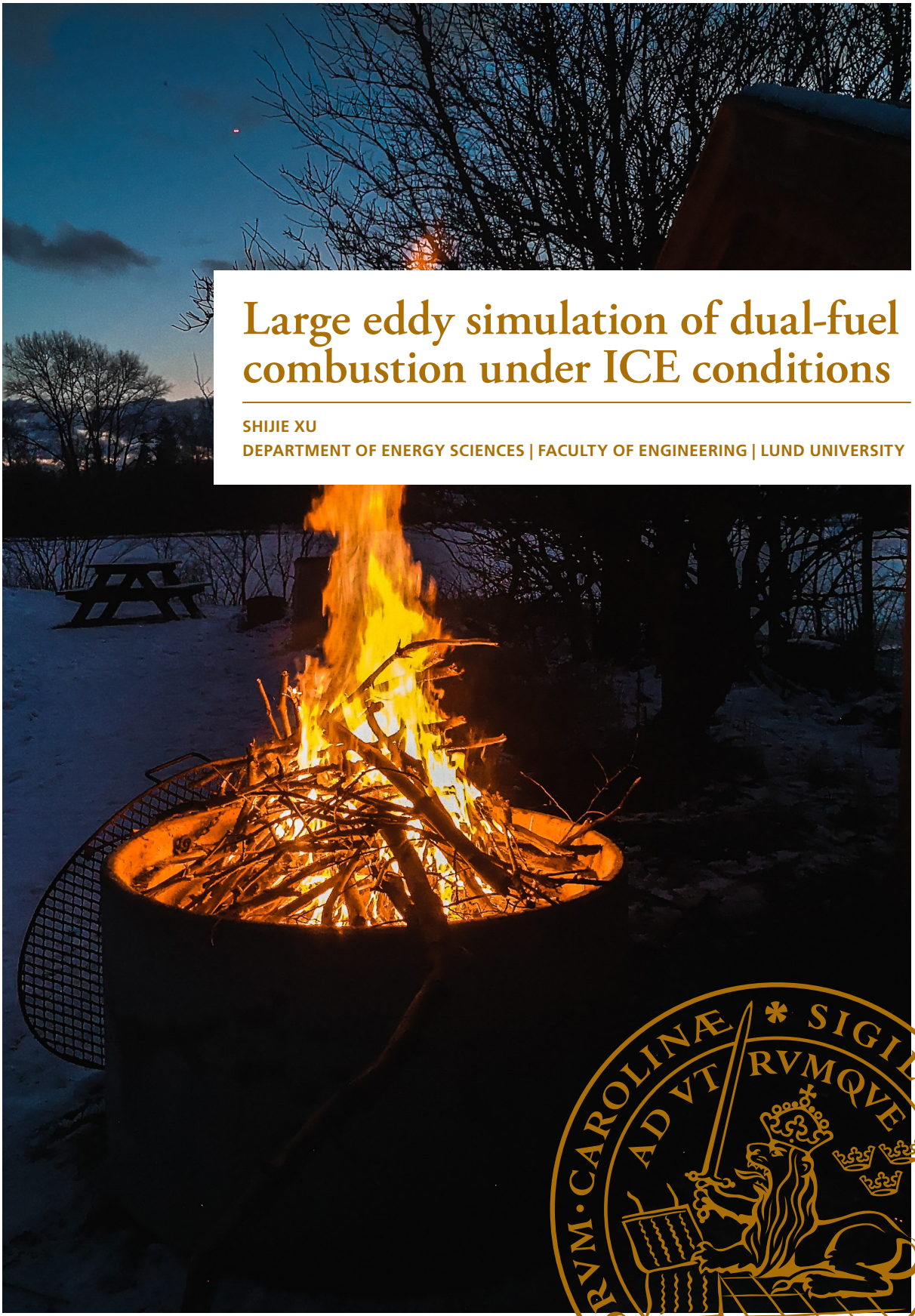

Large eddy simulation of dual-fuel combustion under ICE conditions

SHIJIE XU
DEPARTMENT OF ENERGY SCIENCES | FACULTY OF ENGINEERING | LUND UNIVERSITY

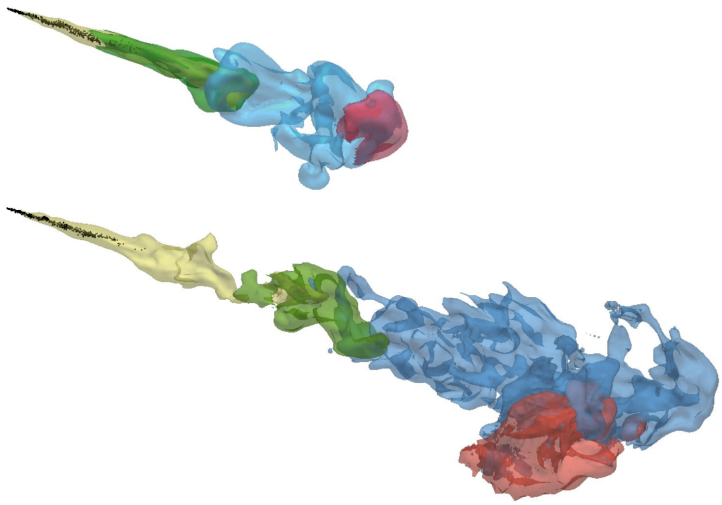

Dual-fuel combustion is a promising concept as it is in favor of some alternative fuels utilisation and has potential to reduce pollutant emissions. In this thesis, high-fidelity methods for the simulation of turbulence and combustion are used to study the single- and dual-fuel combustion.

Printed by Media-Tryck, Lund 2021 NORDIC SWAN ECOLABEL 3041 0903

LUND UNIVERSITY

Division of Fluid Mechanics
Department of Energy Sciences

ISBN: 978-91-7895-882-5
ISSN: 0282-1990
ISRN: LUTMDN/TMHP-19/1165-SE

9 789178 958825

Large eddy simulation of dual-fuel combustion under ICE conditions

Large eddy simulation of dual-fuel combustion under ICE conditions

by Shijie Xu

LUND
UNIVERSITY

Thesis for the degree of Doctor of Philosophy
Thesis advisors: Prof. Xue-Song Bai, Dr. Hesameddin Fatehi, and Dr. Kar Mun Pang
Faculty opponent: Prof. Ville Vuorinen, Aalto University

To be presented, with the permission of the Faculty of Engineering of Lund University, for public criticism in the Rudolf room at the Department of Energy Sciences on Monday, the 30th of August 2021 at 09:00.

Organization
LUND UNIVERSITY

Department of Energy Sciences
P.O. Box 118, SE–221 00 LUND
Sweden

Document name
DOCTORAL DISSERTATION

Date of disputation
2021-08-30

Sponsoring organization
China Scholarship Council (CSC), Swedish Research Council (VR), Swedish Energy Agency (STEM) through CECOST and KCFP, Swedish National Infrastructure for Computing (SNIC)

Author(s)
Shijie Xu

Title and subtitle
Large eddy simulation of dual-fuel combustion under ICE conditions

Abstract
The present thesis aims at studying n-heptane/methanol dual-fuel combustion under internal combustion engine conditions and strives to improve the understanding of its ignition, combustion, and pollutant emission mechanisms. Large-eddy simulation (LES) coupled with Eulerian stochastic fields (ESF) approach is employed to simulate single/dual-fuel combustion in a constant-volume vessel to mimic the single/dual-fuel combustion in conventional/dual-fuel premixed engines. The experimental configuration from Engine Combustion Network (ECN) is considered as the baseline case in the simulations. The main works are summarized in two parts: model development and studies of the fundamental physics involved in dual-fuel combustion. First, the ESF approach with a novel modified method is proposed, implemented, and evaluated. Results show that the modified ESF method removes the numerical error in the element mass conservation and shows capability in predicting both premixed and non-premixed flames relevant to dual-fuel combustion. Second, LES of n-heptane single-fuel and n-heptane/methanol dual-fuel combustion is carried out and validated against ECN Spray-H experiments. A good agreement is obtained in terms of flow, combustion, and emissions characteristics. Finally, a parameter study is performed to investigate the effects of the dual-fuel strategies, including the primary fuel concentration, the ambient temperature, and the pilot fuel injection timing. It is concluded that: 1) The ambient methanol is found to have an effect of suppressing the two-stage ignition and heat release of n-heptane, this is more significant under high ambient methanol concentration conditions. 2) The effects of methanol on the n-heptane ignition and NOx formation are strongly dependent on the ambient temperatures. The retardation of the n-heptane high temperature ignition is more remarkable under low ambient temperatures. The NOx and soot in the dual-fuel case is lower than that of the single-fuel case in moderately high initial temperatures, while an opposite trend is observed in higher temperatures. 3) A late injection may lead to an overlap of the ambient methanol auto-ignition and the delivery of n-heptane. This overlap results in high soot and NOx formation.

Key words
Turbulent combustion, transported probability density function, dual-fuel, spray

Classification system and/or index terms (if any)

Supplementary bibliographical information

Language
English

ISSN and key title
0282-1990

ISBN
978-91-7895-882-5 (print)
978-91-7895-881-8 (pdf)

Recipient's notes

Number of pages
288

Price

Security classification

Large eddy simulation of dual-fuel combustion under ICE conditions

by Shijie Xu

LUND
UNIVERSITY

A doctoral thesis at a university in Sweden takes either the form of a single, cohesive research study (monograph) or a summary of research papers (compilation thesis), which the doctoral student has written alone or together with one or several other author(s).

In the latter case the thesis consists of two parts. An introductory text puts the research work into context and summarizes the main points of the papers. Then, the research publications themselves are reproduced, together with a description of the individual contributions of the authors. The research papers may either have been already published or are manuscripts at various stages (in press, submitted, or in draft).

Cover illustration front: "Low temperature" combustion, photographed at Rögle Dammar in February of 2021 (Credits: Michael Bertsch and Thommie Nilsson).

Cover illustration back: An illustration of three-dimensional single- (upper) and dual-fuel (bottom) flame structures (See Paper I).

Funding information: The thesis work was financially supported by the China Scholarship Council (CSC), Swedish Research Council (VR), and Swedish Energy Agency (STEM) through CECOST and KCPF. The computational resources were provided by the Swedish National Infrastructure for Computing (SNIC at NSC, HPC2N, and PDC).

Faculty of Engineering, Department of Energy Sciences

ISBN: 978-91-7895-882-5 (print)
ISBN: 978-91-7895-881-8 (pdf)
ISSN: 0282-1990
ISRN: LUTMDN/TMHP-19/1165-SE

Printed in Sweden by Media-Tryck, Lund University, Lund 2021

Contents

List of publications

I **LES/TPDF investigation of the effects of ambient methanol concentration on pilot fuel ignition characteristics and reaction front structures.**
Shijie Xu*, Kar Mun Pang, Yaopeng Li, Ahmad Hadadpour, Senbin Yu, Shenghui Zhong, Mehdi Jangi, Xue-Song Bai.
Fuel, 2021, 287: 119502.

II **Effects of ambient methanol on pollutants formation in dual-fuel spray combustion at varying ambient temperatures: A large-eddy simulation.**
Shijie Xu*, Shenghui Zhong, Kar Mun Pang, Senbin Yu, Mehdi Jangi, Xue-Song Bai.
Applied Energy, 2020, 279: 115774.

III **Large-eddy simulation of the injection timing effects on the dual-fuel spray flame.**
Shijie Xu, Shenghui Zhong, Ahmad Hadadpour, Yan Zhang, Kar Mun Pang, Mehdi Jangi, Xue-Song Bai*.
Manuscript for journal submission.

IV **On the element mass conservation in Eulerian stochastic field modelling of turbulent combustion.**
Shijie Xu, Shenghui Zhong, Fan Zhang, Xue-Song Bai*.
Combustion and Flame, Under review.

V **Effects of pre-injection on ignition, combustion and emissions of spray under engine-like conditions.**
Ahmad Hadadpour, **Shijie Xu**, Kar Mun Pang, Xue-Song Bai*, Mehdi Jangi.
Combustion and Flame, Under review.

Publications not included in this thesis:

i **Modeling of ammonia solution spray and mixing in selective catalytic reduction (SCR) system.**
Shijie Xu*, Xue-Song Bai, Yaopeng Li, Leilei Xu, Peter Larsson, Per Tunestål
International Conference on Applied Energy, 2019.

ii **Large eddy simulation of spray combustion using flamelet generated manifolds combined with artificial neural networks.**
Yan Zhang, **Shijie Xu**, Shenghui Zhong, Xue-Song Bai, Hu Wang, Mingfa Yao*.
Energy and AI, 2020, 2: 100021.

iii **Combustion characteristics of n-heptane spray combustion in a low temperature reforming gas/air environment.**
Shenghui Zhong, **Shijie Xu**, Xue-Song Bai*, Ahmad Hadadpour, Mehdi Jangi, Fan Zhang, Qing Du, Zhijun Peng*.
Fuel, 2021, 293: 120377.

iv **Large eddy simulation of n-heptane/syngas pilot ignition spray combustion: ignition process, liftoff evolution and pollutant emissions.**
Shenghui Zhong, **Shijie Xu**, Xue-Song Bai*, Zhijun Peng, Fan Zhang*.
Energy, Accepted.

v **Effects of ambient pressure and nozzle diameter on ignition characteristics in diesel spray combustion.**
Jiun Cai Ong*, Jens Honore Walther, **Shijie Xu**, Shenghui Zhong, Xue-Song Bai, Kar Mun Pang.
Fuel, 2021, 290: 119887.

vi **Comparison of Kinetic Mechanisms for Numerical Simulation of Methanol Combustion in DICI Heavy-Duty Engine.**
Mateusz Pucilowski, Rui Li, **Shijie Xu**, Changle Li, Fei Qin, Martin Tuner, Xue-Song Bai*, Alexander A Konnov.
SAE, 2019: 2019-01-0208.

Acknowledgements

This work was sponsored by the Swedish Research Council (VR), Swedish Energy Agency through CECOST and KCFP. The candidate was sponsored by the China Scholarship Council (CSC). The computational resources were provided by the Swedish National Infrastructure for Computing (SNIC).

I would like to express my gratitude to my main supervisor Prof. Xue-Song Bai for all supports in my studies and work. He brought me to the field of numerical simulations and inspired me to think over scientific questions as a researcher. I also benefited from his life experience and attitude toward life. My gratitude also goes to Dr. Kar Mun Pang for his valuable advice, patient discussion, and encouragement; to Dr. Hesameddin Fatehi, Dr. Rixin Yu, and Dr. Robert-Zoltán Szász for their valuable discussions on fluid dynamics; to Prof. Johan Revstedt and Prof. Christer Fureby for their interesting courses; to Dr. Ahmad Hadadpour, Shenghui Zhong, Yan Zhang, Dr. Yaopeng Li, Dr. Mateusz Pucilowski, Dr. Jiun Cai Ong, and Dr. Mehdi Jangi for their great collaborations; to Johan Lorentzon and Mark Treacy for reading the manuscript of this thesis. It was my pleasure to work with you and learn from you.

I would like to express my great thanks to my colleagues and friends, your presence made my Ph.D. study life rich and colorful. Thank Senbin Yu, Miao Zhang, Jian Liu, Miao Yang and Michael Bertsch for organising activities, cycling, skiing, and BBQ with you are fun. To Morteza Mousavi, Li Guo, Haoran Zhao, Christian Ibron, Peibo Li, Shijie Liu, Wei Wang, Xiufei Li, Yuanxin Qi and Erik Bolin, Zhen Cao, Rui Li, Jian Wu, Zhenkan Wang, Wubin Weng, Xin Liu and Qingshuang Fan, thank you for all the help, talk, and fun times. I would like to give my special thanks to Leilei Xu, we were room mate and office mate treating each other like brothers. His help comes in many ways, not only in work and life. I will never forget precious memories with him and his family, Yang Liu, Alisa and aunt. Special thanks also go to my office mates, Thommie Nilsson and Francesco Pignatelli, for all interesting discussions. I would also like to acknowledge Prof. Magnus Genrup, Catarina Lindén, Isabelle Frej, Julia Hansson, Gity Yahoo, and Sara Månsson for creating a nice work environment.

Last, but not least, I am grateful to my family. To my beloved wife Yuanyuan Cao, thank you for your support, efforts, and patience. You are in another country, but your love could travel thousands of miles. None of this would have been possible without you. To my parents, aunts, and grandparents, thank you for your love, support, and encouragements throughout my life. Special thanks to my grandfather, he is the lighthouse guiding me ahead.

Popular science summary

The internal combustion engine (ICE) is an important energy conversion machine, which has been widely used in cars, ships, and aircraft. In the ICE the fuel is combusted with air to produce heat, which gives rise to hot gas expansion that drives the piston to move reciprocatively and thereby provides power to the vehicles. Currently, gasoline and diesel are the common fuels for ICE, which are known as fossil fuels. On the one hand, fossil fuel consumption is not sustainable due to limited resources, and on the other hand, fossil fuel combustion produces pollutants such as NOx, soot particles, CO and unburned hydrocarbon that are harmful to the environment. Furthermore, fossil fuel combustion generates greenhouse gas CO_2 emissions that lead to global warming. In 2020, as a consequence of the confinement due to the COVID-19 pandemic, the slump in road transport activity accounted for 50% of the decline in global oil demand, and the drop in aviation for around 35%. In addition, the global carbon dioxide emissions from surface transport fell by 36% by April 2020 and made the largest contribution to the total emissions change. This is interesting data showing that the transportation sector has great potential to reduce fossil fuels usage and emissions. Therefore, it is of great importance to seek alternative fuels and clean combustion technologies for combustion in ICEs.

Methanol is one of the ideal alternative fuels for its rich resources and clean combustion features. It has a promising renewable feature, e.g., it can be produced from the reductive conversion of carbon dioxide with hydrogen. The raw material carbon dioxide could be captured from industrial effluents or the atmosphere, i.e., carbon dioxide is recycled into useful fuel in this process. Since the compression-ignition (CI) engines have a better fuel economy, there is a strong interest in applying methanol for CI engines. The engines in most of the trucks and some of the private cars are CI engines, or often known as diesel engine. In CI engines, liquid fuel is injected into the compressed air and auto-ignited as the compressed air has a high temperature and high pressure. However, it is difficult for pure methanol to ignite in conventional CI engines. The pure methanol-fueled CI engines suffer from incomplete combustion and misfire. As a result, novel combustion strategies, e.g., dual-fuel combustion, are developed to improve the ignition process in methanol-fueled CI engines. Dual-fuel combustion is a promising concept for combustion engines also because of its potential to reduce engine noise and emissions. The engines using dual-fuel combustion strategies are known as dual-fuel engines. In methanol/diesel dual-fuel engines, methanol is premixed with air during intake and compression strokes to form a methanol-air mixture, and then diesel is injected to ignite the methanol-air mixture. Although dual-fuel combustion has many advantages, it has been found

that inappropriate use of dual-fuel strategies may not be beneficial and may even deteriorate engine performance.

To enhance its benefits and avoid its shortcomings, detailed knowledge on dual-fuel combustion is needed including the fuel/air mixing, chemical kinetics and its interaction with the flow and mixing in the engine, the mechanisms of fuel ignition and combustion wave propagation, and reasons behind pollutant emissions. Such detailed knowledge can be gained by performing engine experiments and high-fidelity numerical simulations. In this thesis, numerical simulations are carried out to understand the physical and chemical processes in methanol/diesel dual-fuel combustion. Numerical simulation is a powerful method as it provides detailed insights, such as flow velocity, species and temperature distributions in three-dimensional space and time, which are needed to understand the fundamental processes in dual-fuel engines. Although some of these information can be obtained from engine experiments, the data acquisition in engine experiments is limited by the difficulty in accessing the engine through its metal walls, and diagnostic methods for detailed species distribution are available for only limited number of species. Numerical simulations have also limitations. The simulations are performed by solving highly nonlinear transport equations, which gives rise to the generates of a large span of flow scales in the flow. Such flow is known as turbulence. Simulation of all scales of engine turbulence is not possible with current supercomputers, and turbulence models are needed to simplify the problem. In this thesis, a high-fidelity method for the simulation of turbulence is used, which is known as large eddy simulation (LES). In LES, only large-scale turbulence eddies are solved while the small-scale eddies are modelled. In dual-fuel combustion, chemical reactions are interacting with turbulence. The combustion and emission behaviours of dual-fuel combustion are highly sensitive to the turbulence/chemistry interaction (TCI). A novel method for TCI is developed in this thesis, and validation of the method is carried out by comparing it with experiments. The new model is based on the transported probability density function and the Eulerian stochastics fields (ESF) approach.

The results of the simulation are first applied to study spray combustion that had been studied in experiments to make sure that the numerical methods can predict the real behaviour in such complex spray process. Then, the method is adopted to simulate various dual-fuel combustion. For example, altering the methanol concentration to check whether one can use more methanol and less diesel, or what the consequence will be if the methanol and air mixture is compressed to a higher temperature, or how the combustion and emission will be if the diesel is injected in different timing. Those are the questions to be answered in order to design high-performance dual-fuel engines.

The results show that a good agreement with the measurements is obtained in terms of the flow, combustion, and emissions. There are three ignition stages in methanol/n-heptane dual-fuel combustion, the first- and second-stage n-heptane ignition and the ambient methanol auto-ignition. The ambient methanol has an effect of suppressing the ignition. The more methanol is delivered, the later ignition of the n-heptane spray will be. A late diesel injection may lead to an overlap of the ambient methanol auto-ignition and liquid fuel injection, which results in a high pollutant emission. These observations and conclusions from the simulations will help engineers to design advanced engines for cars, trucks, and ships to burn methanol in a cleaner and more efficient way.

The main contributions of this thesis are two-fold: first, the proposed new ESF model can give rise to higher simulation accuracy, which can be used in engine design with high fidelity; second, the more in-depth knowledge on dual-fuel combustion which help engineering to better understand the performance of their engines and in turn help improve the design of the engines.

Abstract

Dual-fuel combustion is a promising concept in combustion engine applications, since it has the potential to reduce engine noise, soot and NOx emissions. However, it has been found that inappropriate uses of dual-fuel strategies may not be beneficial and may even be counterproductive for engine performance. To enhance its benefits and avoid its shortcomings, it is essential to understand the physical processes of ignition, combustion, and pollutant emissions in dual-fuel combustion under internal combustion engines conditions. The present thesis aims at studying these processes and strives to improve the understanding of the underlying mechanisms by means of computational fluid dynamics (CFD) simulations.

In dual-fuel engines, a primary fuel with a long ignition delay time (IDT) is premixed with air during intake and compression strokes to form a low-reactivity mixture, then a pilot fuel with a short IDT is injected to ignite the primary fuel-air mixture. The experimental configuration from Engine Combustion Network (ECN) is considered as the baseline case for simulations. In this configuration, a diesel surrogate fuel serves as the liquid pilot fuel, which is injected into a pressurized and preheated air/primary fuel-air mixture in a constant-volume vessel to mimic the single/dual-fuel combustion in conventional/dual-fuel engines. Large-eddy simulations (LES) with a state-of-art turbulence-chemistry interaction (TCI) model are employed to bring a deep insight into the flow, chemistry, and their interactions in single- and dual-fuel combustion. The main works are summarized in two parts: model developments and parameter studies.

In the first part, the Eulerian stochastic field (ESF) approach with a novel correction method is proposed, implemented, and examined. Light is shed on the TCI as the previous studies pointed out that TCI is of great importance for the spray flame under engine-like conditions. The consistency of ESF method with respect to the element mass conservation in simulations of turbulent combustion of multi-species and multi-step chemistry are investigated. Results show that the corrected ESF method removes the numerical error in the element mass conservation and shows capability in predicting both premixed and non-premixed flames in dual-fuel combustion.

In the second part, LES of n-heptane fueled single- and dual-fuel combustion are carried out and validated against ECN Spray-H experiments. A good agreement with the measurements is obtained in terms of flow, combustion, and emissions characteristics, such as the liquid and vapor penetration lengths, mixture fraction distribution, ignition delay times, lift-off length, pressure rise and

soot volume fraction. Finally, a parameter study is performed to investigate the effects of the dual-fuel strategies, including the primary fuel concentration, the ambient temperature, and the pilot fuel injection timing. Several concluding remarks are made. First of all, the ambient methanol is found to have an effect of suppressing the two-stage ignition and heat release of n-heptane, this is more significant under high ambient methanol concentration conditions. Secondly, the effects of methanol on the n-heptane ignition and NOx formation are strongly dependent on the ambient temperatures. The retardation of the n-heptane high temperature ignition is more remarkable under low ambient temperatures. The NOx and soot in the dual-fuel case is lower than that of the single-fuel case in the 900 K case, while an opposite trend is observed in the 1000 K dual-fuel case. Last but not least, a late injection may lead to an overlap of the ambient methanol auto-ignition and the delivery of n-heptane. This overlap results in high soot and NOx formation.

Nomenclature

Abbreviations

AN	non-reacting case based on Spray-A
AR	reacting cases based on Spray-A
ASI	after the start of injection
CCM	chemistry coordinate mapping
CFD	computational fluid dynamics
CFL	Courant–Friedrichs–Lewy
CI	compression–ignition
CVV	constant-volume vessel
DNS	direct numerical simulation
ECN	Engine Combustion Network
EGR	exhaust gas recirculation
ESF	Eulerian stochastic field
ESF-C	modified ESF solution procedure with two corrections
ESF-O	original ESF solution procedure with factorization scheme
FGM	flamelet generation manifold
HN	non-reacting case based on Spray-H
HR	reacting cases based on Spray-H
HRR	heat release rate
HTC	high temperature chemistry
ICE	internal combustion engine
IDT	ignition delay time
IEM	interaction by exchange with the mean
Ka	Karlovitz number
LES	large eddy simulation
LOL	lift-off length
LPL	liquid penetration length
LPT	lagrangian particle tracking
LTC	low temperature chemistry
MDF	composition mass density function
NTC	negative temperature coefficient
ODE	ordinary differential equation
PaSR	partially stirred reactor
PDF	probability density function
RANS	Reynolds-averaged Navier–Stokes
RMS	root mean square
SGS	sub-grid scale
SOC	start of combustion
SOI	start of injection
TCI	turbulence-chemistry interactions

TDC top-dead-center

TKE turbulence kinetic energy

URANS unsteady Reynolds-averaged Navier–Stokes

VPL vapor penetration length

WSR well-stirred reactor

Subscripts and superscripts

^{p} parcel

$_{\alpha}$ α-th chemical species

$_{\rho}$ mass or density related

$_{f,o(a)}$ index of fuel and oxidizer (air)

$_{h}$ sensible enthalpy

$_{i,j,k}$ directions in the Cartesian coordinates

$_{k}$ turbulent kinetic energy

$_{sgs}$ sub-grid scale term

$_{t}$ turbulent related term

$_{u}$ velocity or momentum related

$_{Y}$ chemical species related

Physical constants

Pr Prandtl number

Sc Schmidt number

Chemicals

CH_2O formaldehyde

CH_3OH methanol

CO carbon monoxide

CO_2 carbon dioxide

H_2 hydrogen

H_2O_2 hydrogen peroxide

NOx nitrogen oxide

OH hydroxyl

PM, soot particulate matter

RO_2 peroxyalkyl, heptyl-peroxide

UHC unburnt hydrocarbon

Operators

: double inner product

$\circ$ the stochastic product using the Stratonovitch interpretation

$\langle\cdot\rangle$, $\langle\cdot \mid \cdot\rangle$ ensemble average and conditional average

$\bar{\cdot}$ ensemble average in RANS or spatial filtered in LES

$\tilde{\cdot}$ Favre average

$\underline{\cdot}$ vector

Variables

χ_q quenching scalar dissipation rate

δ_{th} laminar thermal flame thickness

δ_T turbulent flame thickness

$\dot{\omega}$ chemistry source term

ϵ dissipation rate

η Kolmogorov length scale

$\eta^{(n)}$ standard normal random variables

Γ molecular diffusivity

ν kinematic viscosity

ω scalar mixing frequency

ϕ an arbitrary variable, or equivalence ratio

ϕ_m ambient methanol equivalence ratio

ρ density

τ viscous stress tensor

$\underline{\phi}$ a vector of composition variables

$\underline{\psi}$ a sample point of the composition variables

τ characteristic time

ξ an arbitrary stochastic variable

$\xi^{(n)}$ the stochastic fields system

B_ξ,$B(\xi, \underline{x}, t)$ the diffusion coefficient function in a diffusion process

D diffusion coefficient

$D\xi$ the material derivative of ξ

$d\xi$ the increasement of the stochastic field system

D_ξ,$D(\xi, \underline{x}, t)$ the drift coefficient function in a diffusion process

f a PDF

f' a fine-grained PDF

g body force

h sensible enthalpy

J molecular flux

k turbulent kinetic energy

l_0 integral length scale

m mass

N_R number of reactions

N_S number of species

N_{sf} number of stochastic field

p pressure

S source term

S_L laminar flame speed

S_T turbulent flame speed

t_d diffusion time scale

u velocity

u' velocity fluctuation

W, $\hat{W}$, $\underline{W}$ Wiener processes

Y species mass fraction

Z mixture fraction

Z_{st} stoichiometric mixture fraction

$\mathcal{F}$ composition mass density function

Chapter 1

Introduction

1.1 Background

The primary means of generating energy in the world is the combustion of fuels [1], of which 80% are fossil fuels, including coal oil and natural gas, according to the latest report by the International Energy Agency [2] in 2018. In the same year, the combustion of fossil fuels produced 99% of total carbon dioxide (CO_2) [2], which is a greenhouse gas that has been considered the primary source of global warming. In particular, combustion in the transport sector has a great contribution to the rapid depletion of fossil fuels, environmental damage, and global warming speedup. For example, the transport sector is responsible for 20% of the total energy consumed in 2018 [2]. The road transport, marine traffic, and aviation sectors contribute to 55% of total nitrogen oxide (NOx) emissions and 20% of total particulate matter (PM) emissions in 2017 [3]. In 2020, as a consequence of the confinement due to the COVID-19 pandemic, the slump in road transport activity accounted for 50% of the decline in global oil demand, and the drop in the aviation sector for around 35% in 2020 [2]. In addition, the global CO_2 emissions from surface transport fell by 36% by April 2020 and made the largest contribution to the total emissions change [4]. This interesting data shows that the transport sector has a great potential to reduce fossil fuels usage and CO_2 emissions. On the other hand, internal combustion engines (ICEs) remain the main power source in the transport sector as of 2020. Therefore, it is of great importance to seek alternative fuels and clean combustion technologies for combustion in ICEs.

1.1.1 Methanol as alternative fuel

Methanol (CH_3OH) is one of the alternative fuels for its rich resources and clean combustion features.

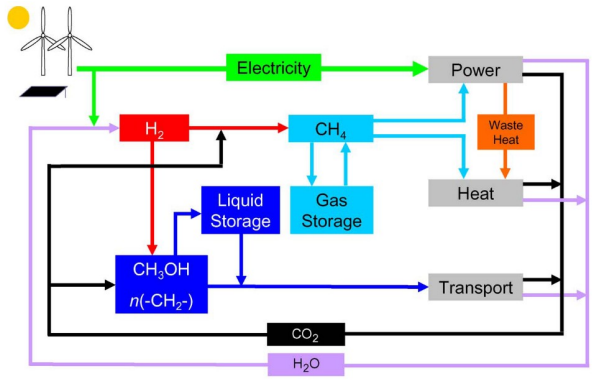

Figure 1.1: Integrated power, heat, and transport system combining renewable methane and liquid methanol [5].

Methanol can be produced from coal, petroleum, natural gas, and biomass [6]. In addition, methanol can be generated from another promising renewable source, e.g., the reductive conversion of CO_2 with hydrogen (H_2) [7]. The raw material CO_2 could be captured from industrial effluents or the atmosphere. CO_2 is recycled into useful fuel in this process and provides a source of hydrocarbons instead of just sequestration. Therefore, although methanol is not a carbon-free fuel, carbon neutrality is achieved through the reductive conversion reaction from the entire lifetime point of view. According to Ref. [7], if methanol can be efficiently produced from atmospheric carbon dioxide and hydrogen on a large scale, it is possible to operate the so-called methanol economy, which eventually liberates mankind from reliance on fossil fuels. This reaction could also be used as large-scale storage of hydrogen [8], which is a clean fuel but difficult to be stored. As compared with gaseous hydrogen, methanol is easier to store, transport, distribute, and use since methanol is in liquid form at room temperature. It can be combusted directly or used in direct-methanol fuel cells to provide heat or electricity. It can also be converted back to H_2 via a reforming process with water. By utilising this methanol-based system, H_2 can be stored at high density (99 kg H_2/m^3 for pure methanol) in liquid form at ambient conditions [9]. Fig. 1.1 is a schematic diagram showing the methanol production and utilization. In this sense, methanol is a hydrogen carrier fuel.

In terms of clean combustion features, it is found that methanol-fueled ICEs have the potential to reduce soot and NOx emissions [10, 11]. First, methanol is an oxygenated fuel without carbon–carbon bonds, which tends to not only

lower soot formation but also enhance oxidation of soot [11]. Second, methanol has a high latent heat value as compared with gasoline and diesel. High latent heat reduces the in-cylinder temperatures thus in favour of NOx reduction [12]. As the compression–ignition (CI) engines have a better fuel economy and are widely used in commercial applications, there is a strong interest in implementing methanol in CI engines [13]. However, it is difficult to use methanol directly in CI engines. In CI engines, air or air/exhaust gas mixture is inducted during the intake stroke. The fuel is delivered into the cylinder near the top-dead-centre (TDC) using a high-pressure fuel injector. The fuel is mixed with ambient gas, which has a high temperature and high pressure after the compression stroke. If the mixture temperature is above its auto-ignition temperature, the combustion is triggered. Auto-ignition is a spontaneous phenomenon of the fuel-air mixture. Under auto-ignition conditions, the fuel-air mixture ignites without an external source of ignition. The minimum auto-ignition temperature is the lowest temperature at which the fuel vapours spontaneously ignite. The time needed for the onset of auto-ignition is referred to as ignition delay time (IDT), which is one of the fuel characteristics indicating its ignitibility. For the ICE fuels, the cetane number (CN) is used as an indicator of fuel ignitibility. The higher the CN, the shorter IDT of the fuel. Due to the low CN of methanol, it is difficult for pure methanol to ignite in conventional CI engines. The pure methanol-fueled CI engines suffer from incomplete combustion and misfire. This issue becomes more severe in the condition of a cold start or at low engine loads [11, 14].

1.1.2 Dual-fuel combustion

As a result, novel combustion strategies, e.g., dual-fuel combustion, are developed to improve the ignition process in methanol-fueled CI engines. Dual-fuel combustion is a promising concept in combustion engine applications, since it has the potential to burn low CN fuels and it can be used to reduce engine noise [15], soot [14, 16, 17] and NOx [18–20] emissions. The engines using dual-fuel combustion strategies are known as dual-fuel engines. In dual-fuel premixed engines, a primary fuel with a long IDT is premixed with air during intake stroke to form a low-reactivity fuel-air mixture, then a pilot fuel with a short IDT is injected to ignite the premixed fuel-air mixture. As an auxiliary fuel, the supply of the pilot fuel is usually less than the primary fuel. It is essential to ignite the primary fuel-air mixture using a relatively small amount of pilot fuel to avoid the misfire leading to unburnt hydrocarbon (UHC) emissions. Therefore, it is important to know the proper amount of pilot fuel needed in methanol-fueled dual-fuel premixed engines.

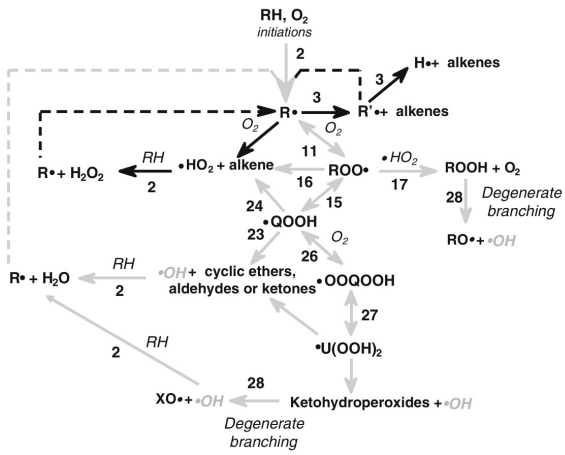

Figure 1.2: A simplified scheme for the mechanism of alkane oxidation. Reactions plotted in gray are important at low temperature (below 900 K), those in black at high temperature [21].

The pilot fuel has a high reactivity or a low auto-ignition temperature. The large alkane, e.g., the main composition of diesel, is usually used as pilot fuel. For alkanes, in general, the auto-ignition temperature decreases as the number of carbon atoms increases [22, 23]. Certain large alkanes tend to auto-ignite before small alkanes due to a counterintuitive behaviour, negative temperature coefficient (NTC) [21]. This distinctive feature of the oxidation of hydrocarbons signifies a zone of temperature, NTC regime. In the NTC regime, the IDT increases as the temperature increases [24]. This is due to the competition of the low-temperature chemistry (LTC) and high-temperature chemistry (HTC).

Figure 1.2 shows a simplified scheme of the LTC and HTC channels in the oxidation of an alkane (denoted as RH). Except at very high temperature (above 1200 K), the reaction is initiated by the abstraction of a hydrogen atom (H-abstraction) from the RH by oxygen (O_2) molecules to give alkyl (radical R·) and hydroperoxy (radical ·OOH) radicals [21]. In the LTC channels, R· radicals react rapidly with O_2 molecules to give peroxyalkyl (ROO·, or RO_2) radicals through the reaction R· + O_2 ⇌ ROO·, reaction 11 in Fig. 1.2. This reaction is reversible. The equilibrium shifts back to the reactants as the temperature increases. On the other hand, according to Ref. [25], the ROO· radicals can either generate ·HO_2 radicals and alkene or consume ·HO_2 radicals through the isomerization to give hydroperoxyalky (·QOOH) radicals. At low temperatures, i.e., below 900 K, ROO· is in favour of the ·HO_2 formation. However, as the temperature increases, the formation of ·HO_2 is inhibited. Because of these two reasons, the LTC channels are more favored to the formation of ·HO_2, which could generate hydroperoxides (H_2O_2) through the disproportionation reaction

($2{\cdot}HO_2 = H_2O_2{+}O_2$). The reactivity decreases in the 700-800 K temperature range [21] because of the decrease in the production of H_2O_2. In the HTC channels, the formation of ROO· radicals through the addition to the oxygen of R· radicals is negligible. The decomposition of H_2O_2 becomes fast and generate hydroxyl (OH) radicals [24]. This reaction becomes very fast above 900 K. The propagation of the reaction is a chain reaction, in which OH radicals are the main chain carriers. The reversibility of the addition of R· radicals to O_2 molecules leads to a reduction of the overall reaction rate and is the main cause of the appearance of the NTC regime.

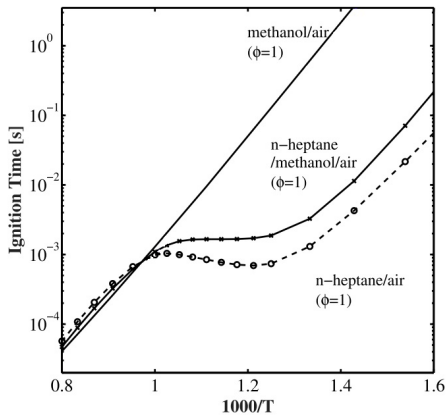

Figure 1.3: A comparison of ignition delay time in stoichiometric mixtures of n-heptane, methanol, and air in a constant volume condition under initial pressure of 4.2 MPa [26]. In the n-heptane/methanol/air mixture the molar ratio between the two fuels is 1. Results are based on zero-dimensional homogeneous reactor simulations using the Lu *et al.* [27] chemical mechanism, which is also used in the present study.

Figure 1.3 shows the IDTs of n-heptane/methanol/air stoichiometric mixtures at different temperature under an ICE pressure. As shown, the IDTs of methanol/air decrease monotonically in the semi-log coordinate as the reciprocal temperature, 1000/T, decreases. In contrast, n-heptane/air mixture's IDTs increases with the increase of temperature in the NTC regime of 1000/T from 1.25 to 1, i.e., 800 to 1000 K. These temperatures and pressures correspond to conditions similar to near TDC in-cyclinder conditions in dual-fuel premixed engines. The NTC regime is also found in the mixed n-heptane/methanol binary fuel. On the other hand, NTC regime is usually found in the pilot spray region due to liquid fuel evaporation. Thus, it is feasible to assist the ignition utilising the NTC behavior of large alkanes liquid fuels, e.g., n-heptane.

Diesel, a widely used CI engine fuel, is an ideal pilot fuel for methanol-fueled CI engines. In the recent studies conducted at Engine Research Center of University of Wisconsin–Madison, diesel/methanol dual-fuel engines were investigated [28–31]. For the computational fluid dynamics (CFD) simulation of diesel/methanol

engines, a compact and robust chemical kinetic mechanism is highly desirable. Methanol is a pure substance. Its chemical kinetic mechanism has been widely investigated and developed [32–34]. In contrast, diesel is a mixture which mainly consists of n-alkanes, iso-alkanes, cyclo-alkanes and aromatic hydrocarbons [35]. The components and their proportions vary in the production region and processes. The characterization of diesel in CFD using the detailed components is not always practical. Therefore, the method of fuel surrogate is adopted to represent the chemical characteristics of fuel mixture, including the IDT, adiabatic flame temperature, etc [36]. Liquid fuels n-heptane and n-dodecane are commonly used diesel surrogate fuel [37], as they have a similar CN and low-temperature chemistry behaviour to diesel. As a result, n-heptane and n-dodecane have been widely used in experiments [38] and numerical simulations [39] to mimic the spray combustion in diesel-fueled ICEs.

1.2 Motivation

It has been proven that the proper use of dual-fuel strategies is beneficial to the engine performance. Ma *et al.* [40] reported engine performance improvement by using dual-fuel combustion with different properties and reactivity fuels. In particular, high-temperature and fuel-rich region can be avoided in the combustion of lean premixed mixture, with the result of both low emission of soot and NOx. However, inappropriate use of dual-fuel strategies may not be beneficial and may even be counterproductive for engine performance [41]. For example, Liu *et al.* [16] showed in their experimental work that the thermal efficiency under dual-fuel mode was lower than that of the single-fuel (conventional compression ignition) mode at low engine loads, especially with a low amount of pilot fuel injected. This is not yet fully understood.

Most recent research in the area of dual-fuel combustion has focused on the interaction between the primary fuel and the pilot fuel. In particular, three different mechanisms for the dual-fuel interaction have been studied. First, Zhang *et al.* [42] found that the addition of the primary fuel dilutes the ambient gas, decreases the oxygen concentration and increases the heat capacity of the ambient mixture, thus resulting in a low adiabatic flame temperature. As a consequence, the formation of soot and NOx is reduced due to low-temperature combustion. Second, the IDT of pilot fuel is retarded by the ambient lean fuel-air mixture, which extends the mixing time before the start of high-temperature combustion. On one hand, an enhanced mixing contributes to a smaller fuel-rich region, thereby reducing soot formation [43, 44]. On the other hand, the oxidation of soot is enhanced due to the increased entrainment of fresh oxygen

[45]. However, intensive mixing might lead to misfire or incomplete combustion in an engine [46], which reduces the thermal efficiency of the engine. Third, Papagiannakis *et al.* [47] pointed out that the heat release of premixed combustion increased the mean temperature during the expansion stroke, which in turn enhanced the soot oxidation [18, 48]. It is important to identify which of the mentioned mechanisms is the main one influencing the ignition, and pollutant formation in dual-fuel combustion under engine-like conditions. It is also worth noting that most of the investigations have been carried out in specific engines, which are case dependent. Kahila *et al.* [49] conducted a large eddy simulation of a methane-fueled dual-fuel combustion in a constant volume vessel. It was found that the LTC of the pilot fuel (n-dodecane) provided intermediate species and heat, which played an important role in the primary fuel (methane) oxidation. The same group also investigated different aspects of n-dodecane/methane dual-fuel combustion using their LES models [49–51]. Yet, fundamental numerical simulations on methanol-fueled dual-fuel combustion have been rare. This motivates the present study.

1.3 Objectives

The thesis is focused on the turbulent dual-fuel combustion. It is accomplished by the numerical simulations in a constant-volume chamber. CFD is employed as it provides the flow velocities, temperature, and species mass fraction distribution, which is crucial for a better understanding of the dual-fuel combustion and usually difficult to be achieved in the experiment. The simplified geometry is used to exclude the specific and complicated engine geometry effects. Large eddy simulation with advanced turbulence-chemistry interaction model is used to bring a deep insight into the flow, chemistry, and their interaction. The broad aim is to provide a better understanding of the dual-fuel combustion of methanol and n-heptane under engine conditions. The main objectives of the work are summarized below:

1. To formulate an Eulerian stochastic fields based transported probability density function method, accommodating the turbulence-chemistry interaction in the premixed and non-premixed flames, and dual-fuel combustion. This method has been developed previously with recent efforts focusing on the consistency. This issue is further explored, solved and examined in the current work.

2. To study the differences between the n-heptane single-fuel combustion and n-heptane/methanol dual-fuel combustion in terms of the ignition,

flame structures, and pollutant emissions. To understand the underlying mechanisms of these differences from point views of chemical reactions, physical dilution, and enhanced mixing.

3. To identify the conditions in which soot and NOx are reduced and also identify the main mechanisms and the conditions in which the deterioration of the pollutant emissions occurs in the n-heptane/methanol dual-fuel combustion.

4. To investigate the effects of the primary fuel concentration, ambient temperature, and pilot fuel injection timing on the dual-fuel combustion, providing suggestions on the dual-fuel strategies.

1.4 Thesis outline

In the next chapter, the mathematical models and numerical methods for the large eddy simulation of two-phase flow are presented. In Chapter 3, the mathematical description, improvement, and implementations of the Eulerian stochastic fields model are discussed. The capability of Eulerian stochastic fields model for simulations of premixed, non-premixed, and spray flames is analysed in Chapter 4. The computational configuration, case setups, and the comparison of the single- and dual-fuel combustion are described in Chapter 5. In Chapter 6, the effects of the dual-fuel strategies, including the primary fuel concentration (Paper I), the ambient temperature (Paper II) and the pilot fuel injection timing (Paper III) are studied. In Chapter 7, the conclusions and application-oriented suggestions for future work are given. The papers related to the thesis are included in the appendix.

Chapter 2

Modelling of the two-phase flow and turbulent combustion

In this chapter, the theory and mathematical models used in the large eddy simulation (LES) of the spray reactive flow are described. The motion of the liquid fuel droplets is described using the Lagrangian particle tracking (LPT) approach, while the gaseous flow is governed by compressible Navier-Stokes equations in the Eulerian framework.

2.1 Governing equations

2.1.1 Reactive flows

The gas phase flow is governed by the continuity, momentum, species, and energy transport equations, as described in Eqs. (2.1 – 2.4), respectively.

$$\frac{\partial \rho}{\partial t} + \frac{\partial \rho u_j}{\partial x_j} = S_\rho, \tag{2.1}$$

$$\frac{\partial \rho u_i}{\partial t} + \frac{\partial \rho u_i u_j}{\partial x_j} = \frac{\partial \tau_{ij}}{\partial x_j} - \frac{\partial p}{\partial x_i} + \rho g_i + S_i, \tag{2.2}$$

$$\frac{\partial \rho Y_\alpha}{\partial t} + \frac{\partial \rho Y_\alpha u_j}{\partial x_j} = -\frac{\partial J_j^\alpha}{\partial x_j} + \rho \dot{\omega}_\alpha + S_\alpha, \tag{2.3}$$

$$\frac{\partial \rho h}{\partial t} + \frac{\partial \rho h u_j}{\partial x_j} = -\frac{\partial J_j^h}{\partial x_j} + \frac{Dp}{Dt} + \rho \dot{\omega}_h + S_h, \tag{2.4}$$

where ρ, u, Y and h represent density, velocity, species mass fraction and sensible enthalpy, respectively. τ denotes the viscous stress tensor, p is pressure, and g is the body force per unit mass (i.e. gravity). J^{α} and J^{h} denote, respectively, the molecular diffusion fluxes of species and enthalpy. $\dot{\omega}_{\alpha}$ and $\dot{\omega}_{h}$ are the species mass fraction and energy source terms from the chemical reactions. The mass, momentum, species and energy source terms from the liquid phase are denoted as S_{ρ}, S_{i}, S_{α} and S_{h}, respectively. The subscripts, i and j represent the components of the i and j directions in the Cartesian coordinates. α represents the α-th chemical species. In the following text, Einstein notation is only applied for the Latin alphabet i, j, and k.

The molecular diffusion fluxes J^{α} and J^{h} are modelled using the Fick's law and Fourier's law, e.g.,

$$J_{j}^{\alpha} = -\rho D_{\alpha} \frac{\partial Y_{\alpha}}{\partial x_{j}}, \tag{2.5}$$

$$J_{j}^{h} = -\rho D_{h} \frac{\partial h}{\partial x_{j}}, \tag{2.6}$$

where, D_{α} and D_{h} are the species and thermal diffusion coefficients.

2.1.2 Chemical reaction mechanisms

The species mass fraction and energy source terms from the chemical reactions are modelled using a finite-rate chemistry model with detailed chemical reaction mechanisms. A chemical reaction mechanism system consists of species and reactions. An arbitrary elementary chemical reaction mechanism with N_S species and N_R reactions can be written as follows [52]:

$$\sum_{\alpha=1}^{N_S} \nu_{l\alpha}^{'} M_{\alpha} \leftrightharpoons \sum_{\alpha=1}^{N_S} \nu_{l\alpha}^{''} M_{\alpha} \ , (\alpha = 1, 2, ..., N_S, l \ = \ 1, 2, ..., N_R), \tag{2.7}$$

where M_{α} stands for one of the species in a N_S species system with species number α, and $\nu_{l\alpha}^{'}$ and $\nu_{l\alpha}^{''}$ are the stoichiometric coefficients in reaction with reaction number l.

The reaction rate for the l-th reaction can be evaluated by the following equation:

$$\dot{\omega}_{l} = k_{l,f}(T) \prod_{\beta=1}^{N_S} C_{\beta}^{\nu_{l\beta}^{'}} - k_{l,r}(T) \prod_{\beta=1}^{N_S} C_{\beta}^{\nu_{l\beta}^{''}}, (l \ = \ 1, 2, ..., N_R), \tag{2.8}$$

where $k_{l,f}(T)$ and $k_{l,r}(T)$ denote the forward and reverse rate coefficients for the reaction with reaction number l, respectively. The symbol C_{β} is the molar

concentration of species β. In general, the rate coefficients can be calculated with Arrhenius equation,

$$\begin{aligned} k_{l,f}(T) &= A_{l,f} T^{b_{l,f}} exp\left(-\frac{E_{A_{l,f}}}{R_u T}\right), \\ k_{l,r}(T) &= A_{l,r} T^{b_{l,r}} exp\left(-\frac{E_{A_{l,r}}}{R_u T}\right), \end{aligned} \tag{2.9}$$

where A, b and E_A denote the pre-exponential coefficient, temperature exponent coefficient, and activation energy, respectively. The subscript l, f or r stands for the number of reactions and its forward or reverse states. These coefficients are provided in the chemical mechanism.

The source term of the α-th species mass fraction, $\dot{\omega}_\alpha$, is the sum of the production in all the reactions:

$$\begin{aligned} \dot{\omega}_\alpha =& W_\alpha \sum_{l=1}^{N_R} \left[\left(\nu_{l\alpha}^{''} - \nu_{l\alpha}^{'} \right) \dot{\omega}_l \right] \\ =& W_\alpha \sum_{l=1}^{N_R} \left\{ \left(\nu_{l\alpha}^{''} - \nu_{l\alpha}^{'} \right) \left[k_{l,f}(T) \prod_{\beta=1}^{N_S} C_\beta^{\nu_{l\beta}^{'}} - k_{l,r}(T) \prod_{\beta=1}^{N_S} C_\beta^{\nu_{l\beta}^{''}} \right] \right\}, \end{aligned} \tag{2.10}$$

where W_α is the molecular weight of the α-th species.

The source term of the sensible enthalpy from the chemical reaction, $\dot{\omega}_h$, is the sum of the

$$\dot{\omega}_h = \sum_{\alpha=1}^{N_S} \dot{\omega}_\alpha \left(\Delta h_{f,\alpha}^0 + \int_{T_0}^{T} c_{p,\alpha} \mathrm{d}t \right), \tag{2.11}$$

where $\Delta h_{f,\alpha}^0$ is the formation enthalpy of the α-th species at the reference temperature T_0, $c_{p,\alpha}$ is the constant-pressure specific heat of the α-th species.

2.2 Modelling of the turbulence

In the present study, LES is adopted for the modelling of the turbulent flow. LES is highly desirable for the understanding of dual-fuel spray combustion as it is capable to predict the local ignition and extinction events and also provides information about the large-scale turbulence flow.

In LES, a spatial filter is employed to separate the turbulence flow into large scale and sub-grid scale (SGS) parts. The large scale flow is resolved while the

SGS scale flow is modelled. For an arbitrary variable ϕ, the spatial filtered value $\overline{\phi}$ is

$$\overline{\phi}(\mathbf{x},t) = \int_{\Delta} \phi(\mathbf{x}',t) G(\mathbf{x}-\mathbf{x}') d\mathbf{x}', \tag{2.12}$$

where G is the filtering function, Δ is the filter size where $\int_{\Delta} G d\mathbf{x}' = 1$. In this study, a box filter is used with a filter size estimated by the single cell volume.

For the variable-density flows, the natural dependent variables are density-weighted. The density-weighted spatial averaged (or Favre average) variable $\tilde{\phi}$ is defined by,

$$\tilde{\phi} = \frac{\overline{\rho\phi}}{\overline{\rho}}. \tag{2.13}$$

The variable ϕ is then decomposed into a resolved large scale part $\tilde{\phi}$ and unsolved SGS part ϕ'', i.e.,

$$\phi = \tilde{\phi} + \phi''. \tag{2.14}$$

Applying filtering procedure, Eqs. (2.12–2.14), to ρ, u, Y and h in Eqs. (2.1 – 2.4), the LES formulation of the continuity, momentum, species and energy equations is obtained.

$$\frac{\partial \overline{\rho}}{\partial t} + \frac{\partial \overline{\rho}\tilde{u}_j}{\partial x_j} = \overline{S}_{\rho}, \tag{2.15}$$

$$\frac{\partial \overline{\rho}\tilde{u}_i}{\partial t} + \frac{\partial \overline{\rho}\tilde{u}_i\tilde{u}_j}{\partial x_j} = \frac{\partial \left(\overline{\rho}\tilde{u}_i\tilde{u}_j - \overline{\rho}\widetilde{u_i u_j}\right)}{\partial x_j} + \frac{\partial \overline{\tau}_{ij}}{\partial x_j} - \frac{\partial \overline{p}}{\partial x_i} + \overline{\rho} g_i + \overline{S}_i, \tag{2.16}$$

$$\frac{\partial \overline{\rho}\tilde{Y}_{\alpha}}{\partial t} + \frac{\partial \overline{\rho}\tilde{Y}_{\alpha}\tilde{u}_j}{\partial x_j} = \frac{\partial \left(\overline{\rho}\tilde{Y}_{\alpha}\tilde{u}_j - \overline{\rho}\widetilde{Y_{\alpha}u_j}\right)}{\partial x_j} + \frac{\partial}{\partial x_j}\left(\overline{\rho} D_{\alpha} \frac{\partial \tilde{Y}_{\alpha}}{\partial x_j}\right) + \overline{\rho}\widetilde{\dot{\omega}}_{\alpha} + \overline{S}_{\alpha}, \tag{2.17}$$

$$\frac{\partial \overline{\rho}\tilde{h}}{\partial t} + \frac{\partial \overline{\rho}\tilde{h}\tilde{u}_j}{\partial x_j} = \frac{\partial \left(\overline{\rho}\tilde{h}\tilde{u}_j - \overline{\rho}\widetilde{hu_j}\right)}{\partial x_j} + \frac{D\overline{p}}{Dt} + \frac{\partial}{\partial x_j}\left(\overline{\rho} D_h \frac{\partial \tilde{h}}{\partial x_j}\right) + \overline{\rho}\widetilde{\dot{\omega}}_h + \overline{S}_h, \tag{2.18}$$

where the first terms on the R.H.S. in Eqs. (2.16), (2.17), and (2.18) represent the SGS effects, which are unclosed and need to be modelled.

The turbulent-viscosity hypothesis [53] and the one-equation eddy viscosity model [54] are used to model the SGS terms in Eq. (2.16). The SGS stress tensor $\tau_{ij}^{sgs} = \overline{\rho}\widetilde{u_i u_j} - \overline{\rho}\tilde{u}_i\tilde{u}_j$ is modelled as [55],

$$\tau_{ij}^{sgs} \approx \frac{2}{3}\overline{\rho}\delta_{ij}k_{sgs} - 2\overline{\rho}\nu_{sgs}\left(\tilde{S}_{ij} - \frac{1}{3}\delta_{ij}\tilde{S}_{kk}\right), \tag{2.19}$$

with

$$\tilde{S}_{ij} = \frac{1}{2}\left(\frac{\partial \tilde{u}_j}{\partial x_i} + \frac{\partial \tilde{u}_i}{\partial x_j}\right), \tag{2.20}$$

where δ is the Kronecker delta. ν_{sgs} is the SGS kinematic turbulent viscosity, and k_{sgs} is the SGS turbulent kinetic energy, $k_{sgs} = (\widetilde{u_k^2} - \tilde{u}_k^2)/2$. The transport equation of k_{sgs} is given by [54, 55],

$$\begin{aligned}\frac{\partial \overline{\rho} k_{sgs}}{\partial t} + \frac{\partial (\overline{\rho} k_{sgs} \tilde{u}_j)}{\partial x_j} =& \frac{\partial}{\partial x_j}\left[\overline{\rho}\left(\nu + \nu_{sgs}\right)\frac{\partial k_{sgs}}{\partial x_j}\right] \\ & -\tau_{ij}^{sgs}\frac{\partial \tilde{u}_j}{\partial x_i} - C_\epsilon \frac{\overline{\rho}}{\Delta}(k_{sgs})^{3/2} + \overline{S}_k,\end{aligned} \tag{2.21}$$

$$\nu_{sgs} = C_k \sqrt{k_{sgs}}\Delta, \tag{2.22}$$

where S_k is the spray-induced turbulence source term. C_k and C_ϵ are the model constants.

The gradient-diffusion hypothesis [56] is introduced to model the SGS terms in Eqs. (2.17) and (2.18), e.g.,

$$\begin{aligned}\overline{\rho}\tilde{Y}_\alpha \tilde{u}_j - \overline{\rho}\widetilde{Y_\alpha u_j} &\approx \overline{\rho}\frac{\nu_{sgs}}{\mathrm{Pr}_t}\frac{\partial \tilde{Y}_\alpha}{\partial x_j}, \\ \overline{\rho}\tilde{h}\tilde{u}_j - \overline{\rho}\widetilde{h u_j} &\approx \overline{\rho}\frac{\nu_{sgs}}{\mathrm{Sc}_t}\frac{\partial \tilde{h}}{\partial x_j},\end{aligned} \tag{2.23}$$

where Pr_t and Sc_t are nondimensional turbulent Prandtl number and Schmidt number.

In Paper I–V, Eqs. (2.15) and (2.16) are solved using the one-equation eddy viscosity model, Eqs. (2.21) and (2.22). Eqs. (2.17) and (2.18) are solved associated with the gradient-diffusion hypothesis, Eq. (2.23), in papers using finite-rate chemistry model, i.e., Paper I–III and V. In terms of the model constants, readers are referred to the specific paper.

2.3 Modelling of liquid-gas flow

The liquid phase is described using the LPT approach. A large number of parcels are tracked to represent the liquid phase fuel droplets. In each parcel, a certain number of liquid droplets are clustered. The governing equations for the motion of a parcel (denoted as p) in the LPT approach are written as:

$$\frac{d}{dt}\vec{x}_p = \vec{u}_p, \tag{2.24}$$

$$\frac{d}{dt}\vec{u}_p = \frac{C_D}{\tau_p}\frac{Re_p}{24}\left(\vec{u}_g - \vec{u}_p\right) + \vec{g}. \tag{2.25}$$

In this equation, $\vec{x}_p$ is the parcel location in the Cartesian coordinates. $\vec{u}_p$ and $\vec{u}_g$ are the parcel and surrounding gas velocity, respectively; $\vec{g} = (g_1, g_2, g_3)$ is the body force as in Eq. (2.2); $\tau_p = d_p^2/18\nu$ is the parcel characteristic time related to the parcel diameter, d_p, and the gas phase kinematic viscosity, ν. $Re_p = |\vec{u}_g - \vec{u}_p| d_p/\nu$ is the parcel Reynolds number, C_D is the drag coefficient, which is a function of Re_p. More detailed descriptions are available in Ref. [39].

The interaction between the gas and liquid phase is considered via the source terms in the gas phase governing equations, denoted as S_ρ, S_i, S_α and S_h in Eqs. (2.15 – 2.18) and S_k in Eq. (2.21). The momentum source term S_i can be expressed as a function of the parcel mass, number density, and velocity (see Paper III). Similarly, the source terms in the continuity, species and energy transport equations are obtained by considering spray vaporization and heat transfer processes. The Ranz-Marshall correlation [57, 58] is used to model heat transfer between the liquid and gas phases while the evaporation is modelled using the Spalding formula [59].

2.4 Modelling of the TCI

The turbulence–chemistry interactions (TCI) is of great importance to the turbulent combustion modelling, especially for the spray flame under engine-like conditions [60]. In LES, TCI in the SGS is accounted for by the modelling of the filtered reaction rate. This is a challenging task since the chemical reaction rates are highly non-linear functions of temperature.

The commonly used TCI models are the Conditional Moment-Closure (CMC) [61], the probability density function (PDF) model [62], the linear eddy model (LEM) [63, 64], and the Flamelet Generation Manifold (FGM) [65]. Table 2.1 shows a list of recent LES studies of the Engine Combustion Network (ECN) spray combustion cases. A summary of the unsteady Reynolds-averaged Navier–Stokes (URANS) simulations is available in Ref. [66].

In the present study, the well-stirred reactor (WSR), partially-stirred reactor (PaSR), and Eulerian stochastic field (ESF) based transported PDF models are employed to model the filtered chemical source terms $\widetilde{\dot{\omega}}_\alpha$ and $\widetilde{\dot{\omega}}_h$ in Eqs. (2.17) and (2.18).

Table 2.1: Recent LES studies of ECN spray flames.

Fuel	Combustion Model	Turbulence Model	Code	Ref.
n-Heptane	WSR	Smagorinsky	Converge	[67]
n-Heptane	FMDF[1]	-	In-house	[68]
n-Heptane	ESF	Dynamic Smagorinsky	In-house	[62]
n-Heptane	WSR	Smagorinsky, dynamic structure	ANSYS	[69]
n-Heptane/ methane	LEM	-	KIVA	[63]
n-Dodecane	WSR	One-equation eddy	OpenFOAM	[39]
n-Dodecane	WSR	Dynamic structure	Converge	[70]
n-Dodecane	FGM	-	OpenFOAM	[65]
n-Dodecane	TFM[2]	Dynamic structure	Converge	[71]
n-Dodecane	CMC	$k-\ell$ two-equations	Star-CD	[61]
n-Dodecane	PaSR	One-equation eddy	OpenFOAM	[72]
n-Dodecane/ methane	WSR	Implicit LES	OpenFOAM	[49–51]
n-Dodecane	LEM	-	KIVA	[64]

[1] Compressible filtered mass density function (FMDF).
[2] Tabulated Flamelet Model (TFM).

2.4.1 Well-stirred reactor model

In the WSR model, a first order closure hypothesis is used to estimate the filtered reaction rates, i.e., the subgrid scale effect is absent in the filtered reaction rates. Each computational cell is treated as a closed homogeneous reactor [73]. The chemical kinetics ordinary differential equations (ODEs) are integrated over a flow time step to update the thermochemical compositions [74]. The reaction rate of the l-th reaction, $\widetilde{\dot{\omega}}_l$, is estimated as follows:

$$\widetilde{\dot{\omega}}_l = \dot{\omega}_l(\widetilde{Y}, \widetilde{T}, \overline{p}). \tag{2.26}$$

The chemical source terms $\widetilde{\dot{\omega}}_\alpha$ and $\widetilde{\dot{\omega}}_h$ in Eqs. (2.17) and (2.18) are obtained from the integration of $\widetilde{\dot{\omega}}_l$ over all the reactions.

Due to the implementation simplicity and computational efficiency, this method has been widely used in the simulation of conventional diesel, spark ignition and Homogeneous Charge Compression Ignition (HCCI) engines over the years

[75–77]. This model has shown capabilities on the prediction of ignition, and flame stabilization in previous LES on spray combustion [39, 49, 50, 78, 79]. In Chapter 4, the WSR model is employed for model comparison.

2.4.2 Partially-stirred reactor model

The PaSR model is based on a subgrid stirred reactor approximation, which takes TCI into account by including the Kolmogorov scale mixing in each computational cell [80]. In the PaSR model, each computational cell is composed of two local elements: a reacting and a non-reacting uniform mixture. The filtered reaction rates is calculated as given by

$$\widetilde{\dot{\omega}}_l = \kappa \dot{\omega}_l(\widetilde{Y}, \widetilde{T}, \overline{p}), \tag{2.27}$$

where κ is the volume fraction of the reacting mixture. κ is proportional to the ratio of the chemical reaction time, τ_c, to the total conversion time in the reactor, i.e., the sum of τ_c and the micromixing time, τ_m.

$$\kappa = \frac{\tau_c}{\tau_m + \tau_c}. \tag{2.28}$$

The chemical reaction time scale, τ_c, is determined by chemical kinetics [80]:

$$\frac{1}{\tau_c} = max\left\{\frac{-\dot{\omega}_f}{Y_f}, \frac{-\dot{\omega}_o}{Y_o}\right\}. \tag{2.29}$$

The subscripts f and o are the species indexes of fuel and oxidizer, respectively.

Chomiak *et al.* [80] proposed an approach to estimate τ_m from the geometrical mean of the Kolmogorov and Taylor time scales, τ_k and τ_t, as

$$\tau_m = C_{mix}\sqrt{\tau_k \tau_t}, \tag{2.30}$$

where C_{mix} is a model constant.

The spray flame is a typical ignition-driven combustion process, which is within the scope of the PaSR model [72]. The use of this PaSR model has been widely validated in previous works on spray combustion [72, 73, 80]. The PaSR model is used in Paper II and III.

2.4.3 Eulerian stochastic fields method

The transported PDF is a promising approach for modelling the TCI effects for a wide range of turbulent flames [52, 81–83]. It has been successfully used to

simulate the lifted flames [62, 84–87] and shown accurate prediction on autoignition and flame stabilization. As one of the transported PDF formulations, the Eulerian stochastic field method solves the PDF by transporting a series of stochastic fields based on the Monte Carlo method [52, 88]. In this method, the one-point one-time joint PDF is expressed as an ensemble of the stochastic fields in which the TCI effect can be computed directly without the need for modeling. The formulations, implementation, and improvement of ESF are discussed in the next chapter (also in Paper I, IV and V).

2.5 Modelling of NOx and soot emission

The extended Zeldovich mechanism [89] (with additional 4 species and 13 reactions) is employed to describe the thermal NO_x formation, including NO and NO_2. Compared with NO and NO_2, N_2O has a relatively low concentration under engine conditions [90, 91]. Thus, it has been neglected in most numerical simulations [90, 92]. In this study (see Paper II), total mass of NOx is calculated as the sum of the mass of NO and NO_2 [90–92].

With relevance to Paper II, a phenomenological multi-step soot model, proposed by Leung *et al.* [93], is employed for soot prediction. In this model, the soot particle nucleus is formed from a soot precursor. Upon the formation of the soot nuclei, soot particles subsequently undergo surface growth, coagulation and oxidation. Equations (2.31) and (2.32) are employed to describe the transport of soot particle number density, ϕ_N, and soot mass fraction, Y_{soot}, during the soot formation process. The soot volume fraction, f_v, is then computed using $f_v = Y_{soot}\rho_{gas}/\rho_{soot}$.

$$\frac{\partial \overline{\rho}\tilde{\phi}_N}{\partial t} + \frac{\partial \overline{\rho}\tilde{u}_j\tilde{\phi}_N}{\partial x_j} - \frac{\partial}{\partial x_j}\left[\overline{\rho}\left(D_N + \frac{\nu_{sgs}}{\mathrm{Pr}_t}\right)\frac{\partial \tilde{\phi}_N}{\partial x_j}\right] = \frac{1}{N_A}\frac{dN}{dt}, \tag{2.31}$$

$$\frac{\partial \overline{\rho}\tilde{Y}_{soot}}{\partial t} + \frac{\partial \overline{\rho}\tilde{u}_j\tilde{Y}_{soot}}{\partial x_j} - \frac{\partial}{\partial x_j}\left[\overline{\rho}\left(D_{soot} + \frac{\nu_{sgs}}{\mathrm{Pr}_t}\right)\frac{\partial \tilde{Y}_{soot}}{\partial x_j}\right] = \frac{dM}{dt}. \tag{2.32}$$

Here, N and N_A denote respectively the number of soot particles and Avogadro constant. D_N and D_{soot} are the molecular diffusion coefficients, ν_{sgs}/Pr_t is the SGS eddy diffusion coefficient modeled using the k-equation eddy viscosity model. dN/dt and dM/dt are the source terms for particle number density and soot mass, modeled by $dN/dt = N_A \cdot r_1 - r_2$ and $dM/dt = M_p \cdot r_1 + r_3 - r_4$, respectively, where M_p is the mass of an incipient soot particle. r_1 to r_4 are the rates of nucleation, coagulation, surface growth and oxidation. For more details of the soot model, the readers are referred to Ref. [94].

2.6 Numerical methods

The open-source code OpenFOAM [95] version 4 and 7 are used in this study. The Eqs. (2.15–2.18) are solved using finite volume method. The solver that was used in this thesis has a second-order accuracy in spatial discretisation and second-order accuracy in temporal integration. The diffusion and convection terms are discretised by a filtered-linear scheme, while the time integration is based on an implicit backward scheme. In addition, the integration of the chemical reaction rates is calculated using the ordinary differential equation (ODE) Seulex [96] solver, which is a high-order solver based on the linearly implicit Euler method. In the present LES, over 95% of the computational time are consumed in the integration of the chemical reactions. To speed up the integration of the chemical reactions, a chemistry coordinate mapping (CCM) approach is applied. The approach can reduce the number of chemical reaction cells by a factor of 20 in the current LES after the n-heptane ignition. Details of the CCM theory and its application to spray combustion can be found in Refs. [97, 98]. The solution procedure employed for the decoupling of the pressure and velocity fields is the PIMPLE algorithm [99], which is a combination of the Pressure Implicit with Splitting of Operator (PISO) algorithm and the Semi-Implicit Method for Pressure-Linked Equations (SIMPLE) algorithm. In the current LES, three corrector steps are applied in the PIMPLE algorithm to reduce the error of the pressure and velocity.

Chapter 3

Developments of the Eulerian stochastic fields model

3.1 Eulerian transported PDF method

3.1.1 Fine-grained composition PDF

The composition PDF, $f_{\underline{\phi}}$, represents the probability of a composition state, including species mass fraction and sensible enthalpy, in the flow. The subscript $\underline{\phi}$ denotes that it is a PDF for the composition variables $\underline{\phi}$. The underline denotes that $\underline{\phi}$ is a vector, $\underline{\phi} = (\phi_1, \phi_2, \ldots, \phi_N)$.

The fine-grained composition PDF, $f'_{\underline{\phi}}$, can be interpreted as a representation of the composition PDF for a single realization of the flow [52]. At a position $\underline{x}$ and time t, a single realization of the composition state in the flow is denoted as $\underline{\phi}(\underline{x}, t)$. It is a N–dimensional state vector in an Euclidean space of composition, i.e., composition space. The fine-grained composition PDF is the corresponding PDF of this state, defined by [56]

$$f'_{\underline{\phi}}(\underline{\psi}; \underline{x}, t) \equiv \delta\left(\underline{\phi}(\underline{x}, t) - \underline{\psi}\right) = \prod_{\alpha=1}^{N} \delta\left(\phi_\alpha(\underline{x}, t) - \psi_\alpha\right), \tag{3.1}$$

where the one-point, one-time fine-grained composition PDF, $f'_{\underline{\phi}} = f'_{\underline{\phi}}(\underline{\psi}; \underline{x}, t)$, is a N–dimensional delta function. $\underline{\psi}$ is a sample point of the composition variables $\underline{\phi}$. The point $\underline{\psi}$ has coordinates of $(\psi_1, \psi_2, \ldots, \psi_N)$ in the composition space, e.g., ψ_α denotes a specific species mass fraction or sensible enthalpy.

The fine-grained PDF has two important properties [56]:

$$\langle f'_{\underline{\phi}}(\underline{\psi};\underline{x},t)\rangle = f_{\underline{\phi}}(\underline{\psi};\underline{x},t), \tag{3.2}$$

$$\langle \xi(\underline{x},t) f'_{\underline{\phi}}(\underline{\psi};\underline{x},t)\rangle = \langle \xi(\underline{x},t) \mid \underline{\phi}(\underline{x},t) = \underline{\psi}\rangle f_{\underline{\phi}}(\underline{\psi};\underline{x},t), \tag{3.3}$$

where $\langle\cdot\rangle$ denotes ensemble average, $\langle \cdot \mid \underline{\phi}(\underline{x},t) = \underline{\psi}\rangle$ is the conditional average under the condition of $\underline{\phi}(\underline{x},t) = \underline{\psi}$, also denoted as $\langle \cdot \mid \underline{\psi}\rangle$ for brevity. $\xi = \xi(\underline{x},t)$ is an arbitrary function.

The proof of these two properties are available in Ref. [56]. The following subsections introduce the formulation of the PDF transport equation.

3.1.2 Transport equation of the composition PDF

For a constant density flow, the transport equation of a single-scalar field, $\phi_\alpha = \phi_\alpha(\underline{x},t)$, is written as

$$\frac{\partial \phi_\alpha}{\partial t} + u_j \frac{\partial \phi_\alpha}{\partial x_j} = \frac{\partial}{\partial x_j}\left(\Gamma \frac{\partial \phi_\alpha}{\partial x_j}\right) + S(\underline{\phi}), \alpha = 1, 2, \ldots, N. \tag{3.4}$$

Γ is the molecular diffusivity, S is a reaction source term which is a function of the composition variables $\underline{\phi}$.

The transport equation of the fine-grained PDF can be derived using Eq. (3.4), the properties of delta functions, and the chain rules of the temporal and spatial derivatives in Eqs. (3.5) and (3.6).

$$\frac{\partial f'_{\underline{\phi}}}{\partial t} = \frac{\partial f'_{\underline{\phi}}}{\partial \phi_\alpha}\frac{\partial \phi_\alpha}{\partial t} = -\frac{\partial f'_{\underline{\phi}}}{\partial \psi_\alpha}\frac{\partial \phi_\alpha}{\partial t}, \tag{3.5}$$

$$\frac{\partial f'_{\underline{\phi}}}{\partial x_j} = \frac{\partial f'_{\underline{\phi}}}{\partial \phi_\alpha}\frac{\partial \phi_\alpha}{\partial x_j} = -\frac{\partial f'_{\underline{\phi}}}{\partial \psi_\alpha}\frac{\partial \phi_\alpha}{\partial x_j}. \tag{3.6}$$

Specifically, substituting Eqs. (3.5) and (3.6) into (3.4), one has

$$\begin{aligned}
\frac{\partial f'_{\underline{\phi}}}{\partial t} + u_j \frac{\partial f'_{\underline{\phi}}}{\partial x_j} &= -\frac{\partial f'_{\underline{\phi}}}{\partial \psi_\alpha}\frac{\partial \phi_\alpha}{\partial t} - u_j \frac{\partial f'_{\underline{\phi}}}{\partial \psi_\alpha}\frac{\partial \phi_\alpha}{\partial x_j} \\
&= -\frac{\partial}{\partial \psi_\alpha}\left[\left(\frac{\partial \phi_\alpha}{\partial t} + u_j \frac{\partial \phi_\alpha}{\partial x_j}\right) f'_{\underline{\phi}}\right] \\
&= -\frac{\partial}{\partial \psi_\alpha}\left\{\left[\frac{\partial}{\partial x_j}\left(\Gamma \frac{\partial \phi_\alpha}{\partial x_j}\right) + S(\underline{\psi})\right] f'_{\underline{\phi}}\right\} \\
&= -\frac{\partial}{\partial \psi_\alpha}\left[\frac{\partial}{\partial x_j}\left(\Gamma \frac{\partial \phi_\alpha}{\partial x_j}\right) f'_{\underline{\phi}}\right] - \frac{\partial S(\underline{\psi}) f'_{\underline{\phi}}}{\partial \psi_\alpha},
\end{aligned} \tag{3.7}$$

and

$$\frac{\partial}{\partial x_j}\left(\Gamma\frac{\partial f'_{\underline{\phi}}}{\partial x_j}\right)=\frac{\partial}{\partial \psi_\alpha}\left(\Gamma\frac{\partial f'_{\underline{\phi}}}{\partial \psi_\alpha}\right)\frac{\partial \phi_\alpha}{\partial x_j}\frac{\partial \phi_\alpha}{\partial x_j}-\frac{\partial}{\partial \psi_\alpha}\left[\frac{\partial}{\partial x_j}\left(\Gamma\frac{\partial \phi_\alpha}{\partial x_j}\right)f'_{\underline{\phi}}\right]. \quad (3.8)$$

Subtracting the left and right hand sides (L.H.S and R.H.S), the transport equation of the fine-grained PDF is obtained:

$$\frac{\partial f'_{\underline{\phi}}}{\partial t}+u_j\frac{\partial f'_{\underline{\phi}}}{\partial x_j}-\frac{\partial}{\partial x_j}\left(\Gamma\frac{\partial f'_{\underline{\phi}}}{\partial x_j}\right)=-\frac{\partial}{\partial \psi_\alpha}\left(\Gamma\frac{\partial f'_{\underline{\phi}}}{\partial \psi_\alpha}\right)\frac{\partial \phi_\alpha}{\partial x_j}\frac{\partial \phi_\alpha}{\partial x_j}-\frac{\partial S(\underline{\psi})f'_{\underline{\phi}}}{\partial \psi_\alpha}. \quad (3.9)$$

By taking the ensemble average of the fine-grained PDF transport Eq. (3.9), and using the properties of fine-grained PDF Eqs. (3.2) and (3.3), a transport equation of the composition PDF, $f_{\underline{\phi}}$, is derived as

$$\begin{aligned}&\frac{\partial}{\partial t}f_{\underline{\phi}}+\frac{\partial}{\partial x_j}\left[\langle u_j\,|\,\underline{\psi}\rangle\, f_{\underline{\phi}}\right]-\frac{\partial}{\partial x_j}\left(\Gamma\frac{\partial f_{\underline{\phi}}}{\partial x_j}\right)\\ =&-\frac{\partial^2}{\partial \psi_\alpha^2}\left[\Gamma\left\langle\frac{\partial \phi_\alpha}{\partial x_j}\frac{\partial \phi_\alpha}{\partial x_j}\,\middle|\,\underline{\psi}\right\rangle f_{\underline{\phi}}\right]-\frac{\partial}{\partial \psi_\alpha}\left[S(\underline{\psi})f_{\underline{\phi}}\right].\end{aligned} \quad (3.10)$$

According to Ref. [100], the second term of the L.H.S and the first term of the R.H.S in Eq. (3.10) can be closed using Eqs. (3.11) and (3.12). For further closure, the gradient-diffusion transport model and turbulence model with eddy viscosity hypothesis are needed, i.e. Eq. (3.13); the second term of R.H.S in Eq. (3.12) is closed using a micro-mixing model, i.e., the interaction by exchange with the mean (IEM) model, cf. Eq. (3.14).

$$\langle u_j\,|\,\underline{\psi}\rangle=\langle u_j\rangle+\langle u'_j\,|\,\underline{\psi}\rangle, \quad (3.11)$$

$$\left\langle\frac{\partial \phi_\alpha}{\partial x_j}\frac{\partial \phi_\alpha}{\partial x_j}\,\middle|\,\underline{\psi}\right\rangle=\left\langle\frac{\partial \phi_\alpha}{\partial x_j}\right\rangle\left\langle\frac{\partial \phi_\alpha}{\partial x_j}\right\rangle+\left\langle\frac{\partial \phi'_\alpha}{\partial x_j}\frac{\partial \phi'_\alpha}{\partial x_j}\,\middle|\,\underline{\psi}\right\rangle, \quad (3.12)$$

$$\langle u'_j\,|\,\underline{\psi}\rangle f_{\underline{\phi}}=-\Gamma_t\frac{\partial f_{\underline{\phi}}}{\partial x_j}, \quad (3.13)$$

$$\frac{\partial}{\partial \psi_\alpha}\left[\Gamma\left\langle\frac{\partial \phi'_\alpha}{\partial x_j}\frac{\partial \phi'_\alpha}{\partial x_j}\,\middle|\,\underline{\psi}\right\rangle f_{\underline{\phi}}\right]=-\omega\left(\psi_\alpha-\langle\phi_\alpha\rangle\right)f_{\underline{\phi}}, \quad (3.14)$$

where $\langle\cdot\rangle$ and $'$ denote time averaging and fluctuations in RANS, or spacial averaging and sub-grid fluctuations in LES. Γ_t is the turbulent eddy diffusivity, ω is the scalar mixing frequency.

After substituting Eqs. (3.11)-(3.14) into Eq. (3.10), a closed form of the modelled transport equation of the composition PDF is attained,

$$\begin{aligned}\frac{\partial}{\partial t}f_{\underline{\phi}}+\frac{\partial}{\partial x_j}\left(\langle u_j\rangle f_{\underline{\phi}}\right)-\frac{\partial}{\partial x_j}\left[(\Gamma+\Gamma_t)\frac{\partial f_{\underline{\phi}}}{\partial x_j}\right]=\\ -\frac{\partial^2}{\partial\psi_\alpha^2}\left[\Gamma\left\langle\frac{\partial\phi_\alpha}{\partial x_j}\right\rangle\left\langle\frac{\partial\phi_\alpha}{\partial x_j}\right\rangle f_{\underline{\phi}}\right]\\ +\frac{\partial}{\partial\psi_\alpha}\left[\omega\left(\psi_\alpha-\langle\phi_\alpha\rangle\right)f_{\underline{\phi}}\right]\\ -\frac{\partial}{\partial\psi_\alpha}\left[S(\underline{\psi})f_{\underline{\phi}}\right].\end{aligned}\tag{3.15}$$

In applying the PDF method to inhomogeneous variable-density flows, it is suggested [81] to use the density-weighted PDF $\widetilde{f}_{\underline{\phi}}$, in which ˜ denotes the Favre-average. However, the natural dependent variable is neither $f_{\underline{\phi}}$ nor $\widetilde{f}_{\underline{\phi}}$ but it is the composition mass density functions (MDF), $\mathcal{F}_{\underline{\phi}}$ [81]. They are defined by

$$\widetilde{f}_{\underline{\phi}}(\underline{\psi};\underline{x},t)=\langle\rho(\underline{\psi})f_{\underline{\phi}}(\underline{\psi};\underline{x},t)\rangle/\langle\rho\rangle,\tag{3.16}$$

$$\mathcal{F}_{\underline{\phi}}(\underline{\psi},\underline{x};t)=\langle\rho(\underline{\psi})f_{\underline{\phi}}(\underline{\psi};\underline{x},t)\rangle=\langle\rho\rangle\widetilde{f}_{\underline{\phi}}(\underline{\psi};\underline{x},t).\tag{3.17}$$

The transport equation for the MDF can be derived in the same manner as the constant density flow. For brevity, it is given as below:

$$\begin{aligned}\frac{\partial}{\partial t}\mathcal{F}_{\underline{\phi}}+\frac{\partial}{\partial x_j}\left[\left\langle u_j\mid\underline{\psi}\right\rangle\mathcal{F}_{\underline{\phi}}\right]=-\frac{\partial}{\partial\psi_\alpha}\left[S_\alpha(\underline{\psi})\mathcal{F}_{\underline{\phi}}\right]\\ +\frac{\partial}{\partial\psi_\alpha}\left[\left\langle\frac{1}{\rho}\frac{\partial J_j^\alpha}{\partial x_j}\middle|\underline{\psi}\right\rangle\mathcal{F}_{\underline{\phi}}\right],J_j^\alpha=\Gamma\frac{\partial\phi_\alpha}{\partial x_j}.\end{aligned}\tag{3.18}$$

The modelled MDF transport equation is

$$\begin{aligned}\frac{\partial}{\partial t}\mathcal{F}_{\underline{\phi}}+\frac{\partial}{\partial x_j}\left(\tilde{u}_j\mathcal{F}_{\underline{\phi}}\right)-\frac{\partial}{\partial x_j}\left[\frac{\Gamma+\Gamma_t}{\overline{\rho}}\frac{\partial\mathcal{F}_{\underline{\phi}}}{\partial x_j}\right]=\\ -\frac{\partial^2}{\partial\psi_\alpha^2}\left[\frac{\Gamma}{\overline{\rho}}\frac{\partial\tilde{\phi}_\alpha}{\partial x_j}\frac{\partial\tilde{\phi}_\alpha}{\partial x_j}\mathcal{F}_{\underline{\phi}}\right]+\frac{\partial}{\partial\psi_\alpha}\left[\omega\left(\psi_\alpha-\tilde{\phi}_\alpha\right)\mathcal{F}_{\underline{\phi}}\right]-\frac{\partial}{\partial\psi_\alpha}\left[S(\underline{\psi})\mathcal{F}_{\underline{\phi}}\right].\end{aligned}\tag{3.19}$$

3.1.3 Eulerian stochastic fields method

The traditional numerical solution approaches, such as finite-volume or finite-difference methods, fail to solve Eqs. (3.15) and (3.19) due to the large number

of dimensionality [100]. A feasible approach is the Monte Carlo based method, in which a set of stochastic fields is introduced to provide a discrete representation of the PDF. Take the modelled constant density PDF Eq. (3.15) for example, it is simplified to,

$$\begin{aligned}\frac{\partial}{\partial t}f_{\underline{\phi}}+\frac{\partial}{\partial x_j}\left(\langle u_j\rangle f_{\underline{\phi}}\right)-\frac{\partial}{\partial x_j}\left[(\Gamma+\Gamma_t)\frac{\partial f_{\underline{\phi}}}{\partial x_j}\right]=\\ -\frac{\partial}{\partial \psi_\alpha}\left[D_\alpha(\underline{\psi},\underline{x},t)f_{\underline{\phi}}\right]+\frac{1}{2}\frac{\partial^2}{\partial \psi_\alpha^2}\left[B_\alpha(\underline{\psi},\underline{x},t)f_{\underline{\phi}}\right],\end{aligned} \tag{3.20}$$

where the function D_α and B_α are the coefficients of the first and the second order derivatives in the composition space, e.g.,

$$\begin{aligned}B_\alpha(\underline{\psi},\underline{x},t)=&-2\Gamma\left\langle\frac{\partial\phi_\alpha}{\partial x_j}\right\rangle\left\langle\frac{\partial\phi_\alpha}{\partial x_j}\right\rangle,\\ D_\alpha(\underline{\psi},\underline{x},t)=&S(\underline{\psi})-\omega\left(\psi_\alpha-\langle\phi_\alpha\rangle\right)f_{\underline{\phi}}.\end{aligned} \tag{3.21}$$

3.1.3.1 Wiener process in a scalar- or vector-valued diffusion process

The terms in the R.H.S of the PDF transport equation, Eq. (3.20), are challenging to solve. The solution procedure of the Fokker–Planck equation [56] in Eq. (3.22) provides a general idea for solving the PDF transport equation based on Monte Carlo method.

$$\frac{\partial f(\xi;\underline{x},t)}{\partial t}=-\frac{\partial}{\partial\xi}\left[f(\xi;\underline{x},t)D(\xi,\underline{x},t)\right]+\frac{1}{2}\frac{\partial^2}{\partial\xi^2}\left[f(\xi,\underline{x},t)B(\xi,\underline{x},t)\right], \tag{3.22}$$

where the time evolution of an arbitrary quantity, $\xi=\xi(\underline{x},t)$, is introduced. $f(\xi;\underline{x},t)$ is the PDF of ξ, or denoted as f_ξ. The functions $D(\xi,\underline{x},t)$ and $B(\xi,\underline{x},t)$ are the drift and diffusion coefficients, representing the move and the diffusion of the PDF in the ξ space [101]. For brevity, they are denoted as D_ξ and B_ξ hereinafter. f_ξ has a discrete form, e.g.,

$$\begin{aligned}f(\xi;\underline{x},t+\Delta t)-f(\xi;\underline{x},t)=&-\frac{\partial}{\partial\xi}\left[f(\xi;\underline{x},t)D_\xi\Delta t\right]\\ &+\frac{1}{2}\frac{\partial^2}{\partial\xi^2}\left[f(\xi;\underline{x},t)B_\xi\Delta t\right],\end{aligned} \tag{3.23}$$

The discrete form in Eq. (3.23) is equivalent to the Taylor series expansion of an integral form in Eq. (3.24).

$$f(\xi;\underline{x},t+\Delta t)=\int f(\xi-\Delta\xi;\underline{x},t)g_{\Delta t}(\Delta\xi|\xi-\Delta\xi)d(\Delta\xi), \tag{3.24}$$

where $g_{\Delta t}(\Delta\xi|\xi_0)$ is a Gaussian PDF with a mean of $D(\xi_0, \underline{x}, t)\Delta t$ and variance of $B(\xi_0, \underline{x}, t)\Delta t$ [101]. $D(\xi_0, \underline{x}, t)$ and $B(\xi_0, \underline{x}, t)$ are then denoted as D_{ξ_0} and B_{ξ_0}, respectively.

Assuming that an existing stochastic fields system, $\xi^{(n)}$ $(n = 1, 2, ..., N)$, represents the f_ξ. $d\xi(\underline{x}, t)$ representing the PDF $f(\xi; \underline{x}, t + \Delta t) - f(\xi; \underline{x}, t)$ is equivalent to that the increasement of the stochastic field system $d\xi$ obeys the PDF of $g_{\Delta t}(\Delta\xi \mid \xi_0)$, i.e., $d\xi$ is a random variable, which follows the Gaussian distribution and has a conditional average and variance of $\langle d\xi|\xi_0\rangle = D_{\xi_0}\Delta t$ and $\left\langle [d\xi - D_\xi \Delta t]^2 \mid \xi_0 \right\rangle = B_{\xi_0}\Delta t$, respectively, when $\Delta t \to 0$.

The Wiener process, denoted as W, represents a continuous-time stochastic process. It is introduced to describe the random diffusion in the increasement of the stochastic field system $d\xi$. For instance, a finite number of independent standard normal random variables, $\eta^{(n)}$ $(n = 1, 2, ..., N)$, are observed from time $t = 0$ to $t = T$ at N uniform time steps. The time increase at each discrete time step is $\Delta t = \frac{T}{N}$. The increase of the Wiener term at $t_{n-1} = (n-1)\Delta t$ is defined as, $dW(t_{n-1}) = \sqrt{\Delta t}\eta^{(n)}, n = 1, 2, ..., N$. It has a feature that $W(t_n) - W(t_m)$ is a random variable obeying the Gaussian distribution with a mean value of 0 and variance of $t_n - t_m$.

$$\langle W(t_n) - W(t_m)\rangle = \sqrt{\Delta t} \sum_{i=m+1}^{n} \langle \eta^{(i)}\rangle = 0, \tag{3.25}$$

and

$$\begin{aligned}\left\langle [W(t_n) - W(t_m)]^2 \right\rangle =& \Delta t \sum_{i=m+1}^{n} \sum_{j=m+1}^{n} \left\langle \eta^{(i)}\eta^{(j)} \right\rangle \\ =& \Delta t(n - m) = t_n - t_m.\end{aligned} \tag{3.26}$$

Therefore, if the random variable is,

$$d\xi(\underline{x}, t) = D_\xi dt + \sqrt{B_\xi} dW. \tag{3.27}$$

This random variable, $d\xi(\underline{x}, t)$, represents the $f(\xi; \underline{x}, t+\Delta t) - f(\xi; \underline{x}, t)$ as it meets the requirements of a Gaussian variable with a conditional average and variance of $\langle d\xi|\xi_0\rangle = D_{\xi_0}\Delta t$ and $\left\langle [d\xi - D_\xi \Delta t]^2 \mid \xi_0 \right\rangle = B_{\xi_0}\Delta t$, respectively, when $\Delta t \to 0$. Eq. (3.27) is a stochastic differential equation (SPDE) for $\xi(\underline{x}, t)$. The Wiener process is then introduced in the solution procedure of the fine-grained PDF transport equation solving procedures.

The above-mentioned solution procedure is based on a scalar-valued diffusion process, while the transport of the composition PDF contains a vector-valued

diffusion process, where the drift coefficient is a vector and the diffusion coefficient is a matrix, e.g.,

$$\begin{aligned}\frac{\partial f(\underline{\xi};\underline{x},t)}{\partial t} &= -\frac{\partial}{\partial \xi_i}\left[f(\underline{\xi};\underline{x},t)D_i(\underline{\xi},\underline{x},t)\right] \\ &+\frac{1}{2}\frac{\partial^2}{\partial \xi_i \partial \xi_j}\left[f(\underline{\xi};\underline{x},t)B_{ij}(\underline{\xi},\underline{x},t)\right], \underline{\xi}(\underline{x},t) = (\xi_1,\xi_2,\ldots,\xi_N).\end{aligned} \tag{3.28}$$

According to Ref. [56], the SPDE for the vector $\underline{\xi}(\underline{x},t)$ is written as,

$$d\xi_i(\underline{x},t) = D_i(\underline{\xi},\underline{x},t)dt + b_{ij}(\underline{\xi},\underline{x},t)dW_j, b_{ik}b_{kj} = B_{ij}. \tag{3.29}$$

Here, b_{ij} is also a matrix derived from the symmetric matrix B_{ij}. It can be a non-symmetric matrix and not uniquely determined by B_{ij} [56]. The vector-valued Wiener process $\underline{W}$ is composed of the independent scalar-valued Wiener processes W_j, i.e., its increment is a joint normal random vector with mean $\langle dW_j \rangle = 0$ and covariance $\langle dW_i dW_j \rangle = dt\delta_{ij}$.

3.1.3.2 Diffusion and convection process

The terms in the L.H.S of the PDF transport equation, Eq. (3.20), involves the convection of the PDF. Considering the governing equation of a single scalar PDF f_ξ,

$$\frac{\partial}{\partial t}f_\xi + \frac{\partial}{\partial x_j}\left(\langle u_j \rangle f_\xi\right) - \frac{\partial}{\partial x_j}\left(\gamma \frac{\partial f_\xi}{\partial x_j}\right) = -\frac{\partial}{\partial \xi}\left(D_\xi f_\xi\right) + \frac{1}{2}\frac{\partial^2}{\partial \xi^2}\left(B_\xi f_\xi\right). \tag{3.30}$$

Assuming that the SPDE of a stochastic field $\xi(\underline{x},t)$ could replicate the PDF in Eq. (3.30),

$$\frac{\partial \xi}{\partial t} + \langle u_j \rangle \frac{\partial \xi}{\partial x_j} + v_j \circ \frac{\partial \xi}{\partial x_j} = D_\xi + \sqrt{B_\xi}\frac{d\hat{W}}{dt}, \tag{3.31}$$

where, $\hat{W}$ is a Wiener process; $\underline{v} = (v_1, v_2, v_3)$ is a stochastic velocity dependent of $\hat{W}$, $\circ$ denotes the stochastic product using the Stratonovitch interpretation, D_ξ and B_ξ are the drift and diffusion coefficient functions. According to Ref. [102], $\underline{v}$ does not directly correspond to the turbulent fluctuating velocity, and it does not necessarily respect the continuity constraint, and does not necessarily average to zero. Only two features are of interest for our purpose. 1) $\underline{v}$ models a velocity and thus should preserve the physical property of advection. 2) should yield the diffusion term present in Eq. (3.30).

The material derivative of ξ is denoted as $D\xi$,

$$D\xi = \frac{\partial \xi}{\partial t} dt + \langle u_j \rangle dt \frac{\partial \xi}{\partial x_j} + dv_j \circ \frac{\partial \xi}{\partial x_j}. \tag{3.32}$$

The material derivative of the corresponding fine-grained PDF (with the fine-grained PDF denoted as f'_ξ and its material derivative denoted as Df'_ξ), is derived,

$$Df'_\xi = df'_\xi + \langle u_j \rangle \frac{\partial f'_\xi}{\partial x_j} + dv_j \circ \frac{\partial f'_\xi}{\partial x_j}. \tag{3.33}$$

The PDF of ξ, denoted as f_ξ, is defined by considering that the fine-grained PDF function f'_ξ is averaged over an infinite number of realizations of the stochastic processes $d\underline{v}$ and $d\hat{W}$, i.e., $f_\xi = \left\langle \langle f'_\xi \rangle_v \right\rangle_{\hat{W}}$, in which $\langle \rangle_v$ and $\langle \rangle_{\hat{W}}$ denotes averaging over the realizations of $\underline{v}$ and $\hat{W}$, respectively.

$$Df_\xi = \left\langle \left\langle \frac{\partial f'_\xi}{\partial t} dt \right\rangle_v \right\rangle_{\hat{W}} + \left\langle \left\langle \langle u_j \rangle \frac{\partial f'_\xi}{\partial x_j} \right\rangle_v \right\rangle_{\hat{W}} + \left\langle \left\langle dv_j \circ \frac{\partial f'_\xi}{\partial x_j} \right\rangle_v \right\rangle_{\hat{W}} \tag{3.34}$$

in which,

$$\left\langle \left\langle \frac{\partial f'_\xi}{\partial t} dt \right\rangle_v \right\rangle_{\hat{W}} = \frac{\partial f_\xi}{\partial t} dt, \left\langle \left\langle \langle u_j \rangle \frac{\partial f'_\xi}{\partial x_j} \right\rangle_v \right\rangle_{\hat{W}} = \langle u_j \rangle \frac{\partial f_\xi}{\partial x_j}, \tag{3.35}$$

and using the Ito Stratonovitch correspondence [102],

$$X \circ dW = X(t + \frac{1}{2}dt) \left[W(t + dt) - W(t) \right] = XdW + \frac{1}{2} dX dW. \tag{3.36}$$

One has,

$$\begin{aligned}
&\left\langle \left\langle dv_j \circ \frac{\partial f'_\xi}{\partial x_j} \right\rangle_v \right\rangle_{\hat{W}} \\
&= \left\langle \left\langle dv_j \frac{\partial f'_\xi}{\partial x_j} + \frac{1}{2} d \left(\frac{\partial f'_\xi}{\partial x_j} \right) dv_j \right\rangle_v \right\rangle_{\hat{W}} \\
&= \left\langle \left\langle dv_j \frac{\partial f'_\xi}{\partial x_j} - \frac{\partial}{\partial x_j} \left(\frac{1}{2} dv_j dv_k \frac{\partial f'_\xi}{\partial x_k} \right) + \frac{1}{2} dv_k \frac{\partial dv_j}{\partial x_j} \frac{\partial f'_\xi}{\partial x_k} \right\rangle_v \right\rangle_{\hat{W}} \\
&= \left\langle \left\langle dv_j \frac{\partial f'_\xi}{\partial x_j} \right\rangle_v - \left\langle \frac{\partial}{\partial x_j} \left(\frac{1}{2} dv_j dv_k \frac{\partial f'_\xi}{\partial x_k} \right) \right\rangle_v + \left\langle \frac{1}{2} dv_k \frac{\partial dv_j}{\partial x_j} \frac{\partial f'_\xi}{\partial x_k} \right\rangle_v \right\rangle_{\hat{W}} \\
&= \langle dv_j \rangle \frac{\partial f_\xi}{\partial x_j} - \frac{\partial}{\partial x_j} \left(\frac{1}{2} \langle dv_j dv_k \rangle \frac{\partial f_\xi}{\partial x_k} \right) + \frac{1}{2} \left\langle dv_k \frac{\partial dv_j}{\partial x_j} \right\rangle \frac{\partial f_\xi}{\partial x_k}.
\end{aligned} \tag{3.37}$$

Therefore, the material derivative Df'_ξ is,

$$\begin{aligned} Df'_\xi =& \frac{\partial f_\xi}{\partial t}dt + \langle u_j \rangle \frac{\partial f_\xi}{\partial x_j} + \langle dv_j \rangle \frac{\partial f_\xi}{\partial x_j} + \frac{1}{2}\left\langle dv_k \frac{\partial dv_j}{\partial x_j} \right\rangle \frac{\partial f_\xi}{\partial x_k} \\ & - \frac{\partial}{\partial x_j}\left(\frac{1}{2}\langle dv_j dv_k \rangle \frac{\partial f_\xi}{\partial x_k} \right). \end{aligned} \tag{3.38}$$

On the other hand, taking Eq. (3.31) into consideration, the material derivative of ξ can also be written as,

$$\begin{aligned} D\xi =& \frac{\partial \xi}{\partial t}dt + \langle u_j \rangle dt \frac{\partial \xi}{\partial x_j} + dv_j \circ \frac{\partial \xi}{\partial x_j} \\ =& D_\xi dt + \sqrt{B_\xi} d\hat{W}, \end{aligned} \tag{3.39}$$

which is a diffusion process. According to Section 3.1.3.1, it has a PDF formulation,

$$Df_\xi = -\frac{\partial}{\partial \xi}\left(D_\xi f_\xi \right) + \frac{1}{2}\frac{\partial^2}{\partial \xi^2}\left(B_\xi f_\xi \right), \tag{3.40}$$

Combining Eqs. (3.38) and (3.40), the governing equation of $f(\xi)$ is given, i.e.,

$$\begin{aligned} & \frac{\partial f_\xi}{\partial t}dt + \langle u_j \rangle \frac{\partial f_\xi}{\partial x_j} + \langle dv_j \rangle \frac{\partial f_\xi}{\partial x_j} + \frac{1}{2}\left\langle dv_k \frac{\partial dv_j}{\partial x_j} \right\rangle \frac{\partial f_\xi}{\partial x_k} \\ & - \frac{\partial}{\partial x_j}\left(\frac{1}{2}\langle dv_j dv_k \rangle \frac{\partial f_\xi}{\partial x_k} \right) = -\frac{\partial}{\partial \xi}\left(D_\xi f_\xi \right) + \frac{1}{2}\frac{\partial^2}{\partial \xi^2}\left(B_\xi f_\xi \right). \end{aligned} \tag{3.41}$$

Once the following constraints are satisfied, the Eq. (3.41) is identical to Eq. (3.30),

$$\begin{aligned} \frac{1}{2dt}\langle dv_i dv_j \rangle &= \gamma \delta_{ij}, \\ \frac{\langle dv_j \rangle}{dt} + \frac{1}{2dt}\left\langle dv_j \frac{\partial dv_i}{\partial x_i} \right\rangle &= 0. \end{aligned} \tag{3.42}$$

According to Ref. [102], the temporal increment of the stochastic velocity, $d\underline{v} = (dv_1, dv_2, dv_3)$, can be decomposed as,

$$dv_j = u_j^d dt + u_j^g dt, \tag{3.43}$$

where u_j^d is a deterministic drift component and u_j^g is a Gaussian random component of the velocity.

Therefore, the above constraints are equivalent to,

$$\begin{aligned}\left\langle u_i^d u_j^d dt\right\rangle + \left\langle u_i^d u_j^g dt\right\rangle + \left\langle u_i^g u_j^d dt\right\rangle + \left\langle u_i^g u_j^g dt\right\rangle &= 2\gamma\delta_{ij},\\ \langle u_j^d\rangle + \langle u_j^g\rangle + \frac{1}{2}\left\langle (u_j^d + u_j^g)\frac{\partial(u_i^d dt + u_i^g dt)}{\partial x_i}\right\rangle &= 0,\end{aligned} \tag{3.44}$$

where $\langle u_j^d\rangle = u_j^d$, $\langle u_j^g\rangle = 0$, $\langle u_i^d u_j^d dt\rangle \sim O(dt)$, $\langle u_i^g u_j^g dt\rangle \sim O(1)$. Thus,

$$\begin{aligned}\left\langle u_i^g u_j^g\right\rangle dt &= 2\gamma\delta_{ij},\\ u_j^d &= -\frac{1}{2}\left\langle \frac{\partial u_i^g}{\partial x_i} u_j^g\right\rangle dt.\end{aligned} \tag{3.45}$$

One of the solution is

$$\begin{aligned}u_j^g &= -\sqrt{2\gamma}\frac{dW_j}{dt},\\ u_j^d &= -\frac{\partial\gamma}{\partial x_j}.\end{aligned} \tag{3.46}$$

The infinitesimal increment in ξ is denoted as $d\xi$,

$$d\xi = -\langle u_j\rangle\frac{\partial\xi}{\partial x_j}dt + \frac{\partial}{\partial x_j}\left(\gamma\frac{\partial\xi}{\partial x_j}\right)dt + \sqrt{2\gamma}\frac{\partial\xi}{\partial x_j}dW_j + D_\xi dt + \sqrt{B_\xi}d\hat{W} \tag{3.47}$$

3.1.3.3 The ESF formulation

As suggested by Eqs. (3.29) and (3.47), the composition PDF $f_{\underline{\phi}}$ is represented by N_{sf} number of stochastic fields, $\xi_\alpha^{(n)} = \xi_\alpha^{(n)}(\underline{x}, t)$, $(n = 1, 2, ..., N_{sf})$. The solutions of Eq. (3.15) are approximated by

$$f_{\underline{\phi}}(\underline{\psi}; \underline{x}, t) \approx \frac{1}{N_{sf}}\sum_{n=1}^{N_{sf}}\left[\prod_{\alpha=1}^{N}\delta\left(\psi_\alpha - \xi_\alpha^{(n)}\right)\right], \tag{3.48}$$

$$\phi_\alpha(\underline{x}, t) \approx \frac{1}{N_{sf}}\sum_{n=1}^{N_{sf}}\xi_\alpha^{(n)}. \tag{3.49}$$

The evolution of $\xi_\alpha^{(n)}$ are governed by a set of SPDEs, which is written as follows by comparing Eq. (3.20) with Eq. (3.30) and using Eq. (3.47),

$$\begin{aligned}d\xi_\alpha^{(n)} =& -\langle u_j\rangle\frac{\partial\xi_\alpha^{(n)}}{\partial x_j}dt + \frac{\partial}{\partial x_j}\left[(\Gamma + \Gamma_t)\frac{\partial\xi_\alpha^{(n)}}{\partial x_j}\right] + \sqrt{2(\Gamma + \Gamma_t)}\frac{\partial\xi_\alpha^{(n)}}{\partial x_j}dW_j\\ &+ D_\alpha(\xi_\alpha^{(n)}, \underline{x}, t)dt + \sqrt{B_\alpha(\xi_\alpha^{(n)}, \underline{x}, t)}d\hat{W}_\alpha,\end{aligned} \tag{3.50}$$

where, $\underline{W}$ and $\underline{\hat{W}}$ are independent Wiener vectors.

The α-th component of the drift coefficient is,

$$D_\alpha(\xi_\alpha^{(n)}, \underline{x}, t) = S(\underline{\xi}^{(n)}) - \omega\left(\xi_\alpha^{(n)} - \langle\xi_\alpha^{(n)}\rangle\right), \tag{3.51}$$

where, $\underline{\xi}^{(n)} = (\xi_1^{(n)}, \xi_2^{(n)}, \ldots, \xi_N^{(n)})$.

The diffusion coefficient is,

$$B_\alpha(\xi_\alpha^{(n)}, \underline{x}, t) = -2\Gamma\left\langle\frac{\partial\xi_\alpha^{(n)}}{\partial x_j}\right\rangle\left\langle\frac{\partial\xi_\alpha^{(n)}}{\partial x_j}\right\rangle. \tag{3.52}$$

Therefore, the SPDEs of the Eulerian stochastic fields (ESF) system, $\xi_\alpha^{(n)}(\underline{x}, t)$, are given as below:

$$\begin{aligned} d\xi_\alpha^{(n)} = &-\langle u_j\rangle\frac{\partial\xi_\alpha^{(n)}}{\partial x_j}dt + \frac{\partial}{\partial x_j}\left[(\Gamma+\Gamma_t)\frac{\partial\xi_\alpha^{(n)}}{\partial x_j}\right]dt \\ &+\sqrt{2(\Gamma+\Gamma_t)}\frac{\partial\xi_\alpha^{(n)}}{\partial x_j}dW_j + \sqrt{-2\Gamma\left\langle\frac{\partial\xi_\alpha^{(n)}}{\partial x_j}\right\rangle\left\langle\frac{\partial\xi_\alpha^{(n)}}{\partial x_j}\right\rangle}d\hat{W}_\alpha \\ &-\omega\left(\xi_\alpha^{(n)} - \langle\xi_\alpha^{(n)}\rangle\right)dt \\ &+S(\underline{\xi}^{(n)})dt. \end{aligned} \tag{3.53}$$

It is written in increment form to emphasize that stochastic term is not differentiable with respect to time [52]. It is also worth mentioning that all the scalars are convected together by the turbulent transport without differential diffusion [103].

In the same manner, for the inhomogeneous variable-density flows, the modelled transport equation of the composition MDF, Eq. (3.19), can also be solved using the Monte Carlo based method. The governing equations of the stochastic fields in ESF $\xi_\alpha^{(n)}(\underline{x}, t)$ are:

$$\begin{aligned} \overline{\rho}d\xi_\alpha^{(n)} = &-\overline{\rho}\tilde{u}_j\frac{\partial\xi_\alpha^{(n)}}{\partial x_j}dt + \frac{\partial}{\partial x_j}\left[(\Gamma+\Gamma_t)\frac{\partial\xi_\alpha^{(n)}}{\partial x_j}\right]dt \\ &+\overline{\rho}\sqrt{2\frac{\Gamma+\Gamma_t}{\overline{\rho}}}\frac{\partial\xi_\alpha^{(n)}}{\partial x_j}dW_j + \overline{\rho}\sqrt{-2\frac{\Gamma}{\overline{\rho}}\left\langle\frac{\partial\xi_\alpha^{(n)}}{\partial x_j}\right\rangle\left\langle\frac{\partial\xi_\alpha^{(n)}}{\partial x_j}\right\rangle}d\hat{W}_\alpha \\ &-\overline{\rho}\omega\left(\xi_\alpha^{(n)} - \langle\xi_\alpha^{(n)}\rangle\right)dt \\ &+\overline{\rho}S(\underline{\xi}^{(n)})dt. \end{aligned} \tag{3.54}$$

3.1.4 Solving the ESF transport equations for reacting flow

In the LES of reacting flows, the composition spaces are species mass fractions and sensible enthalpy. The ESF method is coupled with the conventional LES using the following procedure.

1. The filtered continuity equation and momentum equations, Eqs. (2.15) and (2.16), are solved first to calculate $\tilde{u}_j$, Γ_t, and ω.

2. Instead of solving the filtered species and energy transport equations, Eqs. (2.17) and (2.18), the MDF transport equation, Eq. (3.19), is solved. Assuming that N_S is the number of species, $N_S + 1$ scalar transport equations need to be solved in conventional LES. In ESF/LES method, the number of scalar transport equations to be solved is $N_{sf}(N_S + 1)$, where N_{sf} is the number of stochastic fields.

3. The filtered species mass fractions and sensible enthalpy are retrieved from the ensemble average of the stochastic field $\xi_\alpha^{(n)}$ ($\alpha = 1, 2, \ldots, N_S + 1$; $n = 1, 2, \ldots, N_{sf}$), e.g., $\langle \underline{\xi}^{(n)} \rangle = (\tilde{Y}_1, \tilde{Y}_2, \ldots, \tilde{Y}_{N_S}, \tilde{h})$. The filtered mean values will be used in the IEM model, as shown in Eq. (3.14).

The stochastic fields system is governed by Eq. (3.54). As the Wiener process is introduced, the numerical solution procedures of Eq. (3.54) are different from that in the conventional species mass fraction and the sensible enthalpy transport equations. The detailed solution procedures are discussed in the following section.

3.2 Theoretical and numerical consistency

In the simulation of multi-species reacting flows, a unity Lewis number is implied in Eq. (3.8), in which each ϕ_α shares the same diffusion coefficient. By considering the differential molecular diffusion, the new formulation of the PDF equation is obtained from the mean of the fine-grained PDF transport Eq. (3.7).

$$\begin{aligned} \frac{\partial}{\partial t} f_{\underline{\phi}} + \frac{\partial}{\partial x_j} \left[\langle u_j \mid \underline{\psi} \rangle f_{\underline{\phi}} \right] = \\ -\frac{\partial}{\partial \psi_\alpha} \left[\left\langle \frac{\partial}{\partial x_j} \left(\Gamma_\alpha \frac{\partial \phi_\alpha}{\partial x_j} \right) \middle| \underline{\psi} \right\rangle f_{\underline{\phi}} \right] - \frac{\partial S(\underline{\psi}) f_{\underline{\phi}}}{\partial \psi_\alpha}, \end{aligned} \tag{3.55}$$

in which Γ_α is dependent of the location but independent of composition, i.e. $\langle\Gamma_\alpha\rangle = \Gamma_\alpha$. The conditional average terms are closed using the Eqs. (3.11), (3.13), (3.56) and the new IEM model, Eq. (3.57), proposed by Wang *et al.* [104].

$$\begin{aligned}\left\langle \frac{\partial}{\partial x_j}\left(\Gamma_\alpha \frac{\partial \phi_\alpha}{\partial x_j}\right) \middle| \underline{\psi} \right\rangle =& \frac{\partial}{\partial x_j}\left(\Gamma_\alpha \left\langle \frac{\partial \phi_\alpha}{\partial x_j} \right\rangle\right) \\ &+ \left\langle \frac{\partial}{\partial x_j}\left(\Gamma_\alpha \frac{\partial \phi'_\alpha}{\partial x_j}\right) \middle| \underline{\psi} \right\rangle,\end{aligned} \tag{3.56}$$

$$\left\langle \frac{\partial}{\partial x_j}\left(\Gamma_\alpha \frac{\partial \phi'_\alpha}{\partial x_j}\right) \middle| \underline{\psi} \right\rangle f_{\underline{\phi}} = -\omega\left(\psi_\alpha - \langle\phi_\alpha\rangle\right) f_{\underline{\phi}}. \tag{3.57}$$

The modelled PDF transport equation with differential molecular diffusion is written as

$$\begin{aligned}&\frac{\partial}{\partial t} f_{\underline{\phi}} + \frac{\partial}{\partial x_j}\left(\langle u_j\rangle f_{\underline{\phi}}\right) - \frac{\partial}{\partial x_j}\left(\Gamma_t \frac{\partial f_{\underline{\phi}}}{\partial x_j}\right) = \\ &-\frac{\partial}{\partial \psi_\alpha}\left[\frac{\partial}{\partial x_j}\left(\Gamma_\alpha \left\langle \frac{\partial \phi_\alpha}{\partial x_j} \right\rangle\right) f_{\underline{\phi}}\right] + \frac{\partial}{\partial \psi_\alpha}\left[\omega\left(\psi_\alpha - \langle\phi_\alpha\rangle\right) f_{\underline{\phi}}\right] - \frac{\partial S(\underline{\psi}) f_{\underline{\phi}}}{\partial \psi_\alpha}.\end{aligned} \tag{3.58}$$

Therefore, the SPDEs of the ESF system, $\xi_\alpha^{(n)}(\underline{x}, t)$, are given as below:

$$\begin{aligned}d\xi_\alpha^{(n)} =& -\langle u_j\rangle \frac{\partial \xi_\alpha^{(n)}}{\partial x_j} dt + \frac{\partial}{\partial x_j}\left(\Gamma_t \frac{\partial \xi_\alpha^{(n)}}{\partial x_j}\right) dt + \frac{\partial}{\partial x_j}\left(\Gamma_\alpha \left\langle \frac{\partial \xi_\alpha^{(n)}}{\partial x_j} \right\rangle\right) dt \\ &+ \sqrt{2\Gamma_t} \frac{\partial \xi_\alpha^{(n)}}{\partial x_j} dW_j \\ &- \omega\left(\xi_\alpha^{(n)} - \langle \xi_\alpha^{(n)}\rangle\right) dt \\ &+ S(\underline{\xi}^{(n)}) dt.\end{aligned} \tag{3.59}$$

3.2.1 Theoretical consistency

The ESF method was originally developed by Valiño [88] in 1998, Sabel'nikov and Soulard [102] in 2005 based on the Itô and Stratonovitch interpretation, respectively. It is proved that both formulations are statistically equivalent [102].

The mathematical consistency between the solution of the ESF method and that from the original transported PDF equation has been discussed recently [100,

103–105]. It is expected that PDF derived from the equation of SPDE is identical to PDF equation, i.e., the numerical solutions of the ESF method converge asymptotically to the true solution when the numerical parameters reach their limits. However, Valiño *et al.* [103] reported that the original formulation (denoted as ESF-V98) [88] has some small inconsistencies because it has a non-zero stochastic term, $\mathcal{W} = \sqrt{2(\Gamma + \Gamma_t)}\frac{\partial \xi_\alpha^{(n)}}{\partial x_j} dW_j$ in the laminar limit when $\Gamma_t \to 0$. The inconsistency in the ESF method means that when numerical parameters reach their limits, i.e., $\mathrm{N}_{sf} \to \infty$ and $\Delta t \to 0$, the ESF solution does not fully converge to the true solution of the PDF transport equation. In the same study [103], Valiño *et al.* also introduced a modified formulation (denoted as ESF-V16) to address the spurious variance production in the original method. Recently, Wang *et al.* [100, 104] systematically investigated the consistency of the ESF methods and revealed that none of the existing formulations is fully consistent with the PDF transport equation. It was shown that the consistency of the ESF-V16 method is achieved for the mean field, but for higher moments certain correction terms should be included in the SPDE to achieve consistency of the method [100]. Therefore, Wang *et al.* [104] proposed two fully consistent ESF formulations. The first form has limited practical value as it involves complex number calculations. Here, only the second form is discussed, denoted as ESF-W21.

Table 3.1 shows the above-mentioned ESF formulations and a formulation we derived in Eq. (3.53), denoted as ESF-X21. All of the existing ESF formulations share a similar form,

$$d\xi_\alpha^{(n)} = \mathcal{C} + \mathcal{D} + \mathcal{W} + \mathcal{M} + \mathcal{S}. \tag{3.60}$$

where $\mathcal{C}$, $\mathcal{D}$, $\mathcal{W}$, $\mathcal{M}$ and $\mathcal{S}$ are convection, diffusion, stochastic and reaction source terms, in which $\mathcal{C}$ and $\mathcal{S}$ are the same, e.g.,

$$\mathcal{C} = -\langle u_j \rangle \frac{\partial \xi_\alpha^{(n)}}{\partial x_j} dt, \mathcal{S} = S(\underline{\xi}^{(n)}) dt, \tag{3.61}$$

The differences locate at the $\mathcal{W}$, $\mathcal{D}$ and $\mathcal{M}$ terms, cf. Table 3.1. The $\mathcal{M}$ term follows the IEM model, e.g.,

$$\mathcal{M} = -\omega \left(\xi_\alpha^{(n)} - \langle \xi_\alpha^{(n)} \rangle \right) dt \tag{3.62}$$

in which ω is the scalar mixing frequency, which has different meanings in the derivation procedures.

In the next chapter, the performance of the ESF formulations, ESF-V98, ESF-V16, and ESF-W21, will be shown. The ESF-X21 is not examined as it involves

the complex number, which comes from the negative square root of the coefficient in the $\mathcal{W}$ term. This makes the use of the formulation in numerical analysis complicated and the interpretation of the numerical results difficult. The similar complex number problem is also reported in another fully consistent formulation in Ref. [104].

Table 3.1: The existing ESF formulations.

	$\mathcal{W}$	$\mathcal{D}$	Ref.
ESF-V98	$\sqrt{2(\Gamma_t+\Gamma)}\frac{\partial\xi_\alpha^{(n)}}{\partial x_j}dW_j^{(n)}$	$\frac{\partial}{\partial x_j}\left((\Gamma_t+\Gamma)\frac{\partial\xi_\alpha^{(n)}}{\partial x_j}\right)dt$	[88]
ESF-V16	$\sqrt{2\Gamma_t}\frac{\partial\xi_\alpha^{(n)}}{\partial x_j}dW_j^{(n)}$	$\frac{\partial}{\partial x_j}\left((\Gamma_t+\Gamma)\frac{\partial\xi_\alpha^{(n)}}{\partial x_j}\right)dt$	[103]
ESF-W21	$\sqrt{2\Gamma_t}\frac{\partial\xi_\alpha^{(n)}}{\partial x_j}dW_j^{(n)}$	$\frac{\partial}{\partial x_j}\left(\Gamma_t\frac{\partial\xi_\alpha^{(n)}}{\partial x_j}+\Gamma\left\langle\frac{\partial\xi_\alpha^{(n)}}{\partial x_j}\right\rangle\right)dt$	[104]
ESF-X21	$\sqrt{2(\Gamma+\Gamma_t)}\frac{\partial\xi_\alpha^{(n)}}{\partial x_j}dW_j+\sqrt{-2\Gamma\left\langle\frac{\partial\xi_\alpha^{(n)}}{\partial x_j}\right\rangle\left\langle\frac{\partial\xi_\alpha^{(n)}}{\partial x_j}\right\rangle}d\hat{W}_\alpha$	$\frac{\partial}{\partial x_j}\left((\Gamma_t+\Gamma)\frac{\partial\xi_\alpha^{(n)}}{\partial x_j}\right)dt$	present

3.2.2 Numerical consistency

The aforementioned ESF formulations eliminate the theoretical inconsistency of the original ESF-V98 method under ideal conditions, e.g., using an infinite number of stochastic fields and infinitesimal time step. However, in practice, the number of stochastic fields is not infinite, the same for the time step Δt in numerical simulations. A numerical inconsistency arises in the ESF method due to the nature of Monte Carlo based methods [81, 106].

In the ESF method, the PDF is approximated by a finite number of stochastic fields governed by the SPDE. The stochastic fields do not represent any particular realization of the real field. It is expected that in the limit of an infinite number of stochastic fields the true PDF is obtained. However, this approximation is accompanied by a statistical error, which has an order of $\frac{1}{\sqrt{N_{sf}}}$, i.e. $\mathcal{O}(\frac{1}{\sqrt{N_{sf}}})$. The error leads to numerical instability and accumulative errors in results [106, 107], especially for the modelling of reactive scalars in turbulent reacting flow simulations. The reactive scalars, e.g., mass fractions of species or temperature, should be bounded (the mass fractions should be between 0 and 1 and temperature should be lower than the adiabatic flame temperature) since these scalars are used in the calculation of reaction rates that are highly non-

linear functions of temperature. For the single-step reaction adiabatic premixed flame that is described with a single scalar (i.e., the reaction progress variable), it was shown that the scalar is bounded [88]. However, in general, there is no guarantee that the reactive scalars are bounded to their physically meaningful range. Garmory [108] suggested that the maximum incremental contribution of the Wiener term should be restricted to bound the scalar to be within its upper and lower physical limits. This could be done by limiting the numerical integration time step to smaller values that are dynamically determined locally. Prasad [107] suggested solving the auxiliary mean fields of the scalars to filter the noise from stochastic fields. Avdić *et al.* [106] proposed a weighted function to remove the stochastic noise by weighting the first moment value from stochastic fields and the auxiliary mean fields transport equations. Pant *et al.* [109] presented a gradient limiter to directly suppress the Wiener process to avoid the possible rapid change of the scalars. Nevertheless, when the reactive scalars are bounded within their physical limits, there is still an issue that the element mass conservation may not be satisfied in ESF modelling of the multi-species turbulent combustion process. To the best of the authors' knowledge, the issue of element mass conservation is not well addressed yet.

In the following section, the consistency of the ESF method for the element mass conservation in simulations of turbulent combustion of multi-species and multi-step chemistry are investigated. The three-step factorization scheme is presented for the implementation of the ESF method. Moreover, a novel correction method is proposed to remove the numerical error in the element mass conservation.

3.3 Implementation and improvements of ESF

3.3.1 Factorization Scheme

The aforementioned SPDEs are solved with a three-step factorization scheme proposed by Jones *et al.* [110]. A brief description of the factorization scheme is given here, since the developed modification method is based on this scheme. The first step involves the integration of convection and diffusion terms using an implicit scheme and Wiener term using an explicit scheme with the solution being advanced according to

$$\xi_\alpha^{(n)(1)} = \xi_\alpha^{(n)}(t_n) + \mathcal{C}(\xi_\alpha^{(n)(1)}) + \mathcal{D}(\xi_\alpha^{(n)(1)}) + \mathcal{W}(\xi_\alpha^{(n)}(t_n)), \tag{3.63}$$

where superscript (1) indicates the results after the first step. Time t_n indicates results at time step t_n.

Before the second step (integration of the micro-mixing process), the mean fields are updated from the solution of Eq. (3.63) by applying Eq. (3.49), i.e.,

$$\phi_\alpha^{(1)} = \frac{1}{N_{sf}} \sum_{n=1}^{N_{sf}} \xi_\alpha^{(n)(1)}.$$

The IEM micro-mixing process is integrated analytically [108] in the second step:

$$\xi_\alpha^{(n)(2)} = \phi_\alpha^{(1)} + \left(\xi_\alpha^{(n)(1)} - \phi_\alpha^{(1)} \right) e^{-\frac{1}{2} C_\phi \omega^{sgs} \Delta t}. \tag{3.64}$$

The final step is the integration of the chemical source term based on the solution of the second step,

$$\xi_\alpha^{(n)}(\mathbf{x}, t_n + \Delta t) = \xi_\alpha^{(n)(2)} + \mathcal{S}(\underline{\xi}^{(n)(2)}; \Delta t), \tag{3.65}$$

where $\mathcal{S}(\underline{\xi}^{(n)(2)}; \Delta t)$ denotes the integration of the chemical reaction rates within the time interval of Δt, using a finer chemical time step.

Finally, the mean fields are obtained by applying Eq. (3.49),

$$\phi_\alpha(\mathbf{x}, t_n + \Delta t) = \frac{1}{N_{sf}} \sum_{n=1}^{N_{sf}} \xi_\alpha^{(n)}(\mathbf{x}, t_n + \Delta t).$$

As stated in Ref. [110], the factorization scheme is more stable than the previous scheme used by Jones *et al.* [87, 111]. This is largely attributed to the smoothing effect of the micro-mixing process, which eliminates some non-physical values of the scalar due to the large Wiener term before the chemical reactions.

3.3.2 Modified ESF Method

The factorization scheme is modified to fulfil element mass conservation by employing two corrections. First, a mean field of ϕ_α^* is computed by integrating the convective and diffusive terms of the mean field, following the suggestion of Avdić *et al.* [106],

$$\phi_\alpha^{*(1)} = \phi_\alpha(t_n) + \mathcal{C}(\phi_\alpha^{*(1)}) + \mathcal{D}(\phi_\alpha^{*(1)}). \tag{3.66}$$

The difference is that the method in Ref. [106] is based on the flamelet generated manifolds (FGM) model, in which the chemistry is tabulated. It can be shown that $\phi_\alpha^{*(1)}$ satisfies the mass conservation law.

The first step of the modified factorization scheme is identical to that of the original scheme presented in Section 3.3.1, Eq. (3.63),

$$\xi_\alpha^{(n)(1)} = \xi_\alpha^{(n)}(t_n) + \mathcal{C}(\xi_\alpha^{(n)(1)}) + \mathcal{D}(\xi_\alpha^{(n)(1)}) + \mathcal{W}(\xi_\alpha^{(n)}(t_n)).$$

It can be shown that, when $N_{sf} \to \infty$,

$$\sum_{n=1}^{N_{sf}} \mathcal{W}(\underline{\xi}^{(n)}(t_n)) \to 0, \frac{1}{N_{sf}} \sum_{n=1}^{N_{sf}} \xi_\alpha^{(n)(1)} \to \phi_\alpha^{*(1)}.$$

When the number of stochastic fields N_{sf} is finite, a mass conservation error arises due to the Wiener term. Define an error term $\mathcal{E}$ as,

$$\mathcal{E} = \tfrac{1}{N_{sf}} \textstyle\sum_{n=1}^{N_{sf}} \xi_\alpha^{(n)(1)} - \phi_\alpha^{*(1)}. \tag{3.67}$$

It is clear that $\mathcal{E} \to 0$ as $N_{sf} \to \infty$. To remove the error, a correction step is proposed,

$$\xi_\alpha^{(n)(2)} = \xi_\alpha^{(n)(1)} - \mathcal{E}. \tag{3.68}$$

It can be shown that regardless the number of stochastic fields,

$$\frac{1}{N_{sf}} \sum_{n=1}^{N_{sf}} \xi_\alpha^{(n)(2)} = \phi_\alpha^{*(1)}.$$

After the correction step, the IEM micro-mixing process is integrated. This step is similar to that given in Eq. (3.64),

$$\xi_\alpha^{(n)(3)} = \phi_\alpha^{*(1)} + \left(\xi_\alpha^{(n)(2)} - \phi_\alpha^{*(1)}\right) e^{-\frac{1}{2} C_\phi \omega^{sgs} \Delta t}. \tag{3.69}$$

To ensure that the mass fraction of each species strictly lies in [0,1], we introduce a second correction step,

$$\begin{aligned} &\xi_\alpha^{(n)(4)} = \phi_\alpha^{*(1)} + \beta_\alpha(\xi_\alpha^{(n)(3)} - \phi_\alpha^{*(1)}), \\ &\beta_\alpha = \min(1, |\tfrac{\phi_\alpha^{*(1)}}{\phi_\alpha^{*(1)} - \xi_\alpha^{(n)(3)}}|, |\tfrac{\phi_\alpha^{*(1)} - 1}{\phi_\alpha^{*(1)} - \xi_\alpha^{(n)(3)}}|), (n = 1, ..., N_{sf}), \end{aligned} \tag{3.70}$$

where β_α is the minimum of the three terms in the bracket, at a given spatial location and for a given α, among all stochastic fields.

In the final step, integration of the chemical source term is done based on the field $\xi_\alpha^{(n)(4)}$,

$$\begin{aligned} &\xi_\alpha^{(n)}(t_n + \Delta t) = \xi_\alpha^{(n)(3)} + \mathcal{S}(\underline{\xi}^{(n)(4)}; \Delta t), \\ &\phi_\alpha(t_n + \Delta t) = \phi_\alpha^{*(1)} + \tfrac{1}{N_{sf}} \textstyle\sum_{n=1}^{N_{sf}} \mathcal{S}(\underline{\xi}^{(n)(4)}; \Delta t). \end{aligned} \tag{3.71}$$

The above-mentioned solution procedure is independent of the turbulence model. It is applicable for both RANS and LES. The difference is that Γ_α represents the sub-grid eddy diffusivity in LES. For brevity, the original ESF procedure and the modified one with corrections are referred to as ESF-O and ESF-C, respectively. The detailed comparison of the ESF-O and ESF-C are available in Paper IV.

Chapter 4

Study of ESF model for simulation of multi-mode combustion

In this chapter, the developed ESF method is employed in the one-dimensional (1-D) premixed turbulent flames, non-premixed turbulent flames, and three-dimensional (3-D) spray flames simulations to investigate its performance. The different ESF formulations, ESF-V98, ESF-V16, and ESF-W21 derived in the previous chapter, the element mass conservation issues, and the comparison of ESF with WSR and PaSR in the spray flames are presented.

4.1 Premixed flame

In this section, turbulent premixed flames are studied using the ESF method. The case setup is based on a direct numerical simulation (DNS) [112], in which a fuel-lean (equivalence ratio ϕ of 0.6) methane-air flame is freely propagated in turbulent flow environments with different turbulence intensities. The premixed flame is initialized from an infinitely large flat flame profile, which is obtained from a 1-D laminar freely propagating flame under atmospheric pressure. It evolves to be a 3-D turbulent flame in a pre-calculated turbulent environment. The turbulence intensity is characterized using a dimensionless number, Karlovitz number (Ka), which is defined as the ratio of the smallest turbulent time scales, i.e., Kolmogorov timescale, to the chemical timescale. For more information, readers are referred to Refs. [112, 113].

Table 4.1: Specification of premixed turbulent flame cases for one-dimensional unsteady RANS simulations.

Case	u' [m/s]	l_0 [mm]	η [μm]	k [m^2/s^2]	ϵ [m^2/s^3]	ν_t [s^2/m]	ω [1/s]
Laminar	0	-	-	-	-	-	-
K4	0.3	0.70	90	0.135	6.24E1	2.63E-5	4.62E2
K100	2.2	0.52	26	7.260	8.96E3	5.29E-4	1.23E3
K800	8.1	0.43	9.4	98.42	5.25E5	1.66E-3	5.33E3
K4100	25	0.48	4.2	937.5	1.32E7	5.99E-3	1.40E4

4.1.1 Case Specification

As the turbulence field is statistically stationary, the aforementioned turbulent premixed flames are statistically planar [113], i.e., it is a statistical 1-D flame. Therefore, 1-D unsteady RANS simulations are carried out to study the statistical characteristics, e.g., turbulent flame speed and flame thickness. The standard k–ϵ model is employed for turbulence closure. The ESF models with different formulations, ESF-V98, ESF-V16, and ESF-W21 derived in the previous chapter, are adopted to study the performance of the ESF model on the prediction of turbulent premixed flames. The focus is to study the capability of the ESF model in the prediction of turbulent premixed flames and the differences between different formulations. Three hypotheses are proposed to simplify the simulations: (1) a two-step BFER's mechanism [114], which consists of 6 species and 2 global reactions (fuel oxidation and CO–CO_2 equilibrium), is used to model the chemistry of the fuel-lean methane-air flame; (2) the flow is simplified to be constant-density to keep the calculations stable, because that the simulations using ESF-V98 formulation diverge in the variable-density flows under the low Ka conditions; (3) the turbulence characteristics are assumed to be constant in each simulation, i.e., k and ϵ are independent of time and location.

Table 4.1 shows the studied cases and the key parameters of the turbulence flows with Ka numbers varying from 0 to 4100. The RMS velocity fluctuation, u', integral length scale, l_0, and the Kolmogorov length scale, η, are obtained from the DNS in Ref. [113]. The turbulent kinetic energy, k, dissipation rate, ϵ, turbulent viscosity, ν_t, and the scalar mixing frequency, ω, in the RANS simulations are derived from the u', l_0 and η. To estimate the Ka numbers, u' and l_0 are normalized by the laminar flame speed S_L and the laminar thermal flame thickness δ_{th}, respectively. The Ka number is then calculated as $\mathrm{Ka}=\left(u'^3/S_L^3 \cdot \delta_{th}/\ell_0\right)^{1/2}$ according to Ref. [113]. Figure 4.1 shows the scatter plot of the studied turbulent flame cases, K4, K100, K800, and K4100, in the Borghi-diagram. The corresponding conditions are located in the thin reaction zone and broken reaction zone regimes, which are commonly used in engineering combustion devices,

e.g., in gas turbines and internal combustion engines [112].

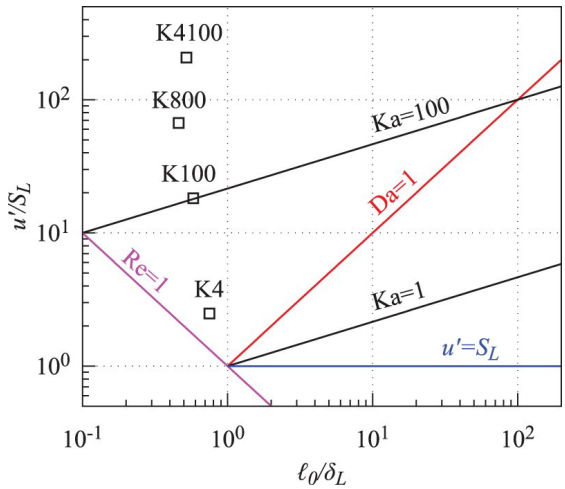

Figure 4.1: The regime diagram for the premixed turbulent flames showing the condition of the present RANS simulations. The conditions are referred to the DNS in Ref. [113].

The computational domain is a cuboid with an equal height and width of 2 mm and a length of 20 mm. According to Ref. [113], the laminar thermal flame thickness δ_{th} is 0.92 mm, which is defined by the ratio of temperature difference between the unburned (T_u) and burned (T_b) mixture to the maximum temperature gradient, i.e., $\delta_{th}=(T_b - T_u)\,/|\nabla T|_{\max}$. The turbulent flame brush is thicker than the laminar flame, thus, the mesh which can resolve the laminar flame structure could also capture the ensemble averaged turbulent flame brush. A sensitivity analysis is performed to determine the mesh size and time step. It is shown that a spacial resolution of 10 µm and a temporal resolution of 20 µs are capable to predict both the laminar and turbulent flame structure. To keep the flame in the domain for a longer time, an upstream flow ($u_{in} = S_L$) is supplied opposite to the flame propagation direction. In the following simulations, a uniform mesh size of 10 µm and a constant time step Δt of 20 µs are then adopted, which yields a Courant–Friedrichs–Lewy (CFL) number of 0.25. In all simulations, the IEM model constant, C_ϕ, is set to 2.

4.1.2 Comparison of ESF formulations

Prior to the ESF formulation comparison, the number of stochastic fields, N_{sf}, is studied using the ESF-V16 formulation. N_{sf} of 2, 8, 32, 128, and 256 are selected and performed in the case with Ka number of 100, cf. K100 in Table 4.1. Figure 4.2 shows the mean and RMS profiles of temperature, mass fractions of CH_4,

O_2 and CO_2 at 10 ms after the simulation, i.e., the initial flat flame. Figure 4.3 shows the turbulent flame speed, S_T, and the turbulent flame thickness, δ_T. The S_T and δ_T are defined as in Eq. (4.1).

$$S_T = \frac{1}{\rho_u} \int \omega_c dx, \qquad \delta_T = \frac{T_b - T_u}{|\nabla T(x)|_{\max}}, \tag{4.1}$$

where ρ_u is the density of the unburned mixture, ω_c is the reaction rate of the progress variable (H_2O in the current simulations).

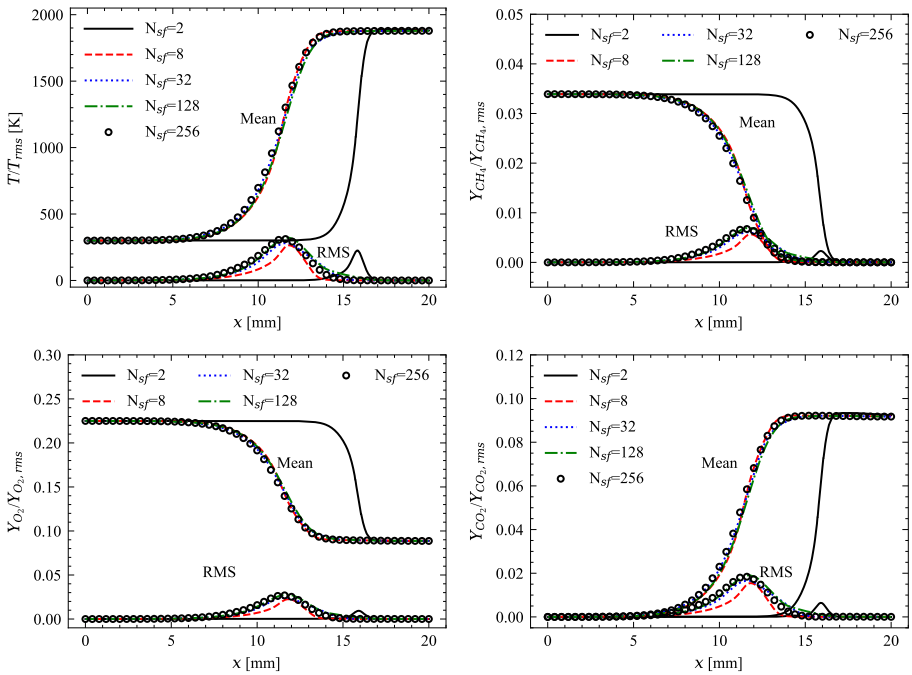

Figure 4.2: The mean and RMS profiles of temperature, mass fractions of CH_4, O_2 and CO_2 at 10 ms after the simulation using N_{sf} of 2, 8, 32, 128, and 256.

It is observed that the mean temperature and species mass fractions are well predicted with $N_{sf} = 8$, while the RMS values converge when $N_{sf} = 32$. In terms of the S_T and δ_T, N_{sf} of 128 is required in the present simulations. The N_{sf} of 128 is then used in the following simulations.

Figure 4.4 shows the stationary (at 10 ms) temperature and its RMS profile of the turbulent flames under Ka of 4, 100, 800, and 4100. Figure 4.5 shows S_T versus the inlet velocity fluctuation, u'. Figure 4.6 shows the transition of S_T and δ_T under different turbulent intensities. The physical time are normalized

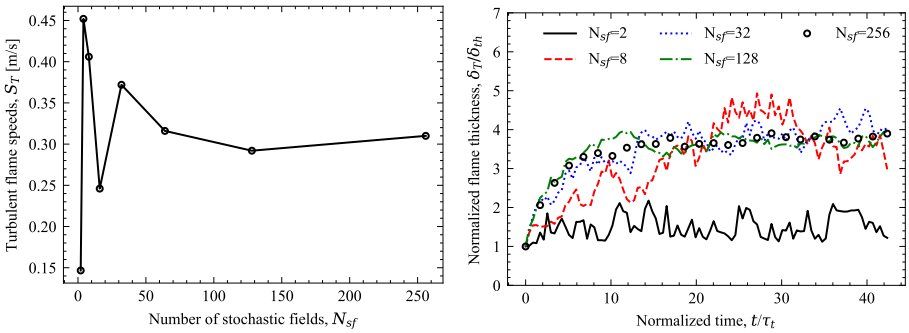

Figure 4.3: The turbulent flame speed, S_T, and flame thickness, δ_T, predicted using N_{sf} of 2, 8, 32, 128, and 256.

using the integral time scale, $\tau_t = l_0/u'$, which is 2.3, 0.236, 0.053, and 0.0192 ms for K4, K100, K800, and K4100 cases. It is found that the planar flame evolves to be thicker and faster in the turbulent environment, which is consistent with the observation in Ref. [112]. The higher the Ka number, the higher S_T and thicker δ_T in the stationary stage. The transition time, from the flat planar flame to the fully developed turbulent flame, increases with the increase of the Ka number. The turbulent flame speed, S_T, increases with the increase of u'. However, it is not linearly increased as the studied cases are not in the wrinkled and corrugated flamelets regimes. The S_T increases faster when u' is low, while it increases slowly when u' further increases.

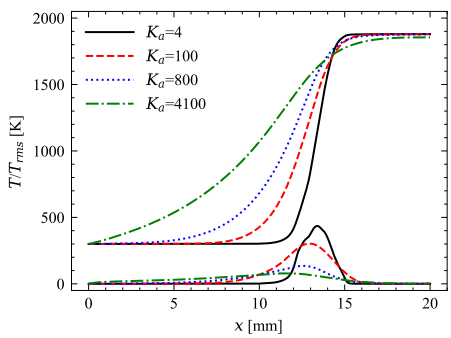

Figure 4.4: The profiles of the temperature and its RMS values at 10 ms after the initial flat flame under different turbulent intensities.

Figure 4.7 shows the temporal evolution of δ_T predicted using different ESF formulations, ESF-V98, ESF-V16, and ESF-W21. The subplots show the turbulence intensity, i.e., laminar condition and turbulent conditions with different Ka number. As suggested by Ref. [103], it is required that the ESF method is consistent in the laminar limit, i.e., the flame characteristics predicted using the ESF model should be the same as the one predicted using the WSR model

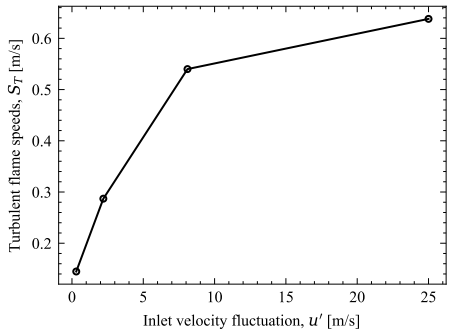

Figure 4.5: The stationary turbulent flame speed, S_T, versus the inlet velocity fluctuation, u'.

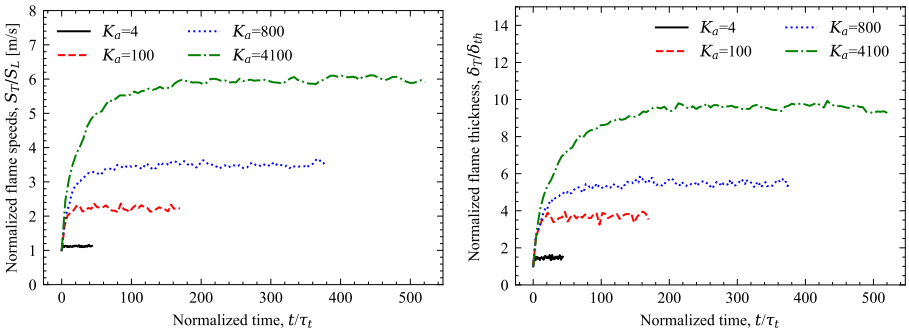

Figure 4.6: The transition of S_T and δ_T under conditions with Ka number of 4, 100, 800, and 4100.

when $u' = 0$, which is equivalent to the DNS results. However, the ESF-V98 predicts a thickened flame under the laminar condition, which is not consistent with the DNS results. The ESF-W21 formulation is consistent in the laminar limit, predicts a similar δ_T to the ESF-V98 and ESF-V16 in high Ka cases. However, the ESF-W21 formulation is not stable, resulting in a divergence in the Ka = 4 case. The ESF-V16 has shown a good agreement with WSR under the laminar condition. In the intermediate turbulence intensity cases, e.g., Ka = 4 and 100, the ESF model using the ESF-V16 formulation predicts a lower δ_T as compared with ESF-V98. Under the high Ka conditions, e.g., Ka = 800 and 4100, the ESF-V16 leads to a similar δ_T to the one predicted by ESF-V98. This is because that the turbulent viscosity is much larger than the laminar viscosity. The difference of the Wiener term in ESF-V98 and ESF-V16 is negligible.

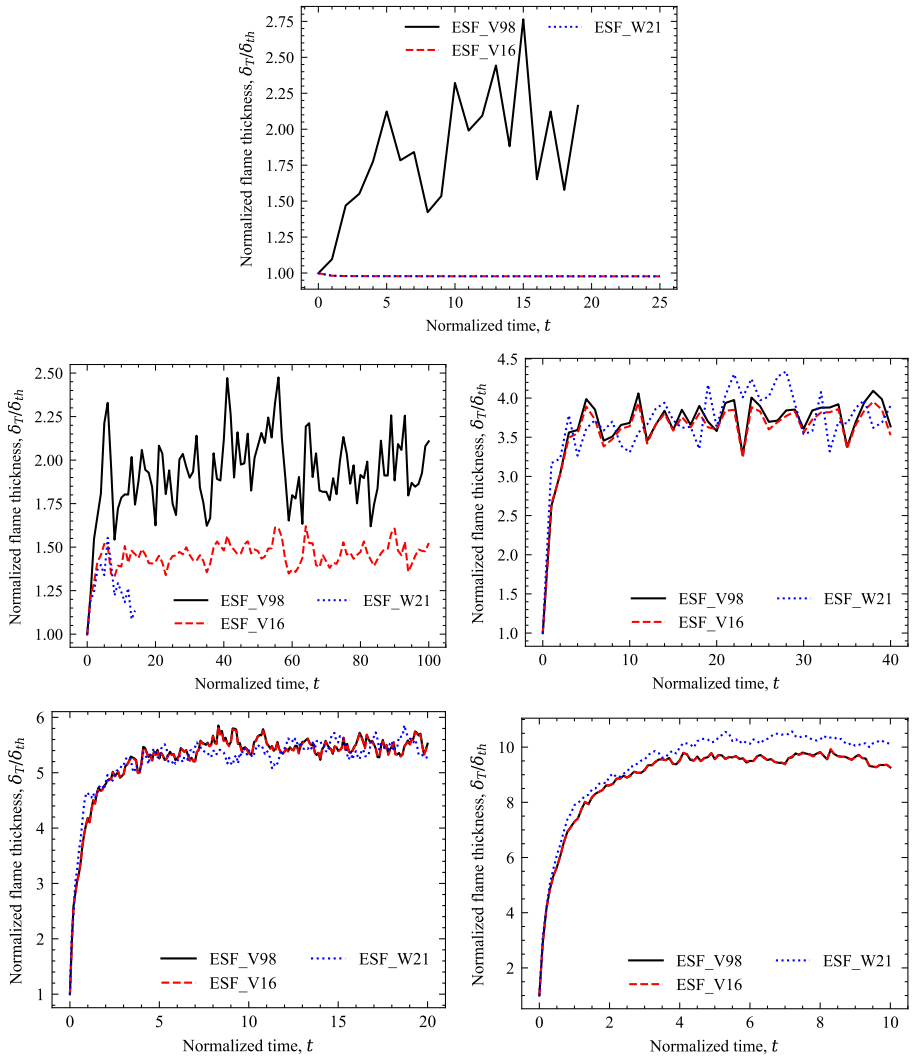

Figure 4.7: The temporal evolution of the turbulent flame thickness, δ_T, predicted using the ESF methods with formulations of ESF-V98, ESF-V16, and ESF-W21.

4.2 Non-premixed flame

In this section, turbulent methane/air counterflow diffusion flames are studied using the ESF method. The flame configuration is based on the experiments of Mastorakos [115], where the inlet turbulence was generated using perforated plates. Both transient and statistically stationary mean flames under different strain rates are simulated using the ESF method and RANS turbulence closure.

The goal is to investigate the performance of ESF-O and ESF-C in terms of the element mass conservation and the prediction of flame quenching as the strain rate increases.

4.2.1 Case specification

According to the experiments of Mastorakos [115], methane and air are supplied from opposed turbulent jets. A diffusion flame is established in the mixing region of opposed jets. The fuel and air streams have equal momentum flow rates, i.e., $\rho_a U_a^2 = \rho_f U_f^2$, where ρ denotes the inlet gas density while U represents the stream bulk velocity. The subscripts a and f are the air and fuel, respectively. Following Refs. [115–117], the intensity of mixing of the opposed jets is characterised using the global strain rate, a_g, taken as the sum of the mean flow strain rate, a_m, and turbulent strain rate, a_t, defined as,

$$a_g = a_m + a_t, a_m = 2U_0/H, a_t = u'^{3/2}/\sqrt{\nu l_0}, \tag{4.2}$$

where, U_0 is the bulk velocity of the air stream used for normalization, i.e. $U_0 \equiv U_a$. H is the separation distance between the two jets. ν is the kinematic viscosity. u' and l_0 are the turbulent RMS velocity fluctuation and integral length scale of the inflow streams, respectively.

The computational domain is a cuboid with a length (x-axis) of 20 mm, width (y-axis) and height (z-axis) of 4 mm. A uniform mesh size of 20 μm is adopted to resolve the diffusion flame structure. The gaseous methane is supplied with a speed of U_f and temperature of T_f at $x = 0$ mm. The air is supplied with a velocity U_a and temperature T_a at $x = 20$ mm. As the mean flame is axisymmetric, the turbulent flow is governed by two-dimensional RANS equations. The k-ϵ model is employed using the standard model constants, C_μ=0.09, C_1=1.44 and C_2=1.92. The inlet turbulent kinetic energy, k, for the fuel and air streams are set at $k_f = \frac{3}{2}(IU_f)^2$ and $k_a = \frac{3}{2}(IU_a)^2$, respectively. I is the turbulent intensity, which is 0.085, obtained in the experiments [115]. The boundary conditions of the turbulence kinetic energy dissipation rate ϵ are derived from the turbulence kinetic energy k and turbulence integral length l_0, i.e. $\epsilon = C_\mu^{\frac{3}{4}} k^{\frac{3}{2}}/l_0$. The IEM model constant, C_ϕ, is set to 2.

The time step of the temporal integration for the flow simulation is kept a constant value of 1 μs, which is shown to ensure numerical stability and also yields a small increment for the Wiener term. A second-order backward Euler scheme is utilised for the temporal integration, and the second-order filtered-linear scheme is employed for the spatial discretisation. An ordinary differential

Table 4.2: The key parameters of the studied counterflow diffusion flames.

Parameters	Values
Bulk strain rate (a_g)	200 – 450 s^{-1}
Inlet fuel bulk velocity U_f	1 – 2 m/s
Inlet air bulk velocity $U_a = U_0$	1.34 – 2.68 m/s
Inlet turbulent intensity (u'/U_0)	0.085
Turbulence integral length (l_0)	4 mm
Separation distance (H)	20 mm
Fuel temperature (T_f)	293 K
Air temperature (T_a)	293 K
Fuel composition, mass fraction	$Y_{CH_4} = 1$
Air composition, mass fraction	$Y_{O_2} = 0.23$, Y_{N_2}=0.77
Stoichiometric mixture fraction (Z_{st})	0.055

equation solver, Seulex, is employed for the integration of the chemical reaction rates. An adjustable chemical time step is used with an initial time step of 0.1 ns. The chemical reactions are modelled using finite-rate chemistry with a skeletal mechanism developed by Smooke [118], consisting of 16 species and 35 elementary reactions. The Smooke's mechanism is capable of predicting a methane/air laminar diffusion flame quenching at a scalar dissipation rate of χ_q = 35 s^{-1} under atmospheric temperature and pressure [119], which has shown a good trade-off between computational efficiency and model accuracy in terms of the prediction of the flame extinction.

The number of stochastic fields is examined using the ESF-O and ESF-C method with N_{sf} = 8, 32, 128, 256 and 512. Both transient and statistically stationary flame simulations are conducted for each N_{sf}. A diffusion time scale of a laminar flamelet, $t_d \sim Z_{st}/\chi_q$ [120], is introduced to quantify the transient flame behaviour during flame extinction. t_d is the characteristic time of flamelet quenching at high strain rate [119, 120]. In the present flame condition, $t_d \sim 0.055^2/35 = 0.086$ ms. In the transient flame simulations, a_g is varied from 200 s^{-1} to 450 s^{-1} during a time period of 10 t_d, ranging from stationary flame mode to flame extinction. The strain rate is varied by adjusting the flow velocity of the fuel and air streams while maintaining equal momentum of the two jets. In the stationary simulations, 10 cases are considered around the extinction strain rate. The conditions of the flames are summarized in Table 4.2, which are selected based on the experiments [115]. For a more detailed description of the experimental setups, the readers are referred to Refs. [115, 121, 122].

4.2.2 Element mass conservation

The element mass conservation results from the original ESF method and the modified ESF method are examined first. In order to do so, a transport equation for the mixture fraction is solved to obtain the theoretical value of element mass fractions. Since the Lewis number is assumed to be unity in the ESF simulations, the element mass fraction from the ESF results should be identical to the theoretical values from the mixture fraction.

Since the elements C and H are originally from fuel (CH_4), while O and N from air (O_2, N_2), cf. Table 4.2, the theoretical distribution of the element mass fraction of C, H, O and N are obtained from the spatial distribution of the transported mixture fraction (Z),

$$Y_{C,t} = \frac{\gamma}{1+\gamma} Z, Y_{H,t} = \frac{1}{1+\gamma} Z, Y_{O,t} = \frac{1}{1+\eta}(1-Z), Y_{N,t} = \frac{\eta}{1+\eta}(1-Z). \quad (4.3)$$

Here, Y_J is the mass fraction of element J, where J represents respectively element C, H, O, and N. Subscript t denotes the element mass fraction calculated from the transported Z. γ and η are constants, $\gamma = 2.979$ and $\eta = 3.3478$, representing the mass ratio of element C to H in the fuel and the mass ratio of element N to O in the air, respectively.

Figure 4.8 shows the relative error of the element mass fraction between the theoretical one ($Y_{J,t}$) and the local value predicted from the ESF simulations (Y_J) at different axial locations, where $\Delta Y_J = (Y_J - Y_{J,t})/Y_{J,max}$. The results are obtained under a global strain rate of 200 s^{-1}, under which the flame is stationary and far from quenching. A non-zero ΔY indicates a violation of element mass conservation in the ESF simulations. For the ESF-O method, the element mass conservation is highly dependent on the number of stochastic fields, N_{sf}. ΔY decreases as N_{sf} increases. With 8 stochastic fields ($N_{sf} = 8$), the value of ΔY_J is rather significant. The largest ΔY_J is found in the spatial location $x = 3 - 12$ mm, where fuel/air mixing takes place, along with chemical reactions around the stoichiometric mixture fraction (at $x \sim 8$ mm), creating a significant gradient of the species mass fraction and enthalpy, thus a higher value of the Wiener term. The behaviour of ΔY_C and ΔY_H is opposite to that of ΔY_O and ΔY_N. The element mass fractions of N and O are compensated as the species mass fractions are normalized to ensure the sum of the mass fractions equal to unity. In contrast, the element mass conservation law is satisfied in the ESF-C simulations, independent of N_{sf}. The results of ESF-C with 8 stochastic fields satisfy exactly the element mass conservation law, while the results from ESF-O with 512 stochastic fields still show a violation of the element mass conservation law.

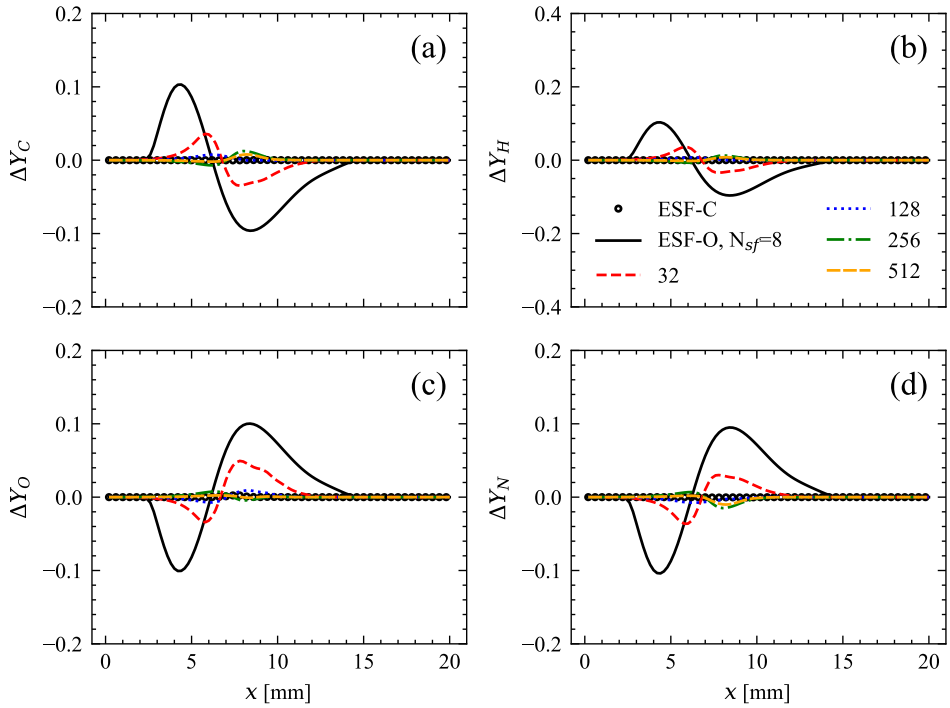

Figure 4.8: Error in the element mass fractions of (a) C, (b) H, (c) O, and (d) N at different axial locations under a global strain rate of 200 s^{-1}. $\Delta Y_J = (Y_J - Y_{J,t})/Y_{J,max}$, where Y_J is the local mass fraction of element J = (C, H, O, N); $Y_{J,t}$ is the mass fraction of J calculated from the transported mixture fraction, Z; $Y_{J,max}$ is the maximum mass fraction of J in the domain. The lines represent the ESF-O method with different numbers of stochastic fields, N_{sf} = 8, 32, 128, 256, and 512. The symbols denote the results from the ESF-C method with N_{sf} = 8.

4.2.3 Stationary flames at different strain rates

Figure 4.9 shows the maximum mean flame temperature, T_{max}, and maximum mean OH mass fraction, $Y_{OH,max}$, for the stationary flames at different global strain rates. In each stationary flame simulation the global strain rate is kept constant. At low strain rate, the maximum flame temperature and OH mass fraction are relatively high. As the strain rate increases, the mixing rate of the reactants increases while the chemical reaction rate decreases, as indicated by the decreasing maximum mean OH mass fraction. At a sufficiently high strain rate, close to the quenching strain rate, the flame temperature decreases as the consumption of the reactants are slower than their supply to the reaction zone. Once the strain rate reaches its critical value at extinction (extinction strain rate), T_{max} and $Y_{OH,max}$ decrease drastically and the flame is not able to sustain itself.

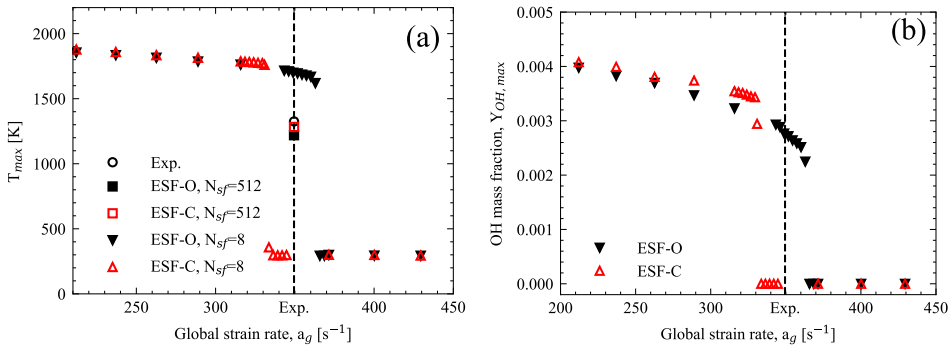

Figure 4.9: Maximum mean flame temperature (a) and maximum mean OH mass fraction (b), for stationary flames at different global strain rates, a_g. The vertical dash line represents the measured extinction strain rate ($a_g = 350$ s^{-1}) [115].

The results from ESF-O and ESF-C are rather similar at low strain rate conditions. However, under conditions close to quenching the two methods predicted significantly different results. In the experiments it was found that the maximum mean flame temperature at $a_g = 350$ s^{-1} is about 1300 K [115]. Slightly above this strain rate the flame was quenched. This condition is indicated in Fig. 4.9 as the experimental extinction condition. The results at this strain rate are found to be highly sensitive to the ESF methods and N_{sf}.

Figure 4.10a shows a comparison of the mean flame temperature as a function of mixture fraction, predicted using ESF-O and ESF-C methods with N_{sf} of 8 and 512. The maximum mean flame temperature has been shown in Fig. 4.9a. The ESF-O with 8 stochastic fields predicted a stationary flame state whereas ESF-C predicted a quenched state. When the number of ESF was increased to 512, both ESF-O and ESF-C yielded rather similar results. The predicted results are also in close agreement with the experiments.

The flame was shown to be highly non-stationary at $a_g = 350$ s^{-1} [115]. Statistical analysis of the experimental data showed a high probability of quenched state and a certain low probability of burning states, cf. Fig. 4.10b. Both the ESF-O and ESF-C methods with $N_{sf} = 512$ captured very well the PDF distribution of flame temperature, while both methods could not capture very well the PDF distribution with $N_{sf} = 8$.

4.2.4 Transient flames at different strain rates

As the flame extinction is a transient process, ESF simulations with a transient variation of strain rate were carried out. In the transient flame simulations, a_g

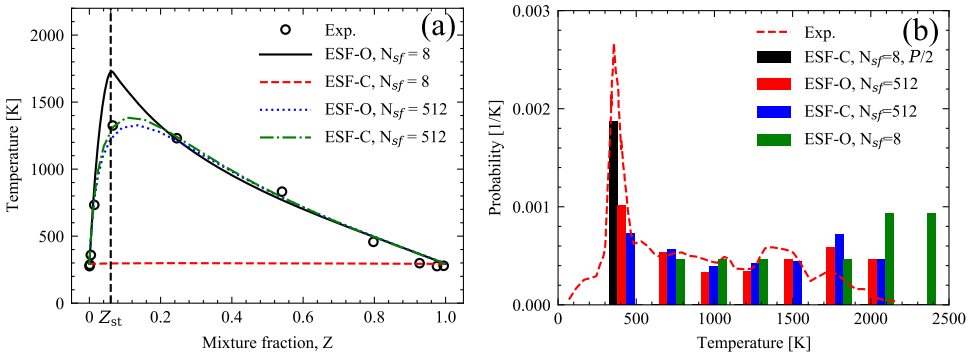

Figure 4.10: (a) Mean temperature as a function of mixture fraction, predicted using different N_{sf} under global strain rate of 350 s^{-1}, and (b) PDF of temperature at the stoichiometric mixture fraction under the same strain rate condition as in (a). The PDF predicted from ESF-C with N_{sf}=8 is scaled (reduced) by a factor of 2, to fit the range of vertical axis in (b). The experimental results are from the work of Mastorakos [115].

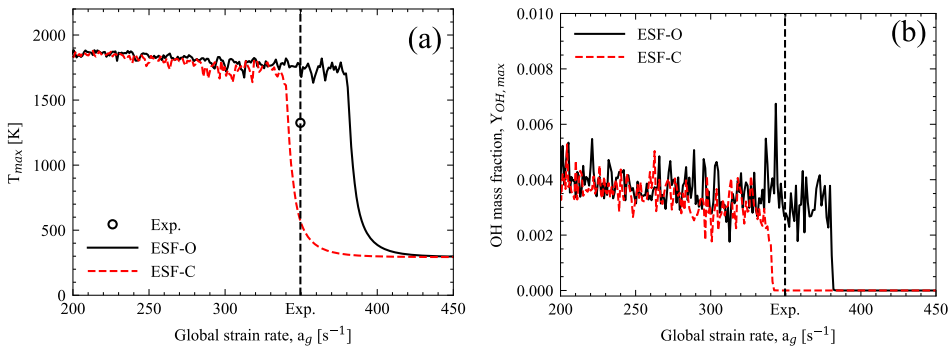

Figure 4.11: Maximum flame temperature (a) and maximum OH mass fraction (b), for transient flames at different global strain rates, a_g. In both ESF-O and ESF-C methods $N_{sf} = 8$. The vertical dash line represents the measured extinction strain rate ($a_g = 350$ s^{-1}) [115].

was varied from 200 s^{-1} to 450 s^{-1} during a time period of 10 t_d, ranging from stationary flame mode to flame extinction. As shown in Fig. 4.11, the maximum flame temperature and OH mass fraction show similar trends as those of stationary flames at different strain rates. In the transient flames the maximum OH mass fraction oscillates as the strain rate (and time) increases, whereas it is rather smooth in the stationary flames. With $N_{sf} = 8$, the extinction strain rate from ESF-C is in closer agreement with the experiments than that from ESF-O.

In both the stationary and transient flame simulations, ESF-C predicted a lower extinction strain rate than ESF-O. From the distributions of the fuel and oxygen mass fractions in the mixture fraction coordinate, it is found that flame extinction occurs when the oxygen starts to leak through the reaction zone to the

fuel-rich side of the flame, consistent with the laminar flame extinction theory [123]. It has been known that premixing of fuel to the oxidizer side of the flame strengthens the flame giving rise to a higher extinction strain rate [124]. In the ESF-O method, the loss of C and H elements in the reaction zone (Fig. 4.8) could increase the diffusion of fuel to the reaction zone towards the oxidizer side of the flame. This may be the reason behind the higher extinction strain rate predicted by the ESF-O method.

4.3 Spray flame in constant volume chamber

In the following studies, the focuses are on the spray flames under the CI engine conditions. The computational configuration is based on the Spray-H and spray-A experiments from the Engine Combustion Network (ECN), which is an international collaboration among experimental and computational researchers in engine combustion. ECN established a database of well-documented experiments that are appropriate for model validation and the advancement of scientific understanding of combustion at conditions specific to engines [38]. Table 4.3 shows the operating conditions of two well-known ECN spray experiments, i.e., Spray-H and Spray-A, which involve an injection of liquid fuel (n-heptane in Spray-H and n-dodecane in Spray-A) into a high-temperature and high-pressure cubical constant-volume vessel (CVV) to mimic the spray of engines. As it is injected from a high-pressure common rail injector, the liquid jet undergoes break-up, evaporation, mixing, ignition and eventually evolves to a stabilized spray flame. The ambient mixture has oxygen concentrations of 21%, 15% and 0% representing the reacting spray under in-cylinder conditions without and with exhaust gas recirculation (EGR), and non-reacting spray conditions. With advanced diagnostics involved, the measured liquid and vapour penetration length (LPL and VPL), the spatial distribution of the mixture fraction are available for the non-reacting spray. For the reacting spray, IDT, pressure rise profile, flame lift-off length (LOL) and soot volume fractions are accessible in ECN [38]. It is worth noting that only single-fuel spray flame experiment is available. The capabilities of the mesh and models are first examined based on these measurements. Upon the model validation using the single-fuel non-reacting and reacting case, dual-fuel combustion simulations and numerical analysis are performed. Such workflow is similar to those in Refs. [49, 50, 63].

In this section, single-fuel spray simulations are performed using WSR, PaSR and ESF combustion models. Those simulations are based on the n-dodecane fueled Spray-A experiments. In the next Chapter, both single- and dual-fuel spray simulations based on the Spray-H are discussed. The Spray-H is selec-

Table 4.3: ECN Spray-H and Spray-A operating conditions [38].

Parameter	Spray-H	Spray-A
Fuel	n-heptane	n-dodecane
Nozzle diameter [μm]	100	90
Fuel temperature [K]	373	363
Injection pressure [MPa]	150	150
Injection duration [ms]	6.8	1.5
Injection mass [mg]	17.8	3.46
Ambient O_2 concentration [vol.]	21%	15%
Ambient temperature [K]	900, 950, 1000	900
Ambient pressure [MPa] [a]	3.76, 3.97, 4.18	5.83

[a] The ambient pressures are changed with the ambient temperatures and compositions to maintain a density of 14.8 kg/m^3 for Spray-H and 22.8 kg/m^3 for Spray-A.

ted as the baseline case of the dual-fuel combustion. Because the compact mechanism with high precision on the n-dodecane and methanol ignition predictions is not available yet in the thesis research topic selection stage, while a skeletal mechanism for n-heptane/methanol dual-fuel combustion is accessible and shows a good trade-off between computational efficiency and model accuracy. Recently, a skeletal mechanism, consisting of 65 species and 363 reactions (henceforth denoted as Lapointe-65), was proposed [125]. Lapointe-65 is composed of a fuel-dependent sub mechanism and a detailed fuel-independent C_0-C_4 chemistry sub mechanism (Aramco Mech 2.0) [126] using a hybrid approach. A further study is then carried out based on the Lapointe-65 and presented in this section.

4.3.1 Simulation configuration

The baseline condition of the ECN Spray-A is considered in the current LESs. Correspondingly, one non-reacting LES case (AN) and 6 reacting LES cases (AR) with WSR, PaSR and ESF are studied, cf. Table 4.4. Table 4.5 shows the ambient gas temperature, pressure and compositions for AN and AR. The non-reacting case is used for the LPT and SGS models validation. The combustion model comparison is performed under the reacting condition, which is is a low-temperature combustion condition with moderate EGR [127]. The computational configurations, and validations of the non-reacting case are described in Paper V.

To shed light on the TCI, the aforementioned WSR, PaSR and ESF based transport PDF models are employed in the LES of the single-fuel flame under the Spray-A conditions. All of the combustion models are based on the finite-

Table 4.4: The LES case setups. The first case is a non-reacting case, denoted as AN for brevity. Case AR1 to AR6 are reacting cases named by its chemical mechanism and combustion model: Y-WSR for reacting case with Yao-54 and WSR model. All the reacting cases are under the same conditions as experiments.

Case	Name	Chemical mechanisms	Combustion model
AN	-	-	-
AR1	Y-WSR	Yao-54	WSR
AR2	Y-PaSR	Yao-54	PaSR
AR3	Y-ESF	Yao-54	ESF
AR4	L-WSR	Lapointe-65	WSR
AR5	L-PaSR	Lapointe-65	PaSR
AR6	L-ESF	Lapointe-65	ESF

Table 4.5: Initial conditions of the ambient mixture in the n-dodecane fueled spray cases.

Cases	Temperature [K]	Density [kg/m^3]	Pressure [MPa]	Ambient mixture composition [vol.]			
				O_2	N_2	CO_2	H_2O
AN	900	22.8	5.95	0%	89.71%	6.52%	3.77%
AR	900	22.8	5.83	15.00%	75.15%	6.22%	3.62%

rate chemistry, which is highly desirable as it can provide information about the local chemical composition and predict ignition and extinction that are important in the lifted spray flames under engine conditions. To reduce the computational time, the chemistry speedup approach, the CCM algorithm, is used.

The choice of the chemical mechanisms has a strong influence on the spray flame IDT and LOL [128]. To avoid being blinded by the chemical mechanisms, all the combustion models are coupled with two different n-dodecane chemical mechanisms: a skeletal mechanism with 54 species and 269 reactions proposed by Yao *et al.* [129] (henceforth named as Yao-54 for brevity) and the hybrid mechanism Lapointe-65 [125]. Yao-54 has been validated against experimental data for shock tubes, perfectly stirred reactors, flow reactors, and laminar flame speeds [129]. It has also been widely used in the Spray A context [49, 50, 61, 78, 128–130]. Lapointe-65 is a hybrid mechanism enabling a good ignition prediction over a large condition range [38, 131]. Both mechanisms have low- and high-temperature chemical pathways and can capture the low-temperature heat release and NTC behaviour [125, 129], which is important for the n-dodecane/air ignition under engine conditions.

4.3.2 Model comparison

4.3.2.1 Computational costs

Figure 4.12 shows the overall CPU hours in the six reacting cases. The LES is carried out with 192 processors in parallel. The CPU hours account from 0 ms to 0.8 ms after the start of injection (ASI). It is observed that the CPU hours in the non-reacting LES is an order of magnitude lower than the reacting LES. In the reacting cases, the computational cost in the cases with the Yao-54 mechanism is lighter than the cases using the Laponite-65 mechanism. The CPU hours consumed in the PaSR cases are slightly larger than that in WSR, while it counts for only 20% of that in the ESF cases. The computational cost includes the continuity equation, momentum equations, species and energy transportation in the non-reacting LES. In the reacting LES, the integration of the chemical kinetics ODEs is also taken into account. Figure 4.13a shows the proportion of the CPU times consumed in the chemistry integration. It is seen that more than 70 % of computational costs are consumed in the chemistry integration from 0.5 to 1.5 ms ASI.

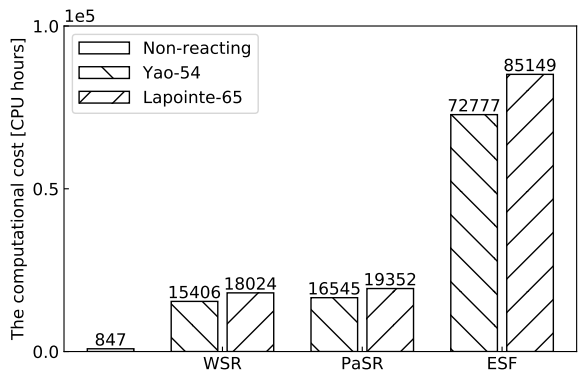

Figure 4.12: The computational costs in CPU hours for the non-reacting, and reacting cases with WSR, PaSR and ESF models. The accumulated CPU hours is counted for all processors from the start of injection to 0.8 ms ASI.

In the CCM algorithm, the reactive scalars (species mass fractions and enthalpy) are mapped from the spatial space to a reduced-dimensional composition space. The number of reactive scalars pairs in the spatial space is denoted as $N_{spatial}$, which equals to the computational cells number (N_{cell}) in WSR and PaSR cases and counted as $N_{cell} \times N_{sf}$ in ESF cases. The reactive scalars pairs in the reduced-dimensional composition space are referred to as activate cells. The number of activated cells is denoted as $N_{activate}$. The ratio of $N_{activate}$ to $N_{spatial}$ is known as the chemistry speedup factors, α_c. Figure 4.13b shows the temporal

evolution of α_c in the reacting cases L-WSR and L-ESF. The α_c in the cases using the Yao-54 mechanism has the same trend as in cases using Lapointe-65. The α_c profile in the PaSR case shows a similar value as that in the WSR case. For brevity, the temporal evolution of α_c in PaSR cases and cases with the Yao-54 mechanism is not shown in Fig. 4.13b. Before the start of injection, the computational domain is assumed to be homogeneous, i.e., $\alpha_c = N_{cell}$. It is observed that α_c dramatically decreases in the beginning. The speedup factor keeps steady and decreases slowly after 0.6 ms ASI, where the flame is stabilized. α_c remains a value of 20 in the WSR case and 30 in the ESF case. It means that the CCM algorithm coupled with the ESF method has a higher chemistry speedup effect than the one with WSR under the same configuration. This is also the reason why the CPU hours in the ESF cases is less than N_{sf} times the WSR cases. The injection ends at 1.5 ms ASI. After the end of injection, α_c increases until the end of the simulation, i.e., 2 ms ASI.

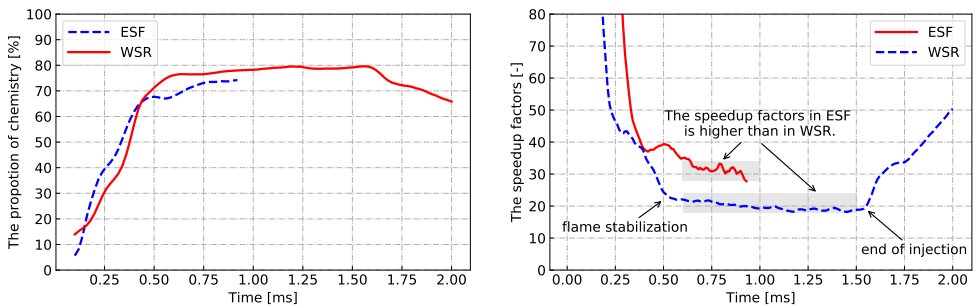

Figure 4.13: Temporal evolution of a) the proportion of the CPU times consumed in the chemistry integration, and b) the chemistry speedup factors, α_c, in the reacting cases L-WSR and L-ESF. α_c is defined as the ratio of number of activate cells to the total number of computational cells.

4.3.2.2 Flame initialization

Figure 4.15a shows the temporal evolution of the pressure difference between the chamber pressure and its initial value, i.e., the pressure rise Δp. The experimental data are obtained from the ECN measurements [38]. Figure 4.15b shows the heat release rate (HRR) profile measured in the experiments [38] and predicted in the reacting cases. The measurements are apparent HRR, which is derived from the pressure rise profile accounting for heat release from chemical reactions and heat absorption from fuel evaporation (as it is a CVV, there is no volume change and external mechanical work). The numerical results are the net HRR, only the chemical heat release is taken into account. It is found that the onset of the pressure rise is earlier in ESF, followed by the ones predicted by

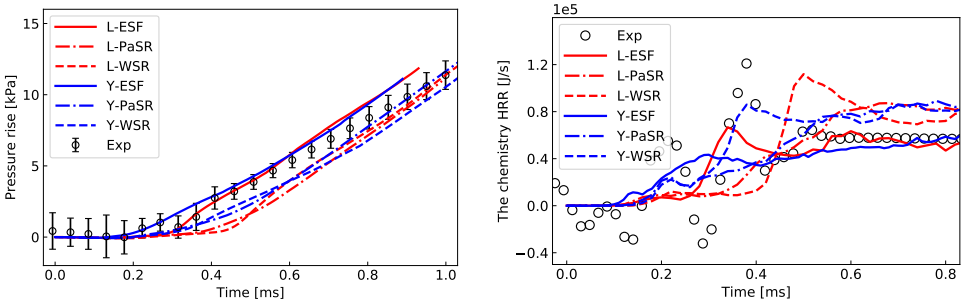

Figure 4.14: a) The pressure rise predicted in the reacting cases and the corresponding results measured in experiments [38]. b) temporal evolution of the experimental and simulated heat release rate (HRR). The experimental HRR is calculated from the time derivative of pressure. The simulated HRRs are the volumetric integral chemistry HRR.

WSR and PaSR. Two-stage heat releases are observed in the HRR profiles. The first heat release is found around 0.2 ms ASI, which is known as the first-stage or low-temperature heat release. The HRR during the first-stage heat release is less than 0.4 J/s in Fig. 4.15b. The onset of the second heat release is observed between 0.2 to 0.6 ms ASI. This heat release is referred to as the second-stage or high-temperature heat release. The second-stage HRR is higher than the value in the first stage. It is worth mentioning that ESF, e.g., L-ESF and Y-ESF, predicts an equal second-stage HRR as compared with experiments after 0.6 ms ASI. However, during the same period, the HRR predicted by WSR and PaSR are higher than the measurements regardless of the chemical mechanisms. The transition time from the first- to the second-stage ignition varies in different combustion models. The WSR model predicts the longest transition time, which is evident by a plateau between 0.2 to 0.4 ms in the HRR profiles of L-WSR and Y-WSR. The counterparts in ESF are much shorter. The transition predicted in PaSR is not clear as HRR increases slowly from the onset of the first-stage to the second-stage heat release. In addition, a heat release spike is found in L-WSR, Y-WSR, L-ESF, and Y-ESF (the peak value is lower than the others) around 0.4 ms ASI, which is consistent with the experiments.

The low- and high-temperature heat releases correspond to the low- and high-temperature chemistry. The onset of the two-stage heat release indicates the two-stage ignitions. Figure 4.15 shows the two-stage IDTs predicted in WSR, PaSR and ESF with Lapointe-65 and Yao-54 mechanisms. The measurement of the second-stage IDT is also shown, which is 0.44 ms defined based on a pressure rise of 3 kPa [38]. The same definition is used for the second-stage IDT in LES. The first-stage IDT in LES is defined by the time interval from the start of injection to the first peak of the time derivative of temperature. The results

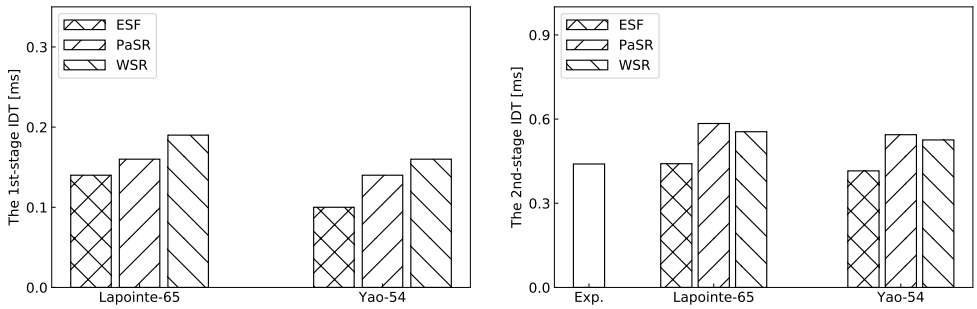

Figure 4.15: The predicted two-stage ignition delay time in WSR, PaSR and ESF with Lapointe-65 and Yao-54 mechanisms, and the measured second-stage ignition delay time.

show that, regardless of the chemical mechanisms, ESF predicts the shortest first-stage IDTs while WSR predicts the longest values. The second-stage IDTs in the ESF cases, i.e., L-ESF and Y-ESF, are close to the measurement. In contrast, WSR and PaSR have longer second-stage IDTs. In summary, the two-stage ignitions and heat releases are well predicted using the ESF method, which yields shorter low- and high-temperature IDTs as compared with WSR and PaSR.

4.3.2.3 Flame stabilisation

In simulations of Spray-A, both stabilised high temperature flame and cool flame are observed.

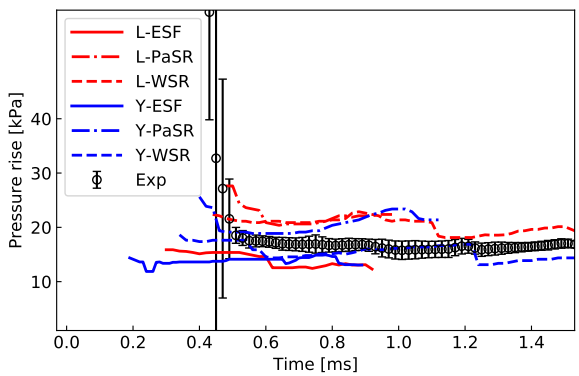

Figure 4.16: The evolution of the spray flame lift-off length (LOL), predicted by different combustion models and measures in experiments [38].

Figure 4.16 shows LOL of the spray flame. In LES, the LOL in LES is defined as

the distance from the injector to the nearest axial location of Favre-average OH mass fraction reaching 2% of its maximum in the domain after a stable flame is established. OH is an important product in high-temperature chemistry, which is observed after the second-stage ignition. Thus, the LOL indicates the stabilization of the high-temperature flame. It is found that LOL in experiment and LESs fluctuate within a range of 15-25 mm. The LOL in ESF cases is the shortest, followed by WSR and PaSR.

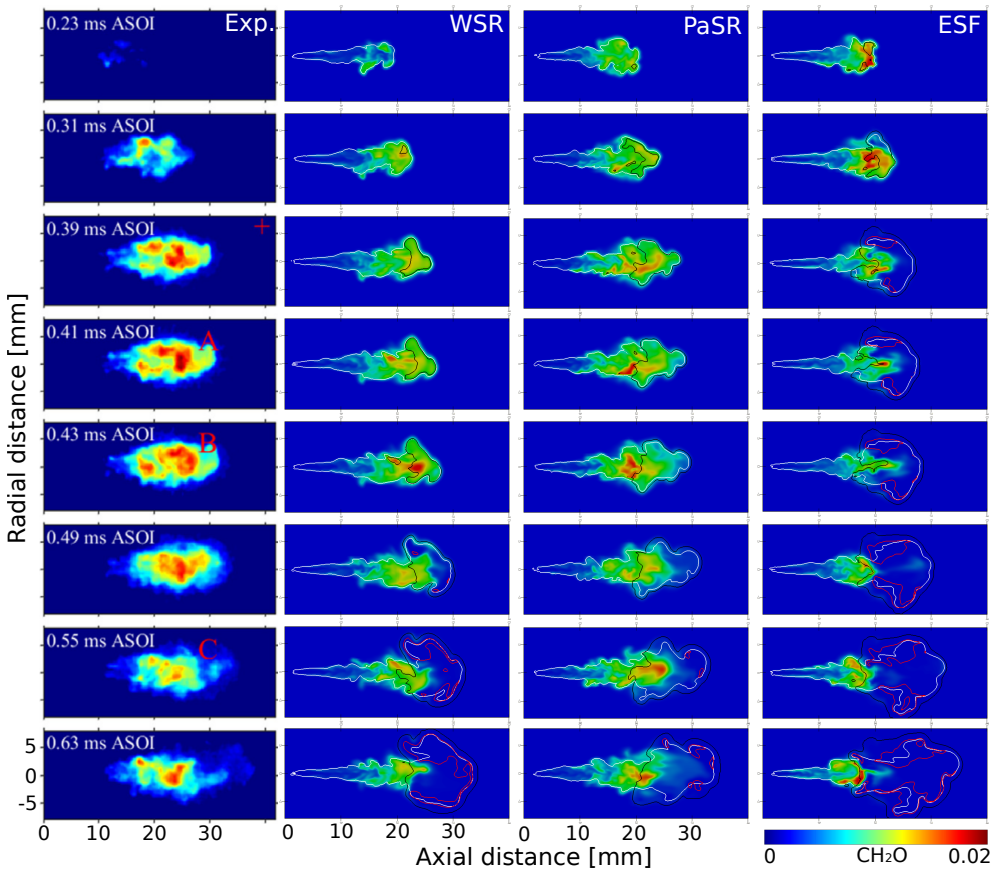

Figure 4.17: Temporal evolution of the cool flames, indicated by CH_2O. The rows represent the time series from 0.23 ms to 0.63 ms after the start of injection. The columns denote the snapshots of the spray central plane from the experiments (denoted as Exp.) [132], and the LES results using WSR, PaSR, and ESF models. The colour in the experimental results represents the PLIF signal intensity. The colour in the simulations represents CH_2O mass fractions. The white line represents the stoichiometric mixture line. The black and red lines are temperature iso-lines of 1000 and 2000 K, respectively.

Figure 4.17 shows the sequential distribution of CH_2O, which is an indicator of the cool flame in n-dodecane combustion, from the CH_2O planar laser-induced fluorescence (PLIF) measurements and the LES results using Lapointe-65 mechanism. The selected time series highlights the occurrences of first-stage ignition

(0.23 ms), CH_2O propagation (from 0.31 to 0.41 ms), second stage ignition (0.43 ms), consumption of CH_2O (from 0.49 to 0.55 ms), and the stabilization of CH_2O (0.63 ms). In experiments, the formation of CH_2O is first observed at 0.21 ms (not shown in Fig.4.17 as the experimental data is not available [132]). In LESs, at 0.23 ms, CH_2O are found in the fuel-rich region accompanied by a small temperature rise region in PaSR and a slightly larger region in ESF, denoted by a black iso-line of 1000 K temperature. At 0.31 ms, higher signal intensity is detected in the spray region. CH_2O propagates upstream and downstream in the following frame at 0.39 ms. Similar behaviour is observed in simulations, at the same time, the CH_2O in two sides near the tip of the spray are consumed in the ESF result. At 0.41 ms and 0.43 ms, the high-temperature chemistry initiates at the tip of the jet (indicated by "A" in Exp.), accompanied by consumption of CH_2O (indicated by "B" in Exp.) [132]. The consumption of CH_2O comes later time at 0.49 ms in WSR and PaSR results. By 0.63 ms, a large portion of the CH_2O in the spray region are consumed. In the measurements, the cool flame is stabilized in the fuel-rich region between 10 mm to 30 mm downstream, which is well captured in PaSR results. In comparison, WSR and ESF predict a cool flame stabilization region in 10 mm and 25 mm downstream the injector.

4.4 Concluding remarks

In the premixed flame simulations, ESF-V16 has shown a good numerical stability in both laminar and turbulent conditions. In the methane/air non-premixed flame, the newly developed solution procedure, ESF-C method, shows a good performance on the prediction of flame extinction and satisfy the element mass conservation law. In the spray combustion simulations, the ESF method shows a good agreement with experiments in terms of IDT, pressure rise, and flame lift-off. Therefore, the ESF method is employed in Paper I to study the ignition of the n-heptane/methanol dual-fuel combustion.

However, the ESF computational cost is an order of magnitude higher than of WSR and PaSR. In Paper II and Paper III, the NOx and soot are discussed, which requires a relatively long simulation time. It is not affordable to run all the simulations with ESF in these parametric studies. Therefore, PaSR is adopted, which also shows a fairly good results on the prediction of the flame structures. To capture the IDT and LOL in PaSR, the chemical mechanism used is slightly different from that in Paper I. More details are referred to Paper II and Paper III.

Chapter 5

Study of dual-fuel combustion

In this chapter, the n-heptane/methanol dual-fuel combustion is studied. The numerical simulations are carried out based on the ECN Spray-H conditions.

5.1 Computational configurations and case setup

In the dual-fuel spray combustion, the liquid fuel is injected into the pressurized preheated ambient gas. The liquid n-heptane is used to mimic the pilot diesel fuel in the dual-fuel premixed engines. The ambient gas is parameterized using gas density, temperature and equivalence ratios (ϕ_m), which is defined as the ratio of the actual methanol-"air" ratio to the stoichiometric methanol-"air" ratio. It is worth mentioning that the "air" is not the atmosphere air but refers to the combustion chamber "air" composition, which resembles that of the ECN experiment to mimic the in-cylinder mixture of engines. In Spray-H, the "air" density is set to 14.8 kg/m^3, while molar concentrations of O_2, N_2, CO_2 and H_2O are set to 21%, 69.33%, 6.11% and 3.56%, respectively [38]. The gaseous methanol is mixed with "air" to form a homogeneous and quiescent primary fuel-air mixture before the n-heptane injection, following the previous LES works [49–51, 133, 134]. According to the ideal gas equation of state, the pressure is calculated from the gas density, ambient temperature, and the mixture average molar mass. Details of the ambient mixture initial conditions can be found in Table 5.1.

Table 5.2 shows the LES cases in this study. In the case names, 'H' denotes that it is based on the Spray-H experiments ('A' represents the Spray-A); 'N' and 'R' denotes the non-reacting and reacting cases, respectively. Cases HN

Table 5.1: Initial conditions of the ambient mixture in the n-heptane fueled spray LES cases.

Cases	ϕ_m	Density [kg/m^3]	Ambient methanol/air mass fraction composition				
			CH_3OH	O_2	N_2	CO_2	H_2O
HN	0	14.8	0	0	0.8763	0.1001	0.0237
	0	14.8	0	0.2280	0.6590	0.0913	0.0218
HR[a]	0.1	14.8	0.0150	0.2246	0.6491	0.0899	0.0214
	0.3	14.8	0.0437	0.2180	0.6302	0.0873	0.0208

[a] HR represents all the reacting cases, including both single- and dual-fuel cases.

and HR-series (HR1, HR2 and HR3) are the single-fuel cases, which have been studied in the ECN Spray-H experiments [38]. They are selected for validation of the current LES models under non-reacting (HN) and reacting spray (HR-series) conditions, respectively. The validation of the non-reacting spray is only performed at the ambient temperature of 1000 K due to the absence of experimental data at lower ambient temperatures. The validation of the reacting spray is performed at ambient temperatures of 900, 950 and 1000 K.

HRA, HRB and HRC-series are the dual-fuel cases with respect to different methanol concentrations, ambient temperatures and the start of injection (SOI) times. To be more specific, effects of ambient methanol concentration on pilot fuel ignition characteristics are subsequently investigated in cases in the HRA series at the ambient temperature of 900 K. The ambient temperature of 900 K is selected since the associated interaction between methanol and n-heptane is stronger than higher ambient temperatures [135]. Case HRA1 is identical to the case HR3, serving as the model validation case and the baseline reference condition for the evaluation of the effects of the ambient mixture equivalence ratio on the dual-fuel combustion process. Cases HRA2 and HRA3 are the dual-fuel cases, with different methanol concentrations (ϕ_m = 0.1 and 0.3) in the ambient mixture. Effects of the ambient temperature are studied in cases in the HRB series with ambient temperatures of 900, 950, and 1000 K. Case HRB1 is the baseline case for the HRB series, the ambient mixture equivalence ratio of 0.3 is chosen as it corresponds to medium-load conditions in dual-fuel engines [92]. Similarly, the HRC-series cases are studied to investigate the effects of SOI on the auto-ignition, flame stabilization, and pollutant formations in the dual-fuel spray combustion.

Table 5.3 shows the numerical models used in the current study, the main model constants are denoted in the footnote of the table. In all cases, the liquid n-heptane is delivered into the CVV from the injector nozzle, which has a diameter of 0.1 mm while the fuel injection pressure is fixed at 150 MPa. The injection

Table 5.2: Operating conditions of the n-heptane fueled spray LES cases.

Cases	T [K]	P [MPa]	O_2 [%][a]	ϕ_m	SOI [ms]
HN	1000	4.29[b]	0	0	0
HR1	1000	4.18	21	0	0
HR2	950	3.97	21	0	0
HR3	900	3.76	21	0	0
HRA1 (cf. HR3 [c])	900	3.76	21	0	0
HRA2	900	3.75	20.71[d]	0.1	0
HRA3	900	3.74	20.15	0.3	0
HRB1	1000	4.16	20.15	0.3	0
HRB2	950	3.95	20.15	0.3	0
HRB3 (cf. HRA3)	900	3.74	20.15	0.3	0
HRC1 (cf. HRB1)	1000	4.16	20.15	0.3	0
HRC2	1000	4.16	20.15	0.3	0.3
HRC3	1000	4.16	20.15	0.3	0.6
HRC4	1000	4.16	20.15	0.3	0.9
HRC5	1000	4.16	20.15	0.3	1.2

[a] The volumetric concentration.
[b] The initial pressures are changed with the ambient temperatures and compositions to maintain a density of 14.8 kg/m^3.
[c] This case serves as the baseline case for the HRA series to study the effects of ϕ_m. The condition is identical to the case HR3.
[d] The ambient primary fuel-air is a mixture of methanol with air (the same composition with that in single-fuel cases). The addition of methanol reduces the oxygen volumetric concentrations.

nozzle is installed on the inner wall of the CVV. The injection duration is set to 6.6 ms, providing a total pilot fuel mass of 17.5 mg. The total mass of the liquid droplets is adopted from the ECN experiment [38], while the injection mass flow profile is modelled using the method described in Ref. [136]. The primary breakup of the droplets is considered using a Rosin-Rammler size distribution, with model parameters n set as 3, d_{max} restricted to the nozzle hole diameter 100 µm and d_{mean} set as half of the d_{max}. The secondary break-up process is modelled using a hybrid Kelvin Helmholtz–Rayleigh Taylor (KH-RT) model [137]. The above mentioned LPT models have been adopted in the previous spray studies [49, 138, 139]. The unclosed SGS terms in momentum, species, and energy equations are modelled using a k-equation eddy-viscosity model [140]. The model constants, C_k and C_e, are set to 0.07 and 0.3, respectively.

The local equivalence ratio of the gaseous fuel mixture (including both methanol and n-heptane) and mixture fraction (considering gaseous n-heptane only) are

Table 5.3: Numerical models and methods used in the LES spray combustion.

	Models
Initial droplet size	Rosin-Rammler distribution[a]
Break-up model	KH-RT model[b]
Turbulence model	LES with k-equation model
Combustion model	Partially-stirred reactor
Chemistry acceleration method	Chemistry coordinate mapping (CCM)[c]
Chemical mechanism	68-species mechanism [27]
NOx mechanism	Extended Zeldovich[4]
Soot mechanism	Multi-step soot model[93]

[a] The number of parcels is set as 20 million per second; The maximum size is 100 μm and mean value is half of the maximum.

[b] The model constant, B_1, is set as 18 as suggested by Ref. [141, 142]. The droplet RT breakup diameter constant, C_{rt}, is chosen as 0.1.

[c] Mapping coordinates are mixture fraction, temperature, scalar dissipation rate and fuel mass fraction.

[4] It has 4 species and 13 reactions, which is added to the current skeletal mechanism [92].

introduced. The local equivalence ratio, ϕ, is defined in Eq. (5.1) as suggested in Ref. [143].

$$\Phi(x, y, z) = \frac{2X_C + 0.5X_H - X_O + \theta X_N}{\theta X_N} \tag{5.1}$$

where X_C, X_H and X_O are the C, H, O element mole fraction, θ is the ratio of the initial oxygen/nitrogen mole fraction. The ambient local equivalence ratio is $\phi = 0$ in single-fuel cases, and $\phi = \phi_m$ in dual-fuel cases.

In dual-fuel combustion, the conventional Bilger mixture fraction is not able to track the contribution of the pilot fuel to the local equivalence ratio as the ambient mixture contains the primary fuel. For this reason, a transport equation for the mixture fraction is employed. In this equation, only the pilot fuel injection is included in the source term, while methanol is excluded. $Z = 0$ indicates the mixture without the pilot fuel vapour, while $Z = 1$ is at the mixture of pure vapour pilot fuel. The ambient mixture fraction is zero in both single- and dual-fuel combustion cases. Assuming that the stoichiometric n-heptane/air mass ratio is γ_A, $\gamma_A = (m_{air} + m_{methanol})/m_{pilot}$. m_{pilot} and $m_{methanol}$ are the sum of the mass of materials that are originated from the pilot fuel stream and ambient methanol, the stoichiometric mixture fraction, Z_{st}, is defined as:

$$Z_{st} = \frac{1}{1 + \gamma_A}. \tag{5.2}$$

5.1.1 Study on mesh resolution

The computational domain is a cube with a side length of 108 mm. A locally refined grid system is employed with the finest cell size of 0.125, 0.25, 0.375, and 0.5 mm. A grid sensitivity study was carried out first to examine the sensitivity of the mesh size.

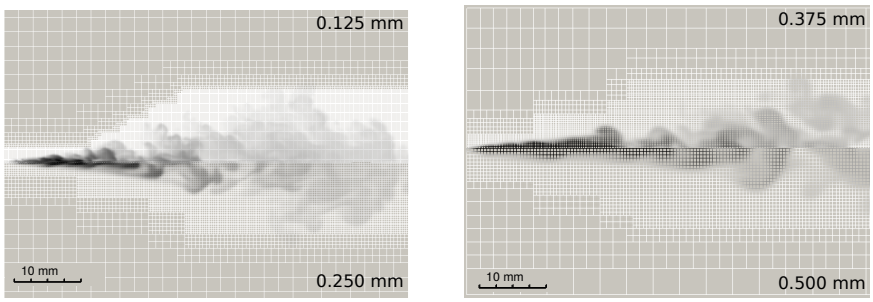

Figure 5.1: A snapshot of the 0.125 mm and 0.25 mm mesh (left), 0.375 mm and 0.5 mm mesh (right) grids in the streamwise cross-section, and the mixture fraction (Z) field at 1.5 ms ASI.

Figure 5.1 shows a snapshot of the mesh and mixture fraction distribution of a streamwise cross-section in the 0.25 and 0.125 mm meshes at 1.5 ms ASI. As shown, the spray is well captured in the refinement regions, which are coaxial cylinders or cones. The 0.5, 0.375 and 0.25 mm meshes consist of four cylinders in the nozzle axial direction. In the 0.125 mm mesh, the liquid region is enveloped by a cylinder of 4 mm diameter and 12 mm height. Another cylinder with a diameter of 20 mm is applied to capture the vapour region from 24 mm downstream. These two cylinders are connected by a cone. Each mesh has a uniform resolution in the spray region extending to 108 mm downstream. The total number of computational cells is 0.37, 0.89, 1.93 and 14.2 million in the 0.5, 0.375, 0.25, and 0.125 mm meshes, respectively.

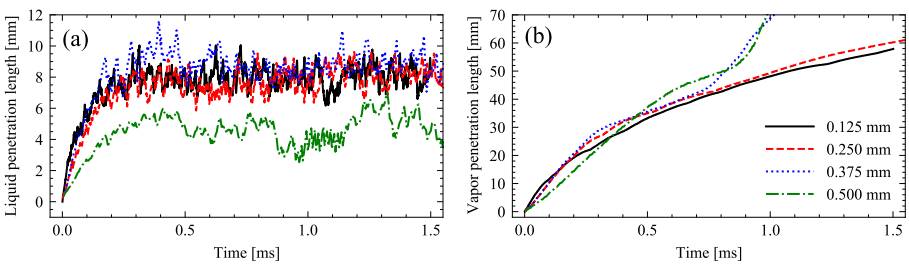

Figure 5.2: Evolution of (a) the liquid penetration length, and (b) vapor penetration length from LES with mesh size of 0.125, 0.25, 0.375 and 0.5 mm.

Figure 5.2 shows LPL and VPL in the non-reacting case HN. In the LES, LPL is defined as the maximum distance from the nozzle outlet to the downstream position in the streamwise direction where the liquid fuel mass within this region accounts for 95% unevaporated liquid mass in the domain. Following the recommendation of ECN [38], the VPL from the numerical simulations is defined as the maximum distance from the injector nozzle to the location where the fuel mass fraction reaches 0.1%. It is seen in Fig. 5.2a and 5.2b, the 0.5 mm mesh predicts a shorter LPL. Both the 0.5 mm and 0.375 mm meshes predict a higher VPL after 0.8 ms ASI. This over-prediction is solved in the 0.25 mm resolution, which also shows similar VPL and LPL results with 0.125 mm mesh. The 0.25 mm mesh provides a reasonable resolution in terms of the vapour and liquid penetration prediction.

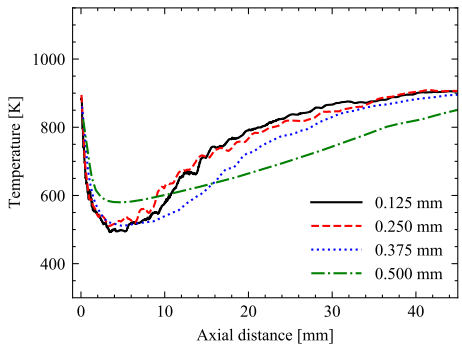

Figure 5.3: The axial distributions of the temperature from non-reacting LES with mesh size of 0.125, 0.25, 0.375 and 0.5 mm.

Figure 5.3 shows the time-averaged radial profiles of the temperature in simulations with mesh size of 0.125, 0.25, 0.375, and 0.5 mm. The results are obtained in the non-reacting LESs, in which the temperature is averaged from 1.0 ms to 1.5 ms ASI. A rapid temperature drop is observed in the liquid region due to evaporation. The temperature is increasing in the mixing region downstream. It is seen that the 0.5 and 0.375 mm mesh predicts a higher temperature in the liquid region and a lower temperature in the mixing region. The 0.25 mm mesh shows a fairly good agreement with the 0.125 mm mesh.

The mesh sensitivity analysis shows that a reasonable resolution of the spray and evaporation is obtained using a resolution of the refined mesh of 0.25 mm. A maximum CFL number of 0.1 is used for all the cases. The typical time step of the temporal integration is 50 ns under such CFL number and mesh size. In addition, the finite rate chemistry integration (with the Seulex ODE solver) is done with an initial time step of 0.1 ns. This mesh and time steps are adopted in Paper I, II and III, where the validation of the LPL, VPL, pressure rise and

soot volume fraction against the experiments is presented.

5.1.2 Performance of chemical kinetic mechanism

A skeletal chemical mechanism (denoted as Lu-68) developed by Lu *et al.* [27] with 68 species and 283 reactions are employed in this study for the prediction of the n-heptane/methanol dual-fuel combustion. This mechanism was also adopted in LES on n-heptane spray combustion [67] and the direct numerical simulation of n-heptane/methanol dual-fuel combustion [135].

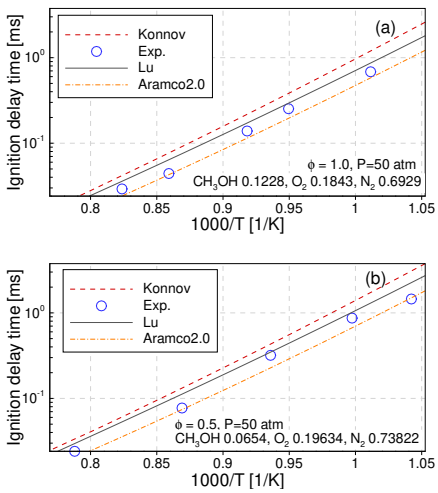

Figure 5.4: IDT predicted using different mechanisms for (a) stoichiometric and (b) lean methanol/air mixture with equivalence ratio of 0.5 at a pressure of 50 bar under different initial temperatures. The symbols represent the high-pressure shock-tube experimental data from National University of Ireland (NUI) Galway [144]. Reproduced from Paper I.

An evaluation of the methanol sub-mechanism in the Lu-68 n-heptane mechanism is conducted to investigate the accuracy of this mechanism in the prediction of the ignition process in the ambient methanol/air mixture. A similar validation approach was reported in Ref. [49] for the duel-fuel study of n-dodecane/methane, while the current work investigates the n-heptane/methanol. Figure 5.4 shows the IDTs of stoichiometric and lean methanol/air mixture (equivalence ratio of 0.5) predicted by the Lu-68 mechanism and two detailed methanol mechanisms, as well as the corresponding high-pressure shock-tube measurements at the National University of Ireland (NUI) Galway [144]. The initial pressure is chosen as 50 bar, which is similar to the current spray flame cases. The two detailed methanol mechanisms considered are the Aramco 2.0 mechanism [145] and the Konnov mechanism [146]. It is shown that the IDTs

predicted using the Lu-68 mechanism are comparable to those calculated using the detailed mechanisms and the shock tube measurement.

5.2 Low- and high-temperature ignitions

In the single-fuel Spray-H flame, two-stage ignitions are observed in both experiments [38] and simulations [66]. As suggested by ECN [38], the first- and second-stage IDTs are defined as time intervals from the start of injection to the time at which the first peak and the maximum time derivative of temperature occurs. The two-stage IDTs are henceforth denoted as τ_1 and τ_2 for brevity. The first- and second-stage ignitions are also known as low- and high-temperature ignitions. Apart from the two-stage ignitions, the auto-ignition of the ambient methanol/air mixture is also observed in the dual-fuel combustion. Figure 5.5 shows the maximum and mean temperature in dual-fuel case HRC1. T_{max} is the maximum temperature within the spray region, $Z > 0.001$. The mean value, T_{mean}, is calculated from the volume-averaged temperature. The IDT of the ambient methanol/air mixture, τ_{amb}, is then defined as the time at which the maximum time derivative of the ambient averaged temperature is achieved.

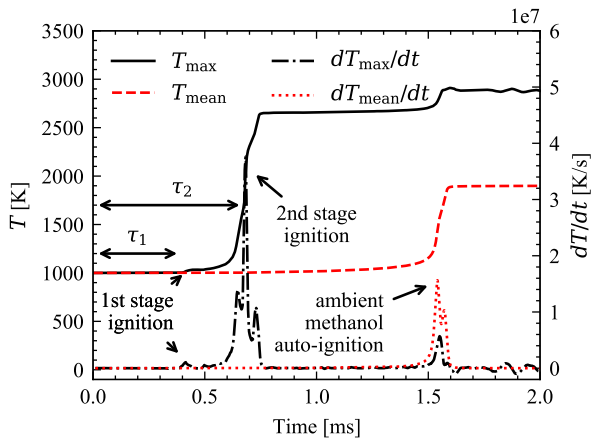

Figure 5.5: The temporal evolution of the maximum temperature, T_{max}, volume averaged temperature, T_{mean}, and its time derivative dT/dt in dual-fuel case HRC1.

In n-heptane/methanol dual-fuel spray combustion, during the liquid n-heptane injection, the oxidation reactions in the methanol-air mixture take place, but not to the critical point of auto-ignition. This period of time is referred to as the ignition induction time. It is clear that with sufficiently long induction time the methanol-air mixture would auto-ignite, even without the participation

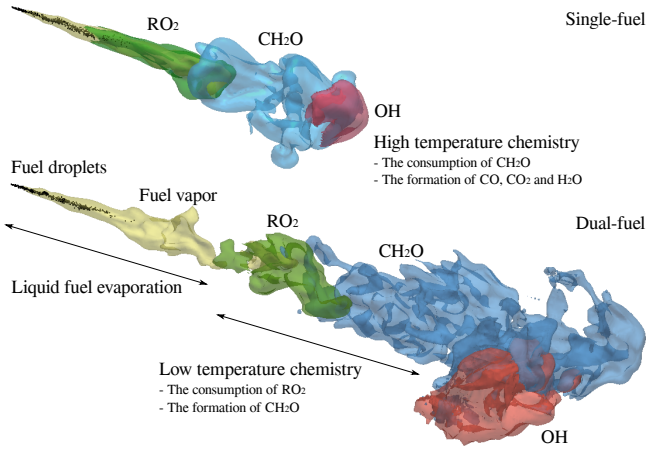

Figure 5.6: Three-dimensional flame structure at the instance of second-stage ignition for the single-fuel HRA1 (upper) and dual-fuel HRA3 (bottom). Black dots indicate the fuel droplets. The yellow, green, blue and red cloud represent n-heptane vapor, RO_2, CH_2O and OH. Reproduced from Paper I.

of n-heptane. This implies that in the present n-heptane/methanol dual-fuel combustion process, the effects of methanol chemistry on the n-heptane ignition is different at different spatial locations of the spray jet due to the variation in the induction time. Figure 5.6 shows the three-dimensional flame structure of single-fuel (HRA1) and dual-fuel combustion (HRA3) at the instance of second-stage ignition. The n-heptane is delivered as a liquid fuel. The liquid n-heptane droplets breakup and evaporate to fuel vapour in the immediate downstream of the fuel jet. The intermediate species, such as RO_2 and CH_2O, are produced in the low-temperature ignition region. As can be seen in Fig. 5.6, the fuel vapour is enveloped by the RO_2 in the single-fuel case, while the RO_2 region in the dual-fuel case is downstream of the fuel vapour region. The high-temperature ignition occurs further downstream of the spray, where the intermediate species are oxidized to CO_2 and H_2O with the participation of radicals such as OH. CH_2O appears and stabilizes after the first stage ignition, indicating the onset of the cool flame. The appearance of OH leads to quick reactions and a rapid heat release, indicating the onset of the high-temperature flame. The ambient methanol/air mixture retards the onset of the first-stage ignition, affects the cool flame structure, and postpones the onset of the second-stage ignition kernel further downstream.

A series of homogeneous reactor simulations (0-D) was conducted to identify the reaction path and explain the effects of methanol on the ignition process. Fig. 5.7 shows the n-heptane/methanol reaction path. This path is divided into two parts, the first part indicates the fuel oxidation reaction path by tracing the C atom, the second part is traced from O atom flow including radicals

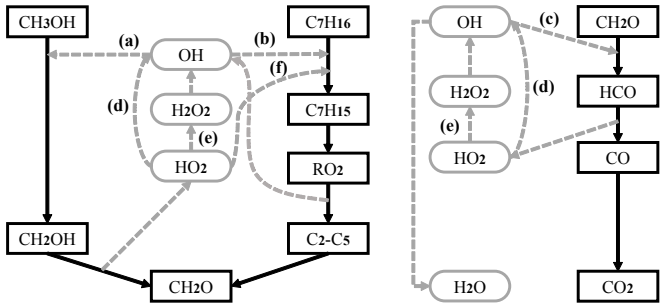

Figure 5.7: The main reaction paths for CH_3OH, n-heptane and air oxidation before ignition. The black arrow lines represent C atom flow while the gray ones for O atom flow.

such as OH and HO_2, denoted as black solid and grey dash arrow lines, respectively. The ambient CH_3OH contributes to the consumption of OH through $CH_3OH+OH \Rightarrow CH_2OH+H_2O$ reaction. This reduces the OH accumulation rate, afterwards prolonging the first-stage ignition delay τ_1. Meanwhile, the intermediate products CH_2OH is formed from CH_3OH dehydrogenation in an ambient methanol-air mixture. Then, the oxidation CH_2OH ($CH_2OH+O_2 \Rightarrow CH_2O+HO_2$) will generate a large amount of HO_2, which is in favour of the first stage ignition. On one hand, the HO_2 formed from ambient CH_2OH oxidation will involve the C_7H_{16} dehydrogenation through reaction path (f) $C_7H_{16}+HO_2 \Rightarrow C_7H_{15}+H_2O_2$. However, the proportion of this reaction path (f) is only 3% in the $\phi_m = 0.3$ case. On the other hand, HO_2 will be converted to H_2O_2 and forms OH through $H_2O_2+M \Rightarrow OH+OH+M$ reaction (denoted as R1). This reaction has high activation energy, the supplement of OH from the methanol-air mixture is limited before the temperature increases up to 1000 K [147]. In other words, the OH is consumed but cannot be replenished in low-temperature reactions. Therefore, the maximum OH mass fraction in the dual-fuel combustion is lower than that of single-fuel case. The detailed mechanism of the two-stage ignition retardation effect in methanol involved dual-fuel combustion is discussed in Paper I.

5.3 Cool flame and high temperature flame

5.3.1 Cool flame

As an indicator of the cool flame, CH_2O is used to study the evolution of the cool flame. Figure 5.8 shows the temporal evolution of the averaged CH_2O mass fraction, $\overline{Y}_{CH_2O}(z,t)$, for a given axial locations z, which is the injection axis.

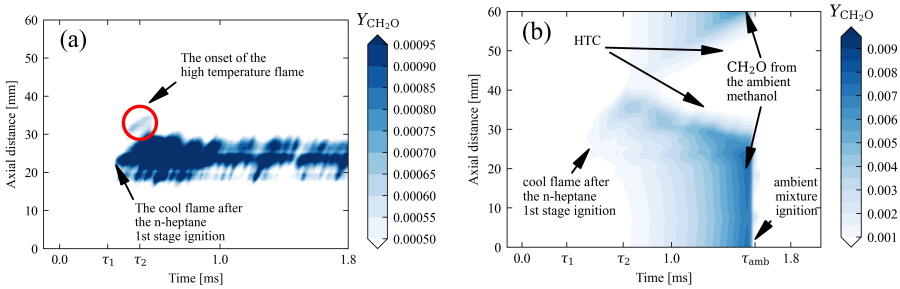

Figure 5.8: Temporal evolution of the averaged CH_2O mass fraction at given axial locations, $\overline{Y}_{CH_2O}(z,t)$ in (a) single-fuel case HR1, and (b) dual-fuel case HRB1.

At each time step, the CH_2O mass fraction is averaged in the cross-flow (x-y) plane, as shown in Eq (5.3).

$$\overline{Y}_{CH_2O}(z,t) = \frac{\int\int Y_{CH_2O}(x,y,z,t)dxdy}{\int\int dxdy} \tag{5.3}$$

In Fig. 5.8a, CH_2O appears after the first stage ignition τ_1 at around 20 mm, indicating the onset of the cool flame. The cool flame propagates downstream reaching 35 mm at the second stage ignition τ_2. After that, the downstream CH_2O is consumed immediately in the reaction $CH_2O + OH = HCO + H_2O$. Hence, the tip of the CH_2O propagates downstream first and then shrinks upstream. Hence, an isolated region can be found in Fig. 5.8a, denoted by a red circle. Finally, the cool flame is stabilized in the single-fuel spray combustion case. In contrast, the onset of the cool flame in the dual-fuel case occurs further downstream at around 25 mm. Since CH_2O is also formed in the auto-ignition reactions of the ambient methanol, CH_2O is subsequently observed both downstream and upstream and its mass fraction increases with time. A wedge-shaped region with low CH_2O mass fraction is found in Fig. 5.8b after 0.7 ms. This is attributed to the high-temperature flame propagating both downstream and upstream after the second stage ignition. After the auto-ignition of the ambient mixture τ_{amb}, CH_2O disappears quickly, indicating that the cool flame is eliminated after the ambient methanol auto-ignition.

5.3.2 High-temperature flame

After the second stage ignition, the high temperature reactions dominate the combustion, the high-temperature flame is then established. Following the recommendation of Refs.[49, 148], the associated chemistry is known as HTC,

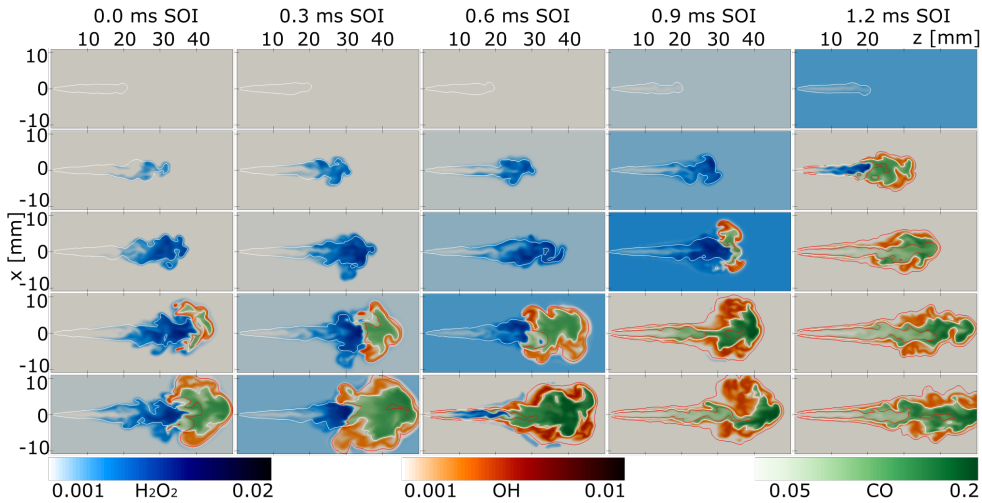

Figure 5.9: Two-dimensional snapshots (in x–z plane) of the mass fractions of H_2O_2, OH and CO in dual-fuel case HRC1 to HRC5 (from left to right). To avoid the overlaps, species mass fraction are truncated by a given threshold, e.g., mass fraction thresholds are 0.1% for H2O2 and OH, 5% for CO. The snapshots are sampled at 0.2-1.0 ms ASI (from top to bottom) with an uniform interval time of 0.2 ms. The iso-contours are $T = 2000$ K (red line) and stoichiometric mixture line (white line).

which is identified by the consumption of H_2O_2. To demonstrate the role of ambient methanol on the formation of a high-temperature ignition kernel, Fig. 5.9 shows the distribution of mass fractions of hydrogen peroxide (H_2O_2), hydroxyl (OH) and carbon monoxide (CO). In the short ignition induction time cases HRC1 (0 ms SOI) HRC2 (0.3 ms SOI) and HRC3 (0.6 ms SOI), H_2O_2 is firstly formed on the rich side, $Z > Z_{st}$. Subsequently, it expands towards lean mixtures. However, in the longer ignition induction time cases HRC4 (0.9 ms SOI) and HRC5 (1.2 ms SOI), H_2O_2 is firstly formed on the lean side. This is because the H_2O_2 mass fraction in the ambient mixture increases significantly with the increase of SOI, thus the ambient H_2O_2 appears earlier in the longer ignition induction time cases. For instance, the H_2O_2 mass fraction in the ambient mixture at 0.2 ms ASI in HRC5 (1.2 ms SOI) is even higher than that at 1.0 ms ASI in HRC1 (0 ms SOI). The presence of H_2O_2 gives rise to the formation of OH through reaction R1, which promotes the onset of high-temperature ignition. As a consequence, the formation of the high-temperature ignition kernel in the spray region is getting ahead in the high ambient H_2O_2 concentration cases.

Figure 5.9 also shows the flame structure after the ambient methanol auto-ignition. The ambient methanol auto-ignition occurs at 0.953, 0.656 and 0.357 ms ASI in Cases HRC3, HRC4 and HRC5, respectively. The ambient H_2O_2 is rapidly consumed in HTC after methanol auto-ignition. However, residual H_2O_2

is found on the rich side upstream after the ambient methanol auto-ignition, e.g., 1.0 ms in HRC3 and 0.4 ms in HRC5. This is due to the high activation energy of R1. The temperature on the fuel-rich side upstream is rather low due to n-heptane evaporation. It is also observed that the maximum CO and OH concentrations increase after the ambient methanol auto-ignition, whereas the locations of CO and OH resemble that before auto-ignition. Due to the lack of oxygen on the fuel-rich side, CO is formed in the high temperature (T >2000K) and rich side ($Z > Z_{st}$) as a product of incomplete combustion. OH is enveloped by the iso-contours of $T = 2000$ K and stoichiometric mixture line. The detailed flame structures after ambient methanol auto-ignition are discussed in Paper III.

5.4 Soot and NOx formation

In Paper II, the soot and NOx emissions in single- and dual-fuel combustion under ambient temperatures of 900, 950, and 1000 K are discussed. It is observed that dual-fuel combustion has a significant lower soot and NOx emissions at 900 K, however, high emissions at 1000 K. To explain the increase of soot and NOx in the 1000 K dual-fuel case, the spatial distributions of intermediate products and pollutants are plotted in Figures 5.10 and 5.11, respectively.

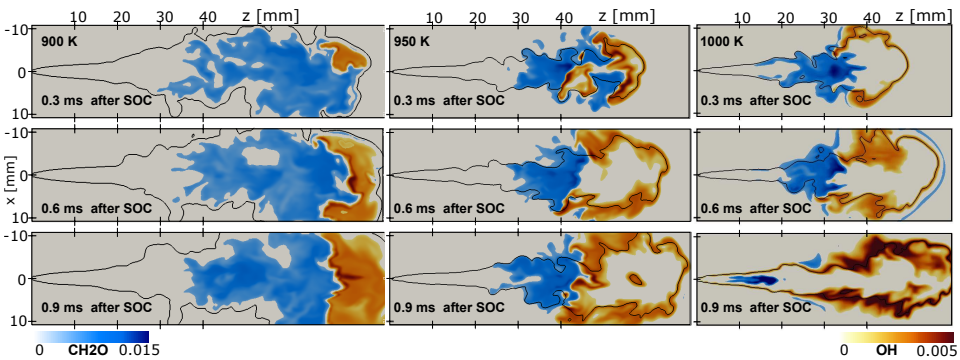

Figure 5.10: Snapshots of the spatial distribution of mass fractions of formaldehyde, Y_{CH_2O}, and hydroxyl radicals, Y_{OH}, in the 900, 950 and 1000 K dual-fuel cases, $0.3 - 0.9$ ms after SOC. The black line is iso-contour of $\phi = 1$.

It appears that soot formation occurs in the overlapping region of the fuel-rich ($\phi > 2$) and intermediate temperatures (1600 K $< T <$ 2300 K), while NOx is formed in oxygen-rich and high-temperature region. This is consistent with the observation of soot-NOx trade-off in previous studies on single-fuel spray combustion [72]. The main factor for the increase of soot and NOx is that ambient methanol-air combustion alters the $\phi - T$ distribution in the dual-fuel combustion. In the 1000 K dual-fuel case, at 0.6 ms after the start of combustion

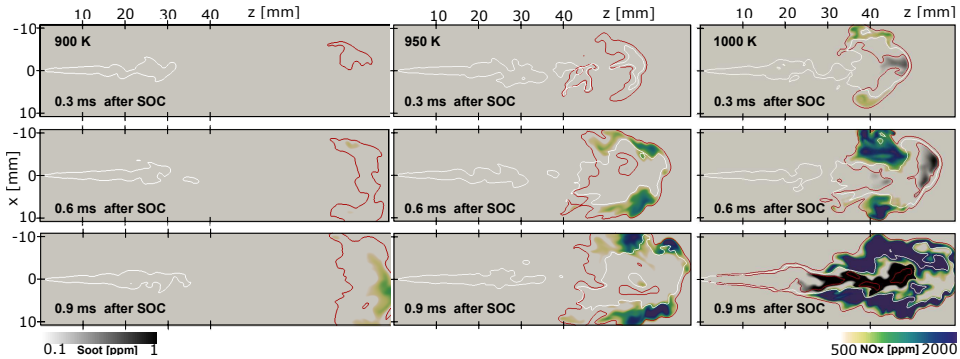

Figure 5.11: The distribution of NOx mass fraction, Y_{NOx}, and soot volume fraction, f_v, in the 900, 950 and 1000 K dual-fuel cases, 0.3–0.9 ms after SOC. The white and red lines represent ϕ=2 and T = 2300 K, respectively.

(SOC), a premixed flame is found on the tip of the spray, cf. Fig. 5.10, where the iso-contour of $\phi = 1$ (black line) is surrounded by a thin layer of CH_2O. Shortly after the development of this premixed flame, i.e., at 0.86 ms after SOC, the premixed methanol/air mixture in the ambient starts to auto-ignite. The auto-ignition of the ambient methanol/air mixture is defined as the time in which the maximum time derivative of the averaged temperature in the domain is achieved. Due to the heat release in ambient methanol-air auto-ignition, the ambient mixture increases up to approximately 1900 K. However, the n-heptane is still injected from the nozzle at the moment. The evaporation of pilot fuel is therefore accelerated. The evaporated n-heptane is burnt rapidly in upstream regions where the mixture has a high local equivalence ratio. This can be seen from the distribution of OH radicals in the upstream region that envelopes the entire liquid fuel. On the other hand, the oxygen concentration in the entire domain is reduced to 15% after auto-ignition. Thereby, a significant amount of soot is formed continuously in its high-temperature production zone, while the soot oxidation is suppressed due to the reduced oxygen in the ambient. For the same reason, the combustion of ambient mixture expands the high-temperature region, leading to a higher NOx formation rate. Consequently, the total mass of soot and NOx in the 1000 K dual-fuel case escalates after the auto-ignition of the ambient methanol-air. For more details, readers are referred to Paper II.

Chapter 6

Impact of operating condition on dual-fuel combustion

In this chapter, the effects of the dual-fuel strategies, including the primary fuel concentration (Paper I), the ambient temperature (Paper II) and the pilot fuel injection timing (Paper III) are studied.

6.1 Effects of primary fuel concentration

An engineering challenge in the dual-fuel engine is the control of ignition time and HRR [149]. The primary fuel concentration is one of the critical factors for ignition timing. In practice, the distribution of the primary fuel/air mixture may not be perfectly homogeneous in dual-fuel engines [150]. On the other hand, methanol concentration represents the engine loads in the diesel/methanol dual-fuel engines. Therefore, understanding the effects of the primary fuel concentration is essential to the dual-fuel strategy design. This has motivated the present study.

6.1.1 Effects of ambient methanol on pressure rise and HRR

Figure 6.1 shows the temporal evolution of pressure rise (the difference between the chamber pressure and its initial pressure) and net HRR (the heat release rate term integrated over the entire chamber) for cases HRA1, HRA2, and HRA3 (the conditions of the cases are referred to Chapter 5). In this figure, black,

blue, and green lines correspond to the equivalence ratios of 0, 0.1, and 0.3, respectively; the solid line is the pressure rise after the start of injection while the dash line represents the HRR. It is worth noting that the HRR here is the volume integration of chemical source term. The benefit of this treatment is to get rid of the effect of evaporation. Before the onset of ignition, the chamber pressure decreases due to the endothermic evaporation process during the n-heptane injection. This is followed by a pressure rise alongside a noticeable HRR, indicating the onset of ignition. Both the initial HRR and the pressure-rise rate are rather low; this stage of ignition and heat release are known as the first-stage ignition and heat release. Thereafter, around 0.6 ms ASI, HRR increases rapidly to a substantially high value, along with a rapid increase of chamber pressure. The start of the high HRR indicates the onset of second-stage ignition, associated with the second stage heat release. This two-stage heat release process is observed for the n-heptane fuel, while pure methanol ignition has only one stage heat release [147]. It is found that the higher the methanol-air equivalence ratio in the ambient mixture, the lower the peak HRR from the first-stage ignition. In contrast, a high methanol-air equivalence ratio results in a high second stage HRR.

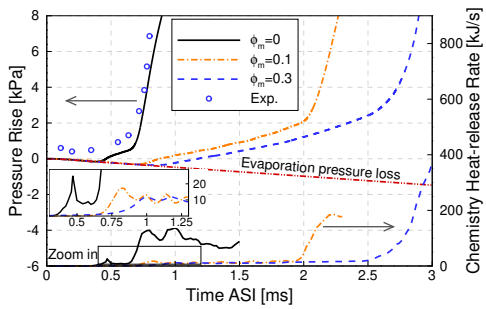

Figure 6.1: Effects of ambient methanol concentration on pressure rise and total heat-release rate for cases HRA1, HRA2, and HRA3 with ambient methanol equivalence ratio varying from 0 to 0.3. The experimental pressure rise is shown using symbols. Reproduced from Paper I.

Figure 6.2 shows the evolution of the maximum chemical HRR in the computational domain for cases HRA1, HRA2, and HRA3. A semi-logarithmic coordinate is used to demonstrate the two-stage heat releases and the weak heat release before the first-stage ignition. The two-stage heat releases are demonstrated by the two plateaus in the figure. It is found that the single-fuel case has the highest maximum chemical HRR in the first-stage heat release, which is consistent with the observation in Fig. 6.1. On the contrary, the maximum chemical HRR of the single-fuel case is the lowest in the second-stage heat release. It is also found that the dual-fuel case HRA2 ($\phi_m = 0.1$) and HRA3 ($\phi_m = 0.3$) have

a higher HRR before 0.15 ms ASI, as shown in the inset of Fig. 6.2.

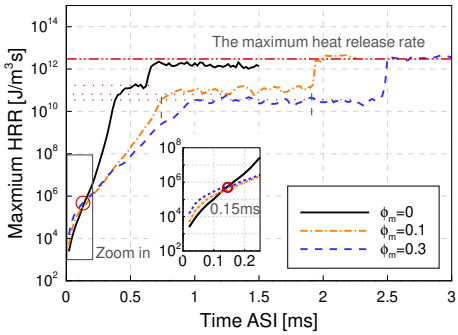

Figure 6.2: The maximum chemical heat-release rate in the domain for the reacting HRA1, HRA2, and HRA3. Reproduced from Paper I.

6.1.2 Effects of ambient methanol concentration on the ignition process

As shown in the inset of Fig. 6.1, where the first-stage HRR is displayed, the onset of first-stage ignition is retarded in the dual-fuel cases ($\phi_m = 0.1$ and $\phi_m = 0.3$). A higher methanol-air equivalence ratio in the ambient mixture leads to a longer retardation time of the first-stage ignition. Moreover, the ambient methanol also retards the second-stage ignition, evident by the time difference between the second-stage ignition and the first-stage ignition, which increases with the increase of ϕ_m in the ambient mixture.

Figure 6.3 shows the temporal evolution of RO_2 and OH mass fractions in the most reactive local mixture, which is the computational cell with the highest HRR. The spatial location of the most reactive local mixture changes with time. The most reactive local mixture is tracked to investigate how it evolves and where it is located.

RO_2 has been recommended by ECN [38] as the indicator of the first-stage ignition: the first-stage IDT is suggested to be at the time of RO_2 mass fraction reaching 20% of its maximum, denoted as τ_1 in Fig. 6.3a with the vertical dashed lines. It is interesting that even though methanol in the ambient mixture retards the first-stage ignition, cf. Fig 6.1, The maximal mass fraction of RO_2 in the most reactive mixture is higher initially (before 0.15 ms ASI) in the cases with higher methanol concentration in the ambient mixture. This indicates that the ambient methanol enhances the production of RO_2. However, shortly after 0.15 ms ASI, the suppression effect of methanol on RO_2 is evident.

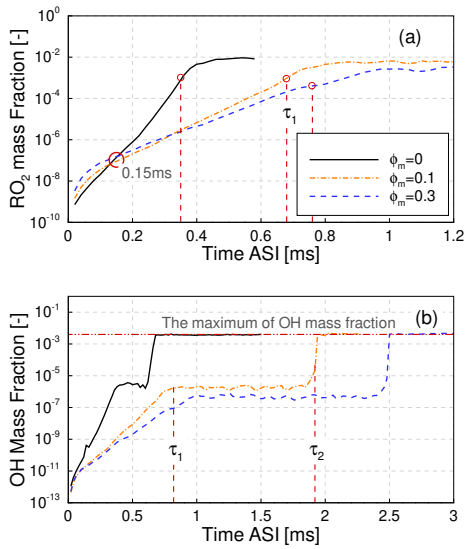

Figure 6.3: Temporal evolution of mass fraction of RO_2, Y_{RO_2} (a), and OH, Y_{OH} (b), in the most reactive local mixture for HRA1, HRA2 and HRA3 (with ϕ_m varying from 0 to 0.3), respectively. The vertical dashed lines indicate the time of first-stage ignition (τ_1, a) and the first- and second-stage ignition (τ_1 and τ_2, b). The two plateaus in the OH profiles indicate the transition period from the onset of the first-stage ignition to the onset of the second-stage ignition, and the period after the onset of the second-stage ignition. Reproduced from Paper I.

On the other hand, OH is used as the indicator for the second-stage ignition (defined at the time that the OH mass fraction exceeds 2% of its maximum value in the domain after a stable flame is established [38], denoted as τ_2 in Fig. 6.3b. It is seen that the mass fraction of RO_2 and OH of the most reactive mixture increases (approximately) exponentially with time (ASI) until it reaches a plateau shortly after τ_1, and the mass fraction of OH reaches a second plateau after τ_2. In the second-stage ignition, the maximum OH mass fraction is independent of ϕ_m, while during the transition period from the first-stage ignition to the second-stage ignition, OH mass fraction decreases with ϕ_m in the ambient mixture. The transition time from the onset of the first-stage ignition to the second-stage ignition shows an increasing retardation effect of methanol on the n-heptane ignition process with ϕ_m.

Figure 6.4 shows the $\phi - T$ diagram for the reacting cases HRA1, HRA2 and HRA3 before the first-stage ignition. The local equivalence ratio, ϕ, is defined as suggested in Ref. [143]. All of the computational cells are shown as grey dots. The dashed line is a fitting curve for the grey dots using the least-squares method. As seen in Fig. 6.1, chemical heat release is absent before the first-stage ignition for both single- and dual-fuel cases. Therefore, no obvious temperature rise is found in Fig. 6.4. Due to liquid n-heptane evaporation and

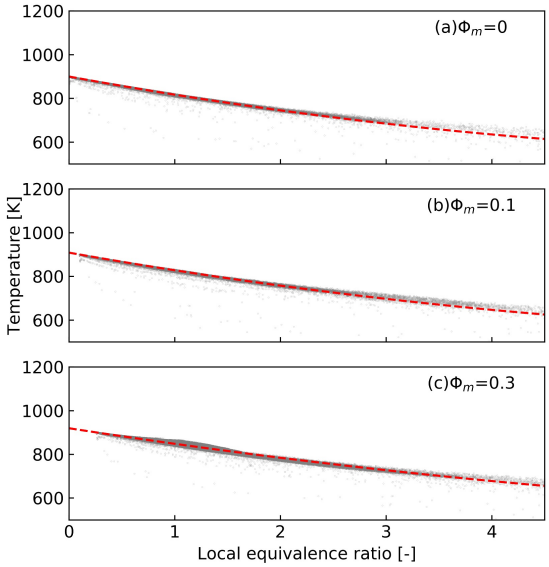

Figure 6.4: The scatter plot of all the LES cells in $\phi - T$ diagram before the first-stage ignition, and mixing lines for the case with ϕ_m of (a) 0, (b) 0.1 and (c) 0.3. Reproduced from Paper I.

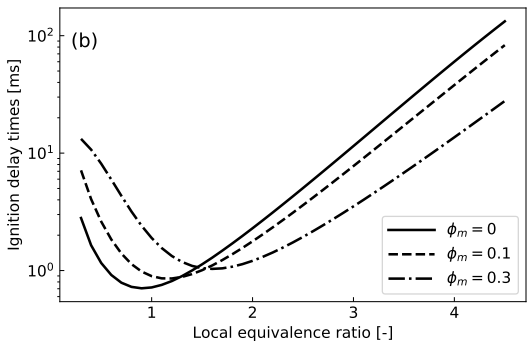

Figure 6.5: The ignition delay times of the n-heptane/methanol-air mixture in zero-dimensional homogeneous reactor simulations. The solid, dashed and dot-dashed lines denote initial methanol equivalence ratio ϕ_m of 0, 0.1 and 0.3, respectively. Reproduced from Paper I.

mixing, the local temperature decreases with the increase of the local equivalence ratio. All of the LES cells collapse into a line, which is the mixing line for the n-heptane and methanol/air mixture. Zero-dimensional homogeneous reactor simulations are conducted along the mixing line to explain the effects of methanol on the ignition of n-heptane. Figure 6.5 shows the high temperature IDTs of the n-heptane/methanol-air mixture at different local equivalence ratios. Each equivalence ratio represents a thermophysical state in the LES. The

initial composition and temperature of the zero-dimensional simulations are extracted from the mixing line in Fig. 6.4. For all of the ϕ_m, IDT first decreases and then increases with the increase of the local equivalence ratio. The shortest IDT locates at near-stoichiometric mixture for single fuel cases ($\phi_m = 0$). It is shifted to the rich region in the $\phi_m = 0.1$ and $\phi_m = 0.3$ cases. In addition, it is found that the shortest IDT increases with the increase of ϕ_m. This implies that a high methanol concentration delays the n-heptane high-temperature ignition, which is consistent with the observation in the LES.

6.2 Effects of ambient temperature

The ambient temperature, at which the pilot fuel is injected, is another important parameter in the dual-fuel engine. It is strongly associated with the emissions of the unburnt HC, NOx and soot [90, 151, 152]. In a diesel/methanol dual-fuel engine, methanol is premixed with air during the intake stroke. The methanol/air mixture temperature increases during the compression stroke. The ambient temperature is controlled by the intake air cooling, compression ratio, and injection timing.

6.2.1 Roles of ambient methanol dilution

Figure 6.6 shows the IDT from experiments as well as IDT from LES in both single- and dual-fuel cases. The IDT of the ambient mixture is also presented. Both experiments and LES show the same trend. IDT declines with the increase of ambient temperature. It is found that the ignition is retarded in dual-fuel cases. This retardation is particularly apparent in low-temperature cases. The dual-fuel IDT at 900 K is more than two times its single-fuel counterpart. It is well established that for n-heptane spray ignition a lower ambient oxygen concentration leads to a longer IDT. As illustrated in Fig. 6.6, the experimental IDTs of the n-heptane spray of 15% ambient oxygen mole fraction are approximately 35% higher than those of 21% oxygen mole fraction. In contrast, the ambient oxygen mole fraction in the dual-fuel cases is 20.15%. Yet, the IDTs of dual-fuel cases, at 900 and 950 K, are consistently longer than the single-fuel cases with 15% O_2. Therefore, the dilution of oxygen concentration is not the main factor of a longer IDT in dual-fuel cases.

Recent LES study [49] suggested that the primary fuel (methane) oxidation reactions slow down the ignition of the pilot fuel. Figure 6.7 shows a comparison of several key species in the single-fuel and dual-fuel cases at the onset of ig-

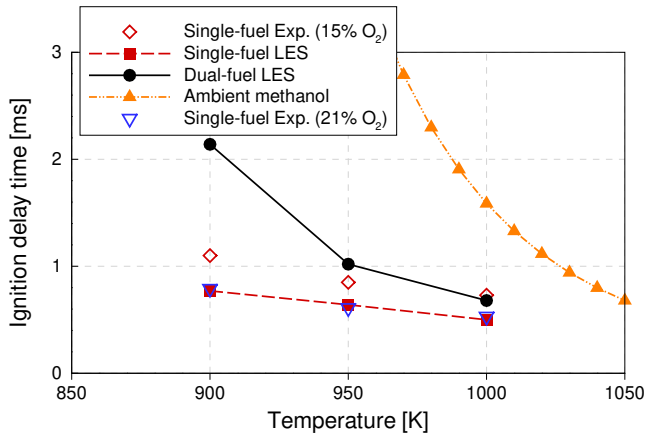

Figure 6.6: Ignition delay time of single-fuel (dash line with square) and dual-fuel (solid line with circle) predicted by the LES model. The ignition delay time of ambient fuel is denoted as dash line with triangle symbols. Experimental IDT of n-heptane spray combustion at 21% O_2 mole fraction (triangle symbol) and 15% O_2 mole fraction (diamond symbol) are also included for comparison. Reproduced from Paper II.

nition. The n-heptane nozzle is located at the origin of the coordinate (x=0, z=0). The yellow dots in Fig. 6.7 show the positions of the liquid n-heptane droplets, which break up and evaporate into gaseous n-heptane. The white line is the iso-contour of $Z = Z_{st}$. The gaseous n-heptane is decomposed/oxidized forming heptyl radical, C_7H_{15}, which undergoes subsequently either decomposition reactions to form smaller hydrocarbons or reaction with oxygen to form RO_2. The reaction path through RO_2 is the main route leading to the cool flame. With decreasing initial temperature, the RO_2 path plays an increasing role in the ignition process [153]. As can be seen, the RO_2 formation appears downstream the droplet region, followed by CH_2O further downstream. In the single-fuel n-heptane spray flame case, most of the CH_2O is generated in the fuel-rich region ($Z > Z_{st}$), which is consistent with the results reported earlier [49]. However, as shown in Fig. 6.7, a noticeable amount of CH_2O is located in the fuel-lean region ($Z < Z_{st}$) in the dual-fuel cases. In both single- and dual-fuel spray combustion, n-heptane undergoes the first and the second stage ignition, indicated by the formation of RO_2 and OH, respectively. To illustrate the participation of methanol, the mass fraction ratio of methanol/nitrogen, γ, is introduced. γ is constant (with an initial value of γ_0) over the domain if methanol is not consumed in the n-heptane reactions. As shown in Fig. 6.7, the CH_2O zone is surrounded by an iso-line (red line in Fig. 6.7) for a 10% reduction of γ, indicating that methanol participates in n-heptane ignition reactions. Moreover, the region between the white and red lines becomes broader with the decrease of ambient temperature. This indicates that the participation of methanol in the n-heptane ignition is more apparent at lower ambient

temperatures.

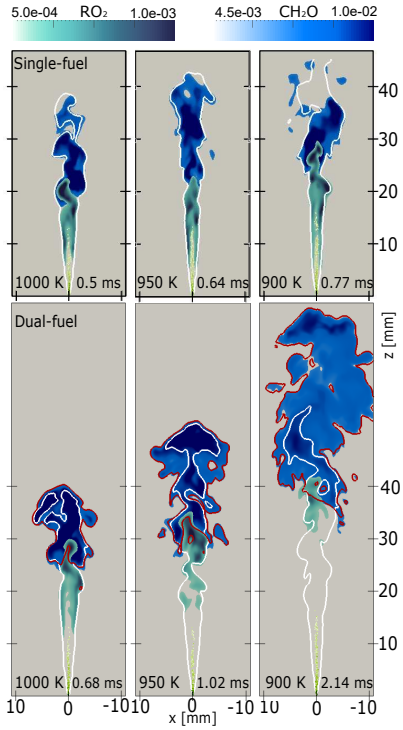

Figure 6.7: Instantaneous distribution of mass fractions of CH_2O, RO_2 and droplets in a cross-section plane along the jet axis in the single-fuel (upper row) and the dual-fuel (bottom row) cases at IDT. The yellow dots represent liquid droplets colored by droplet diameter (1 to 100 micron); the green color represents the RO_2 mass fraction (0.0005 to 0.001); the blue color shows the CH_2O mass fraction (0.0045 to 0.01). The white line is the iso-line of $Z = Z_{st}$. The red line indicates the location where the methanol/nitrogen mass fraction ratio is reduced by 10% from its non-reacting state ($\gamma = 0.9\gamma_0$). Reproduced from Paper II.

6.2.2 Role of methanol on pollutant formation

A longer IDT subsequently leads to a longer time for mixing before the start of high-temperature combustion. Consequently, the local equivalence ratio, ϕ, in the high-temperature reaction region reduces in the dual-fuel case, which is beneficial for soot reduction. Figure 6.8 are the scatter plots of LES cells in $\phi - T$ space for cases HR1 to HR3 and HRB1 to HRB3 at the quasi-steady combustion stage, where each grey dot represents a computational cell. Cells that have certain levels of soot precursor (C_2H_2) or soot, or NOx are indicated using different colours. It demonstrates the effects of delayed ignition on mixing and soot and NOx formation in $\phi - T$ diagram. The following discussion uses the 950 K single-fuel and dual-fuel cases as examples. In the single-fuel HR2 (Fig. 6.8b), the high-temperature mixture expands to the fuel-rich zone ($\phi > 2$),

which leads to the formation of a significant amount of soot precursor, and subsequently soot particles. In contrast, high-temperature combustion in the fuel-rich zone is avoided in the dual-fuel HRB2 (Fig. 6.8e). Consequently, soot precursor (red dots) and soot (yellow dots) are remarkably lower than that in the single-fuel case. It is also found that the peak temperatures in both cases are approximately the same (2630 K in HR2, and 2627 K in HRB2). The heat capacity of the ambient gas mixture in the dual-fuel case is within the margin of 2% when comparing with that in the single-fuel case. This rules out the methanol dilution effect on the heat capacity, at least under the currently studied conditions.

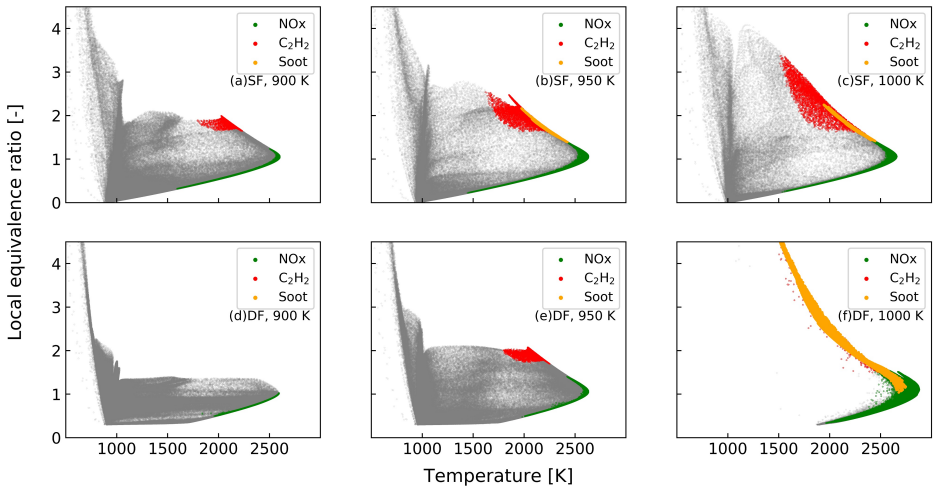

Figure 6.8: Scatter plots of LES cells in $T-\phi$ diagram for single-fuel (SF, upper row) and dual-fuel (DF, bottom row) cases at 900 (HR1 and HRB1), 950 (HR2 and HRB2) and 1000 K (HR3 and HRB3) at their respective quasi-steady combustion stage. All of the computational cells are shown as grey dots. The green dots represent the cells with high NOx emissions (NOx mass fraction exceeding 500 ppm). The orange and red dots are respectively representing cells with soot volume fraction and soot precursor C_2H_2 mass fraction exceeding their respective thresholds (0.1 ppm for soot and 0.01 for C_2H_2). Reproduced from Paper II.

The benefits of the dual-fuel strategy on reducing the local equivalence ratio of the pilot fuel spray flame are more significant in 900 K (Fig. 6.8a and d), where the maximum ϕ in the dual-fuel case is only 1.25. An absence of soot precursor and soot is observed. However, an opposite effect is found in the 1000 K dual-fuel case (Fig. 6.8f). The high-temperature region expands to a high local equivalence ratio ($\phi > 4$) region, with a massive production of soot and NOx. The low-temperature region disappears due to the auto-ignition of the ambient methanol.

Figure 6.9 shows the temporal evolution of the total masses of soot and NOx in the entire domain. The solid and dash lines represent the total masses of

soot and NOx in single-fuel cases, respectively, while the circle and triangle symbols are the soot and NOx masses in the dual-fuel cases, respectively. The non-monotonic temporal evolution of soot mass is attributed to the dynamic competition between the soot formation and oxidation processes. Similar non-monotonic temporal evolution can be found in measurements as well [38]. Soot mass is rather low in the dual-fuel cases at 900 and 950 K. However, at 1000 K a comparable amount of soot is formed in the dual-fuel and single-fuel cases within 0.8 ms after the n-heptane ignition, i.e., the SOC, followed by a more rapid increase of soot mass in the dual-fuel case. The early comparable level of soot formation in the single-fuel and dual-fuel cases can be explained by the previously discussed mixing effects. The difference between IDT in the single-fuel and dual-fuel cases is negligible at 1000 K; thus, the mixing times in the two cases are comparable. The later significantly increased soot emission (after 0.8 ms SOC) is consistent with the increased soot emission in an dual-fuel engine experiment [151], where soot emission was found to be higher when the pilot fuel injection was retarded. Retarded injection of the pilot fuel has a similar effect to that of shortened ambient primary fuel ignition.

6.3 Effects of pilot fuel injection timing

As mentioned in Section 6.2, the primary fuel and pilot fuel are delivered at different times. The time interval is referred to as the ignition induction time. An advanced SOI timing leads to a short ignition induction time and vice versa. During the ignition induction time, the ignition reactions in the primary fuel-air mixture take place.

Wang *et al.* [154] pointed out that this induction time is of great importance for the ignition timing in the methane/diesel dual-fuel spray combustion. The diesel ignition is retarded with an advanced SOI. This becomes more severe in the methanol-fueled dual-fuel spray combustion as methanol has a shorter ignition delay time compared to methane. The ambient methanol auto-ignition is able to be triggered before the diesel injection with a late SOI. For this reason, the self-ignition behaviour of the ambient methanol before the n-heptane injection cannot be ignored, especially for the high ambient temperature conditions. Set against these backgrounds, LES cases HRC1 to HRC5 with induction time ranging from 0 to 1.2 ms were configured and simulated. The induction time effects on the n-heptane IDT and flame structures are discussed in this section.

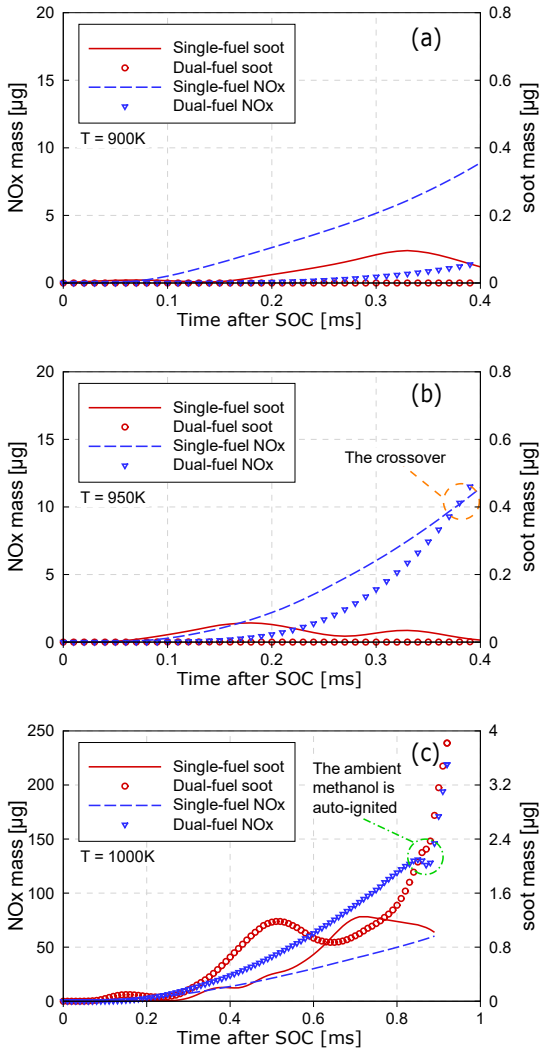

Figure 6.9: Temporal evolution of the total masses of soot and NOx in single- and dual-fuel cases. a) 900 K, cases HR1 and HRB1, b) 950 K, cases HR2 and HRB2, c) 1000 K, cases HR3 and HRB3. Reproduced from Paper II.

6.3.1 n-Heptane and methanol ignition

The methanol/air mixture is assumed to be homogeneous and quiescent before the injection of n-heptane. Figure 6.10 shows the temporal evolution of the intermediate species and temperature under an initial condition of T = 1000 K, P = 4.16 MPa, ϕ_m= 0.3, and O_2 volume fraction of 20.15 %. The auto-ignition of the methanol/air mixture occurs at 1.56 ms.

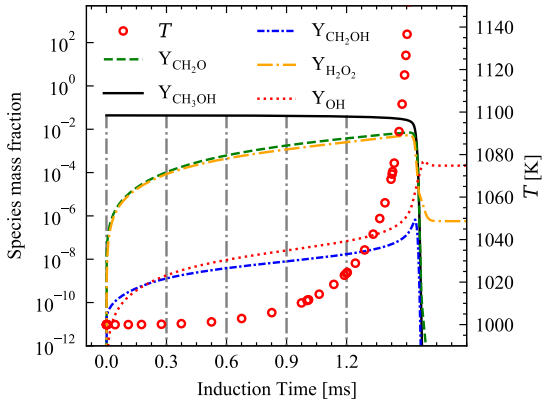

Figure 6.10: The temporal evolution of the key intermediate species and temperature of the ambient methanol/air mixture in the zero-dimension simulation. The rapid increase of temperature at 1.56 ms indicates the auto-ignition of the methanol/air mixture. The vertical lines are the sampled time at 0.3, 0.6, 0.9 and 1.2 ms. Reproduced from Paper III.

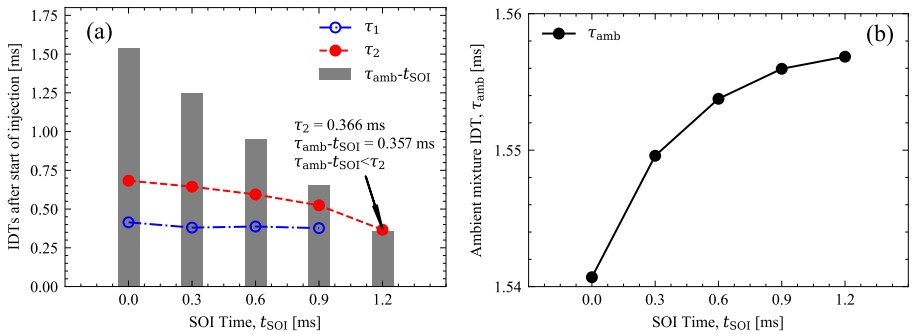

Figure 6.11: a) The two-stage IDTs τ_1 and τ_2 of the spray, and b) The IDT of the ambient mixture τ_{amb} in cases HRC1 to HRC5, with associated SOI times of 0, 0.3, 0.6, 0.9 and 1.2 ms. The color bar in subfigure a) represents the time interval from SOI to the ambient mixture auto-ignition, τ_{amb}-t_{SOI}. Reproduced from Paper III.

By comparing IDT of the ambient methanol/air mixture τ_{amb} in Fig. 6.11, it is found that τ_{amb} is shorten with the addition of the n-heptane spray. τ_{amb} is 1.560 ms without n-heptane spray, while it decreases to 1.540 ms in the case HRC5. On the other hand, only a slight increase of τ_{amb} is observed with the increase of the SOI, e.g. τ_{amb} = 1.540 ms in the 0 ms SOI case and τ_{amb} = 1.557 ms in the 1.2 ms SOI case. This indicates that the methanol auto-ignition is earlier in dual-fuel mode. However, only a minor contribution is provided by the n-heptane spray. The underlying mechanism behind this is investigated in the following section.

The temporal evolution of the spatial integrated chemical HRR is tracked to explain the contribution of the n-heptane to the ambient methanol auto-ignition.

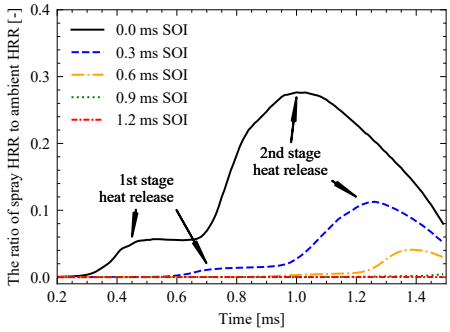

Figure 6.12: The temporal evolution of the ratio $r = \dot{Q}_{spray}/\dot{Q}_{amb}$ in the dual-fuel cases with different SOI. Reproduced from Paper III.

A threshold of mixture fraction $Z = 0.001$ is chosen to separate the HRR of n-heptane spray (denoted as $\dot{Q}_{spray}$) from the total HRR (denoted as $\dot{Q}_{tot}$). $\dot{Q}_{spray}$ is the volume integral chemical HRR within the computational cells of spray, e.g. $Z \geq 0.001$, while HRR of the ambient methanol/air mixture $\dot{Q}_{amb}$ is integrated within the volume of $Z < 0.001$. Figure 6.12 shows the ratio of the tracked $\dot{Q}_{spray}$ and $\dot{Q}_{amb}$ in the dual-fuel cases HRC1 to HRC5. It is evident that the proportion of the HRR from the spray is significantly reduced with the increase of SOI. Also, $\dot{Q}_{spray}$ is much lower than $\dot{Q}_{amb}$ in all of the cases. The maximum $\dot{Q}_{spray}/\dot{Q}_{amb}$ ratio is 0.276 in the 0 ms SOI case, it quickly drops to 0.113 in 0.3 ms SOI and reduces by a factor of 1000 in the 1.2 ms SOI case. The heat source in the ambient mixture auto-ignition is mainly from itself. The heat release effect of the spray on the increasing of the averaged ambient temperature is minor. This explains the minor contribution of the spray on the ambient methanol IDT.

In Fig. 6.12, the ratio of $\dot{Q}_{spray}$ to $\dot{Q}_{amb}$ presents a two-stage growth, especially in the case of 0 ms SOI. Figure 6.13 shows the temporal evolution of HRR from the spray, e.g., $\dot{Q}_{spray}$. Since $\dot{Q}_{spray}$ varies in a wide range before the ignition, a semi-logarithmic coordinate is used to show the HRR clearer. It is seen that $\dot{Q}_{spray}$ in cases HRC1, HRC2, HRC3, and HRC4 reaches two plateaus, which are known as the two-stage heat releases. For instance, in HRC1, the first stage heat release starts shortly after the first stage ignition at $\tau_1 = 0.41$ ms. The second stage heat release occurs at the second stage ignition at $\tau_2 = 0.68$ ms. The transition time from the first stage ignition to the second stage ignition decreases with the increase of SOI. The transition becomes unclear in case HRC5 of SOI 1.2 ms, where the second stage ignition is followed closely to the first stage ignition, and no HRR plateau is observed before the second stage ignition. This indicates that a retarded SOI promotes the n-heptane ignition and reduces its transition time between the first and the second stage ignition.

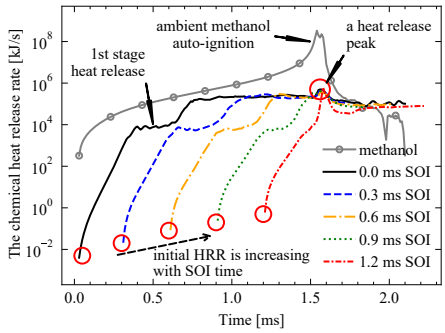

Figure 6.13: The spatial integrated chemical HRR from the spray, $\dot{Q}_{spray}$, in cases HRC1 to HRC5, and evolution of the averaged temperature in the ambient mixture in HRC1. The dots represent the averaged temperature, lines with symbols are the $\dot{Q}_{spray}$. Reproduced from Paper III.

A peak of $\dot{Q}_{spray}$ is observed in all of the dual-fuel cases around 1.55 ms, when the ambient methanol is auto-ignited. Figure 6.14 shows the temporal evolution of the averaged ambient temperature, T_{mean}, and the spray flame LOL in case HRC1. The LOL is defined as the distance from injector to the nearest axial location of Favre-average OH mass fraction reaching 2% of its maximum in the domain after a quasi-steady flame is established. It is seen that the averaged temperature of the ambient mixture increases rapidly after the auto-ignition, reaching 1800 K at 1.55 ms. Meanwhile, the LOL decreases from 22 mm to approximately zero. The auto-ignition of the ambient methanol increases the ambient temperature; thus, the HTC is observed near the nozzle. The unburned n-heptane near the injector nozzle is then ignited, leading to a relatively high HRR, shown as a HRR peak in Fig. 6.13.

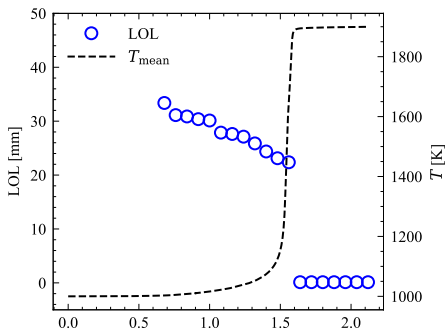

Figure 6.14: The spray flame LOL and the averaged temperature in the ambient mixture in case HRC1. The line is the averaged temperature in the ambient mixture, symbols represent the flame LOL. Reproduced from Paper III.

6.3.2 Species distributions

Figure 6.15 shows the axial distribution of temperature and species mass fractions in cases HRC1 to HRC5 at 0.3, 0.6, and 0.9 ms ASI. Each of the sub-figure is divided into two parts by a vertical line, which represents the corresponding vapour penetration length of n-heptane spray. The n-heptane vapour penetrates to 26, 38 and 47 mm at 0.3, 0.6, and 0.9 ms ASI, respectively. Thus, the n-heptane spray and ambient mixture interaction region fall on the left-hand side of the vertical line, while only methanol/air and its auto-ignition intermediate products on the right-hand side. Due to the presence of n-heptane vapour in the ambient methanol/air mixture, mass fractions of CH_3OH and O_2 decline in the spray and ambient mixture interaction region. Similarly, the temperature in this region decreases due to spray evaporation. In the ambient mixture region, a slight drop of CH_3OH and O_2 is observed at 0.3 ms ASI in HRC4. The temperature in this region increases accordingly, which is more obvious in HRC5. This is due to the methanol/air auto-ignition reactions. Subsequently, CH_3OH is fully consumed and the temperature increases up to 1800 K in the ambient mixture region, which indicates complete combustion of the ambient mixture. For example, the ambient CH_3OH is fully consumed in HRC5 at 0.6 ms ASI and in HRC4 at 0.9 ms ASI.

In the dual-fuel combustion, the cool flame is established after the first stage ignition of the spray, high temperature flame occurs after the high-temperature ignition. The cool flame and high-temperature flame co-exist before the ambient methanol auto-ignition. It is seen in Fig. 6.15 that, at 0.3 ms ASI, RO_2 and CH_2O appear in all cases, indicating that a cool flame is established. The difference is that the RO_2 mass fraction is higher in the retarded SOI case. This difference is rather notable in CH_2O mass fraction, where CH_2O mass fraction at 25 mm is almost 10 times higher than that in the 0 ms SOI case. In addition, a plateau of CH_2O mass fraction is observed after 30 mm downstream the spray axis, which is from the ambient methanol oxidation through the reactions $CH_2OH + O_2 = CH_2O + HO_2$ and $CH_3O + O_2 = CH_2O + HO_2$. In case HRC5 at 0.6 ms ASI, an amount of RO_2 is found further upstream. In the meantime, an absence of CH_2O is found in both the spray region and the ambient mixture, which are consumed in the high-temperature reactions. This indicates that the cool flame disappears in HRC5 at 0.6 ms ASI. A similar phenomenon is found at 0.9 ms ASI as well, where the cool flame disappears and the high-temperature flame is found upstream in both cases HRC5 and HRC4. This is consistent with the findings of LOLs dropping in Fig. 6.14.

In summary, in the delayed SOI cases, an early formation of the high-temperature

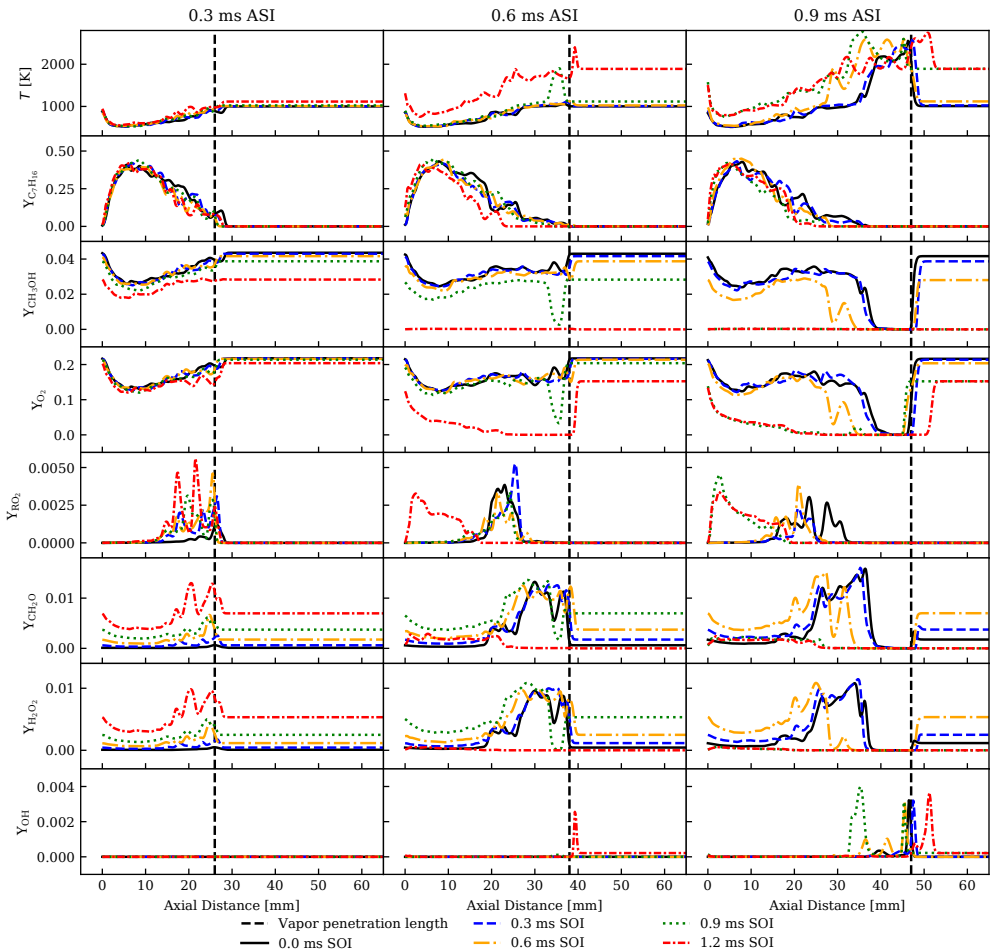

Figure 6.15: The temperature and species mass fraction distribution along the spray axis for cases HRC1 to HRC5 at 0.3, 0.6 and 0.9 ms ASI. Reproduced from Paper III.

flame in the spray region is observed. Once the ambient methanol is ignited, RO_2 is formed further upstream to the injector nozzle, while CH_2O disappears, indicating that the cool flame is eliminated. On the other hand, the LOL of the flame decreases to approximately zero after the ambient methanol auto-ignition. The unburned n-heptane near the injector nozzle is then ignited, leading to a relative high HRR.

Chapter 7

Conclusion and future work

In this chapter, the main works in the thesis are summarized in two aspects: model development and parameter studies. Based on these fundamental studies, application-oriented suggestions for future works are made.

7.1 Conclusion

The turbulent dual-fuel combustion is studied in the present work, which can be categorized into three parts. The first part is focused on the combustion model development. The ESF method is presented, implemented, and examined, showing the capability in predicting both premixed and non-premixed flames in the dual-fuel combustion. The second part clarifies the difference between the single- and dual-fuel combustion, including the two-stage ignitions, low- and high-temperature flame structures. The third part focuses on controlling dual-fuel combustion. Three dual-fuel controlling strategies, primary fuel concentration, ambient temperatures, and injection timings, are discussed.

In the first part, the consistency of the ESF method with respect to the element mass conservation in the simulations of turbulent combustion of multi-species and multi-step chemistry are investigated. A novel correction method is proposed to remove the numerical error in the element mass conservation. This method is based on the three-step factorization scheme and has two correction steps. The first correction step solves an additional mean field. The mass conservation error, which arisen from the Wiener term under a finite number of stochastic fields, is eliminated. The second correction step is proposed to ensure that the mass fraction of each species strictly lies in between zero and one. The

solution procedure is implemented into OpenFOAM (version 7) [99], in which the SPDEs are solved using the finite volume method. It is proven that the modified ESF method not only ensures element mass conservation, but also enhances numerical stability because the potential error from the Wiener term on the mean field is eliminated.

In the second part, LES of single- and dual-fuel combustion are configured based on the n-heptane fueled ECN Spray-H experiments. The turbulence model, TCI model, and other models used in the Lagrangian particle tracking approach are first examined in comparison with the single-fuel experimental data. A good agreement with the measurements is obtained in terms of the flow, combustion and emissions characteristics, such as liquid and vapour penetration lengths, mixture fraction distributions, ignition delay times, lift-off length, pressure rise and soot volume fraction. The performance of the chemical mechanism is then investigated in the prediction of the ignition process in the ambient methanol/air mixture. It is shown that the ignition delay times predicted using the current mechanism are comparable to those calculated using the detailed mechanisms and the shock tube measurement. Finally, the LES models and chemical mechanism are used in the LES of dual-fuel combustion. Results show that:

1. Three stage ignitions, the first- and second-stage n-heptane ignition, τ_1 and τ_2, and the ambient methanol auto-ignition, τ_{amb}, are observed in the dual-fuel combustion. Moreover, it is found that τ_1 and τ_2 are retarded in the dual-fuel cases. The onset of the second-stage ignition kernel is postponed further downstream, resulting in a longer liftoff length in the n-heptane/methanol dual-fuel cases than that of a single fuel n-heptane spray flame. The reaction path in the dual-fuel combustion is identified using a series of homogeneous reactor simulations. It is concluded that the ignition delay time of the n-heptane/methanol dual-fuel combustion is retarded as the OH produced from n-heptane is consumed but cannot be replenished in the ambient mixture. A low OH accumulation rate leads to a longer τ_1, while a low OH mass fraction during the transition period from the first-stage ignition to the second-stage ignition prolongs τ_2.

2. In most cases, the total mass of soot per unit of fuel energy in dual-fuel cases are lower than the single-fuel cases. The results are analyzed from aspects of dilution, mixing and primary fuel combustion to identify the soot emission mechanisms in dual-fuel combustion. It is shown that enhanced mixing is a key factor in soot reduction in the dual-fuel cases. The ignition of n-heptane is retarded in dual-fuel mode. The prolonged ignition delay time extends the mixing time before the start of high-temperature combustion, leading to a low equivalence ratio and thus reducing soot formation.

Effects of oxygen concentration and heat capacity (induced by methanol dilution) on ignition delay time and the maximum flame temperature are not significant in the current dual-fuel configuration.

It is worth mentioning that, in some cases, the increase of soot and NOx is observed in the dual-fuel cases. An inappropriate use of dual-fuel combustion may not be beneficial and may even be counterproductive for engine performance. Therefore, the dual-fuel strategies are studied and discussed in the next part.

In the third part, LESs of dual-fuel combustion under extended conditions are carried out. Different parametric studies are performed to investigate the effects of the dual-fuel operating conditions, including the primary fuel concentration, ambient temperature, and pilot fuel injection timing. It is concluded that:

1. In general, the ambient methanol has an effect of suppressing the two-stage ignition and heat release of n-heptane, this is more significant under high ambient methanol concentration conditions. A longer transition time between the first- and second-stage ignitions, as well as a lower first local peak value of the heat release rate are observed when the ambient methanol concentration increases.

2. The effects of methanol on the n-heptane ignition and NOx formation are strongly dependent on the ambient temperatures. The retardation of the n-heptane high-temperature ignition is more remarkable under low ambient temperatures. The NOx formation rate in the dual-fuel case is lower than that of the single-fuel case in the 900 K case, while an opposite trend of the NOx formation rate is observed in the 1000 K dual-fuel case. In this case, the ambient mixture increases up to 1900 K after its autoignition, which accelerates the n-heptane evaporation and combustion. The high-temperature region with OH radicals propagates upstream. A large NOx formation region is found in the expanded OH zone.

3. The SOI time is an important parameter in the n-heptane/methanol dual-fuel combustion, especially under the ambient methanol auto-ignition conditions. Before the ambient methanol auto-ignition, the axial mass fraction of heptyl-peroxide and formaldehyde are higher in the retarded SOI time case. An early formation of the high-temperature ignition kernel in the spray region is observed in the delayed SOI cases. Moreover, a late SOI may lead to an overlap of the ambient methanol auto-ignition and n-heptane injection, in which the heptyl-peroxide is formed further upstream to the injector nozzle and the cool flame is eliminated. This overlap should be avoided as it results in a high soot and NOx formation.

7.2 Future work

The present thesis shows a fundamental numerical study on dual-fuel combustion. To extend it to the dual-fuel engine simulations, application-oriented suggestions are made.

1. The transported PDF approach coupled with finite rate chemistry has shown its capability on the prediction of the multi-modes combustion process in dual-fuel combustion. However, it is a computationally expensive method, which restricts the simulations of the premixed flame propagation as it has a longer time scale and requires a high mesh resolution. A highly efficient computational method is desirable in practical usage, e.g. engine simulations. In a recent research [155], a tabulated kinetics approach is employed with both Coherent Flame Model (CFM) and Flame Surface Wrinkling Model (FSWM) to achieve time-efficient combustion modelling for dual-fuel combustion. It could be a promising solution to combine the ESF with this novel technique to increase both accuracy and computational efficiency.

2. The present studies are performed in a constant-volume vessel, which replicates the retardation of the ignition, flame structure and pollution emission in the real engine to some extend. The underlying mechanisms are explained based on the simplifications of a homogeneous and quiescent premixed primary fuel-air mixture and an adiabatic wall. However, in the real dual-fuel engine, the stratification, in-cylinder flow, compression and heat loss may play a role. It is suggested that the explained mechanism can be examined in the engine simulations by taking the intake, compression and exhaust strokes into account.

References

[1] T. Poinsot and D. Veynante, *Theoretical and numerical combustion*. RT Edwards, Inc., 2005.

[2] International Energy Agency, *World energy statistics*, `https://www.iea.org/`, 2021.

[3] European Environment Agency, *National emissions report*, `https://www.eea.europa.eu/`, 2021.

[4] C. Le Quéré, R. B. Jackson, M. W. Jones, A. J. Smith, S. Abernethy, R. M. Andrew, A. J. De-Gol, D. R. Willis, Y. Shan, J. G. Canadell *et al.*, 'Temporary reduction in daily global CO 2 emissions during the COVID-19 forced confinement', *Nature Climate Change*, vol. 10, no. 7, pp. 647–653, 2020.

[5] R. J. Pearson, M. D. Eisaman, J. W. Turner, P. P. Edwards, Z. Jiang, V. L. Kuznetsov, K. A. Littau, L. Di Marco and S. G. Taylor, 'Energy Storage via Carbon-Neutral Fuels Made From CO_2, Water, and Renewable Energy', *Proceedings of the IEEE*, vol. 100, no. 2, pp. 440–460, 2011.

[6] T. Chmielniak and M. Sciazko, 'Co-gasification of biomass and coal for methanol synthesis', *Applied Energy*, vol. 74, no. 3-4, pp. 393–403, 2003.

[7] G. A. Olah, 'Beyond oil and gas: the methanol economy', *Angewandte Chemie International Edition*, vol. 44, no. 18, pp. 2636–2639, 2005.

[8] J. Andersson and S. Grönkvist, 'Large-scale storage of hydrogen', *International journal of hydrogen energy*, vol. 44, no. 23, pp. 11 901–11 919, 2019.

[9] J. Andersson, A. Krüger and S. Grönkvist, 'Methanol as a carrier of hydrogen and carbon in fossil-free production of direct reduced iron', *Energy Conversion and Management: X*, vol. 7, p. 100 051, 2020.

[10] T. Wu, A. Yao, C. Yao, W. Pan, H. Wei, C. Chen and J. Gao, 'Effect of diesel late-injection on combustion and emissions characteristics of diesel/methanol dual fuel engine', *Fuel*, vol. 233, pp. 317–327, 2018.

[11] Y. Li, M. Jia, Y. Liu and M. Xie, 'Numerical study on the combustion and emission characteristics of a methanol/diesel reactivity controlled compression ignition (RCCI) engine', *Applied energy*, vol. 106, pp. 184–197, 2013.

[12] W. Tutak, K. Lukacs, S. Szwaja and A. Bereczky, 'Alcohol–diesel fuel combustion in the compression ignition engine', *Fuel*, vol. 154, pp. 196–206, 2015.

[13] S. Verhelst, J. W. Turner, L. Sileghem and J. Vancoillie, 'Methanol as a fuel for internal combustion engines', *Progress in Energy and Combustion Science*, vol. 70, pp. 43–88, 2019.

[14] B. Ma, A. Yao, C. Yao, T. Wu, B. Wang, J. Gao and C. Chen, 'Exergy loss analysis on diesel methanol dual fuel engine under different operating parameters', *Applied Energy*, vol. 261, p. 114 483, 2020.

[15] R. G. Papagiannakis, D. T. Hountalas, C. D. Rakopoulos and D. C. Rakopoulos, 'Combustion and performance characteristics of a DI diesel engine operating from low to high natural gas supplement ratios at various operating conditions', SAE, Tech. Rep. 2008-01-1392, 2008.

[16] J. Liu, F. Yang, H. Wang, M. Ouyang and S. Hao, 'Effects of pilot fuel quantity on the emissions characteristics of a CNG/diesel dual fuel engine with optimized pilot injection timing', *Applied Energy*, vol. 110, pp. 201–206, 2013.

[17] H. Liu, S. Ma, Z. Zhang, Z. Zheng and M. Yao, 'Study of the control strategies on soot reduction under early-injection conditions on a diesel engine', *Fuel*, vol. 139, pp. 472–481, 2015.

[18] B. Sahoo, N. Sahoo and U. Saha, 'Effect of engine parameters and type of gaseous fuel on the performance of dual-fuel gas diesel engines—A critical review', *Renewable and Sustainable Energy Reviews*, vol. 13, no. 6-7, pp. 1151–1184, 2009.

[19] R. B. R. da Costa, R. M. Valle, J. J. Hernández, A. C. T. Malaquias, C. J. Coronado and F. J. P. Pujatti, 'Experimental investigation on the potential of biogas/ethanol dual-fuel spark-ignition engine for power generation: Combustion, performance and pollutant emission analysis', *Applied Energy*, vol. 261, p. 114 438, 2020.

[20] H. Liu, G. Ma, B. Hu, Z. Zheng and M. Yao, 'Effects of port injection of hydrous ethanol on combustion and emission characteristics in dual-fuel reactivity controlled compression ignition (RCCI) mode', *Energy*, vol. 145, pp. 592–602, 2018.

[21] F. Battin-Leclerc, J. M. Simmie and E. Blurock, 'Cleaner combustion', *Developing Detailed Chemical Kinetic Models. Series: Green Energy and Technology. Cham: Springer International Publishing AG*, 2013.

[22] H. F. Coward and G. W. Jones, *Limits of flammability of gases and vapors*. US Government Printing Office, 1952, vol. 503.

[23] S. M. Sarathy, C. K. Westbrook, M. Mehl, W. J. Pitz, C. Togbe, P. Dagaut, H. Wang, M. A. Oehlschlaeger, U. Niemann, K. Seshadri *et al.*, 'Comprehensive chemical kinetic modeling of the oxidation of 2-methylalkanes from C7 to C20', *Combustion and flame*, vol. 158, no. 12, pp. 2338–2357, 2011.

[24] F. Battin-Leclerc, 'Detailed chemical kinetic models for the low-temperature combustion of hydrocarbons with application to gasoline and diesel fuel surrogates', *Progress in Energy and Combustion Science*, vol. 34, no. 4, pp. 440–498, 2008.

[25] J. Zádor, C. A. Taatjes and R. X. Fernandes, 'Kinetics of elementary reactions in low-temperature autoignition chemistry', *Progress in energy and combustion science*, vol. 37, no. 4, pp. 371–421, 2011.

[26] S. Hu, *Combustion characteristics of some alternative fuels in ICE: a detailed numerical study*. Lund University, 2017.

[27] T. Lu, C. K. Law, C. S. Yoo and J. H. Chen, 'Dynamic stiffness removal for direct numerical simulations', *Combustion and Flame*, vol. 156, no. 8, pp. 1542–1551, 2009.

[28] S. L. Kokjohn, R. M. Hanson, D. A. Splitter and R. D. Reitz, 'Experiments and modeling of dual-fuel HCCI and PCCI combustion using in-cylinder fuel blending', *SAE International Journal of Engines*, vol. 2, no. 2, pp. 24–39, 2010.

[29] D. Splitter, S. Kokjohn, K. Rein, R. Hanson, S. Sanders and R. Reitz, 'An optical investigation of ignition processes in fuel reactivity controlled PCCI combustion', *SAE International Journal of Engines*, vol. 3, no. 1, pp. 142–162, 2010.

[30] S. Kokjohn, R. Hanson, D. Splitter, J. Kaddatz and R. Reitz, 'Fuel reactivity controlled compression ignition (RCCI) combustion in light-and heavy-duty engines', *SAE International Journal of Engines*, vol. 4, no. 1, pp. 360–374, 2011.

[31] A. B. Dempsey, N. R. Walker and R. Reitz, 'Effect of piston bowl geometry on dual fuel reactivity controlled compression ignition (RCCI) in a light-duty engine operated with gasoline/diesel and methanol/diesel', *SAE International Journal of Engines*, vol. 6, no. 1, pp. 78–100, 2013.

[32] R. Seiser, K. Seshadri and F. A. Williams, 'Detailed and reduced chemistry for methanol ignition', *Combustion and flame*, vol. 158, no. 9, pp. 1667–1672, 2011.

[33] S. Yalamanchili, W. Sirignano, R. Seiser and K. Seshadri, 'Reduced methanol kinetic mechanisms for combustion applications', *Combustion and flame*, vol. 142, no. 3, pp. 258–265, 2005.

[34] C. Olm, T. Varga, É. Valkó, H. J. Curran and T. Turányi, 'Uncertainty quantification of a newly optimized methanol and formaldehyde combustion mechanism', *Combustion and Flame*, vol. 186, pp. 45–64, 2017.

[35] N. Grumman, 'Diesel fuel oils, 2003', *Report NGMS-232 PPS*, 2004.

[36] W. J. Pitz and C. J. Mueller, 'Recent progress in the development of diesel surrogate fuels', *Progress in Energy and Combustion Science*, vol. 37, no. 3, pp. 330–350, 2011.

[37] A. Patel, S.-C. Kong and R. D. Reitz, 'Development and validation of a reduced reaction mechanism for HCCI engine simulations', SAE Technical Paper, Tech. Rep. 2004-01-0558, 2004.

[38] S. national laboratories, *Engine combustion network*, `https://ecn.sandia.gov`, 2021.

[39] C. Gong, M. Jangi and X.-S. Bai, 'Large eddy simulation of n-dodecane spray combustion in a high pressure combustion vessel', *Applied Energy*, vol. 136, pp. 373–381, 2014.

[40] S. Ma, Z. Zheng, H. Liu, Q. Zhang and M. Yao, 'Experimental investigation of the effects of diesel injection strategy on gasoline/diesel dual-fuel combustion', *Applied Energy*, vol. 109, pp. 202–212, 2013.

[41] X. Kan, L. Wei, X. Li, H. Li, D. Zhou, W. Yang and C.-H. Wang, 'Effects of the three dual-fuel strategies on performance and emissions of a biodiesel engine', *Applied Energy*, vol. 262, p. 114 542, 2020.

[42] Z. Zhang, K. Tsang, C. Cheung, T. Chan and C. Yao, 'Effect of fumigation methanol and ethanol on the gaseous and particulate emissions of a direct-injection diesel engine', *Atmospheric Environment*, vol. 45, no. 11, pp. 2001–2008, 2011.

[43] Q. Tang, H. Liu, X. Ran, M. Li and M. Yao, 'Effects of direct-injection fuel types and proportion on late-injection reactivity controlled compression ignition', *Combustion and Flame*, vol. 211, pp. 445–455, 2020.

[44] Q. Tang, X. Liu, H. Liu, H. Wang and M. Yao, 'Investigation on the dual-fuel active-thermal atmosphere combustion strategy based on optical diagnostics and numerical simulations', *Fuel*, vol. 276, p. 118 023, 2020.

[45] J. O'Connor and M. Musculus, 'Post injections for soot reduction in diesel engines: a review of current understanding', *SAE International Journal of Engines*, vol. 6, no. 1, pp. 400–421, 2013.

[46] S. Imran, D. Emberson, A. Diez, D. Wen, R. Crookes and T. Korakianitis, 'Natural gas fueled compression ignition engine performance and emissions maps with diesel and RME pilot fuels', *Applied Energy*, vol. 124, pp. 354–365, 2014.

[47] R. Papagiannakis and D. Hountalas, 'Experimental investigation concerning the effect of natural gas percentage on performance and emissions of a DI dual fuel diesel engine', *Applied Thermal Engineering*, vol. 23, no. 3, pp. 353–365, 2003.

[48] H. Liu, Q. Tang, Z. Yang, X. Ran, C. Geng, B. Chen, L. Feng and M. Yao, 'A comparative study on partially premixed combustion (PPC) and reactivity controlled compression ignition (RCCI) in an optical engine', *Proceedings of the Combustion Institute*, vol. 37, no. 4, pp. 4759–4766, 2019.

[49] H. Kahila, A. Wehrfritz, O. Kaario and V. Vuorinen, 'Large-eddy simulation of dual-fuel ignition: Diesel spray injection into a lean methane-air mixture', *Combustion and Flame*, vol. 199, pp. 131–151, 2019.

[50] H. Kahila, O. Kaario, Z. Ahmad, M. G. Masouleh, B. Tekgül, M. Larmi and V. Vuorinen, 'A large-eddy simulation study on the influence of diesel pilot spray quantity on methane-air flame initiation', *Combustion and Flame*, vol. 206, pp. 506–521, 2019.

[51] B. Tekgül, H. Kahila, O. Kaario and V. Vuorinen, 'Large-eddy simulation of dual-fuel spray ignition at different ambient temperatures', *Combustion and Flame*, vol. 215, pp. 51–65, 2020.

[52] D. C. Haworth, 'Progress in probability density function methods for turbulent reacting flows', *Progress in Energy and Combustion Science*, vol. 36, no. 2, pp. 168–259, 2010.

[53] E. Garnier, N. Adams and P. Sagaut, *Large eddy simulation for compressible flows*. Springer Science & Business Media, 2009.

[54] A. Yoshizawa and K. Horiuti, 'A statistically-derived subgrid-scale kinetic energy model for the large-eddy simulation of turbulent flows', *Journal of the Physical Society of Japan*, vol. 54, no. 8, pp. 2834–2839, 1985.

[55] S. Menon, 'Subgrid combustion modelling for large-eddy simulations', *International Journal of Engine Research*, vol. 1, no. 2, pp. 209–227, 2000.

[56] S. B. Pope, *Turbulent flows*. Cambridge: Cambridge Univ. Press, 2000.

[57] W. E. Ranz and W. R. Marshall, 'Evaporation from drops, Part I', *Chem. Eng. Prog*, vol. 48, no. 3, pp. 141–146, 1952.

[58] ——, 'Evaporation from drops, Part II', *Chem. Eng. Prog*, vol. 48, no. 3, pp. 173–180, 1952.

[59] D. B. Spalding, 'The combustion of liquid fuels', in *Symposium (international) on combustion*, vol. 4, 1953, pp. 847–864.

[60] A. Varna, A. Wehrfritz, E. R. Hawkes, M. J. Cleary, T. Lucchini, G. D'Errico, S. Kook and Q. N. Chan, 'Application of a multiple mapping conditioning mixing model to ECN Spray A', *Proceedings of the Combustion Institute*, vol. 37, no. 3, pp. 3263–3270, 2019.

[61] C. K. Blomberg, L. Zeugin, S. S. Pandurangi, M. Bolla, K. Boulouchos and Y. M. Wright, 'Modeling split injections of ECN "Spray A" using a conditional moment closure combustion model with RANS and LES', *SAE International Journal of Engines*, vol. 9, no. 4, pp. 2107–2119, 2016.

[62] S. Gallot-Lavallée and W. Jones, 'Large eddy simulation of spray autoignition under EGR conditions', *Flow, Turbulence and Combustion*, vol. 96, no. 2, pp. 513–534, 2016.

[63] H. Wei, W. Zhao, J. Qi, Z. Liu and L. Zhou, 'Effect of injection timing on the ignition process of n-heptane spray flame in a methane/air environment', *Fuel*, vol. 245, pp. 345–359, 2019.

[64] W. Zhao, H. Wei, M. Jia, Z. Lu, K. H. Luo, R. Chen and L. Zhou, 'Flame–spray interaction and combustion features in split-injection spray flames under diesel engine-like conditions', *Combustion and Flame*, vol. 210, pp. 204–221, 2019.

[65] A. Wehrfritz, O. Kaario, V. Vuorinen and B. Somers, 'Large eddy simulation of n-dodecane spray flames using flamelet generated manifolds', *Combustion and Flame*, vol. 167, pp. 113–131, 2016.

[66] K. M. Pang, M. Jangi, X.-S. Bai, J. Schramm and J. H. Walther, 'Modelling of diesel spray flames under engine-like conditions using an accelerated Eulerian Stochastic Field method', *Combustion and Flame*, vol. 193, pp. 363–383, 2018.

[67] S. Som, D. E. Longman, Z. Luo, M. Plomer, T. Lu, P. K. Senecal and E. Pomraning, 'Simulating flame lift-off characteristics of diesel and biodiesel fuels using detailed chemical-kinetic mechanisms and large eddy simulation turbulence model', *Journal of Energy Resources Technology*, vol. 134, no. 3, p. 032 204, 2012.

[68] A. Irannejad, A. Banaeizadeh and F. Jaberi, 'Large eddy simulation of turbulent spray combustion', *Combustion and Flame*, vol. 162, no. 2, pp. 431–450, 2015.

[69] C.-W. Tsang, Y. Wang, C. Wang, A. Shelburn, L. Liang, K. Puduppakkam, A. Modak, C. Naik, E. Meeks and C. Rutland, 'Evaluation and Validation of Large-Eddy-Simulation (LES) for Gas Jet and Sprays', SAE Technical Paper, Tech. Rep. 2017-01-0844, 2017.

[70] Y. Pei, S. Som, E. Pomraning, P. K. Senecal, S. A. Skeen, J. Manin and L. M. Pickett, 'Large eddy simulation of a reacting spray flame with multiple realizations under compression ignition engine conditions', *Combustion and Flame*, vol. 162, no. 12, pp. 4442–4455, 2015.

[71] P. Kundu, M. M. Ameen and S. Som, 'Importance of turbulence-chemistry interactions at low temperature engine conditions', *Combustion and Flame*, vol. 183, pp. 283–298, 2017.

[72] A. Hadadpour, M. Jangi, K. M. Pang and X. S. Bai, 'The role of a split injection strategy in the mixture formation and combustion of diesel spray: A large-eddy simulation', *Proceedings of the Combustion Institute*, vol. 37, no. 4, pp. 4709–4716, 2019.

[73] G. D'Errico, T. Lucchini, F. Contino, M. Jangi and X.-S. Bai, 'Comparison of well-mixed and multiple representative interactive flamelet approaches for diesel spray combustion modelling', *Combustion Theory and Modelling*, vol. 18, no. 1, pp. 65–88, 2014.

[74] K. E. Niemeyer, N. J. Curtis and C.-J. Sung, 'pyJac: Analytical Jacobian generator for chemical kinetics', *Computer Physics Communications*, vol. 215, pp. 188–203, 2017.

[75] P. Senecal, E. Pomraning, K. Richards, T. Briggs, C. Choi, R. McDavid and M. Patterson, 'Multi-dimensional modeling of direct-injection diesel spray liquid length and flame lift-off length using CFD and parallel detailed chemistry', SAE Technical Paper, Tech. Rep. 2003-01-1043, 2003.

[76] F. Contino, H. Jeanmart, T. Lucchini and G. D'Errico, 'Coupling of in situ adaptive tabulation and dynamic adaptive chemistry: An effective method for solving combustion in engine simulations', *Proceedings of the Combustion Institute*, vol. 33, no. 2, pp. 3057–3064, 2011.

[77] X. Yang, A. Solomon and T.-W. Kuo, 'Ignition and combustion simulations of spray-guided SIDI engine using Arrhenius combustion with spark-energy deposition model', SAE Technical Paper, Tech. Rep. 2012-01-0147, 2012.

[78] B. Tekgül, H. Kahila, O. Kaario and V. Vuorinen, 'Large-eddy simulation of dual-fuel spray ignition at different ambient temperatures', *Combustion and Flame*, vol. 215, pp. 51–65, 2020.

[79] C. Gong, M. Jangi, T. Lucchini, G. D'Errico and X.-S. Bai, 'Large eddy simulation of air entrainment and mixing in reacting and non-reacting diesel sprays', *Flow, turbulence and combustion*, vol. 93, no. 3, pp. 385–404, 2014.

[80] J. Chomiak and A. Karlsson, 'Flame liftoff in diesel sprays', *Symposium (International) on Combustion*, vol. 26, no. 2, pp. 2557–2564, 1996.

[81] S. B. Pope, 'PDF methods for turbulent reactive flows', *Progress in energy and combustion science*, vol. 11, no. 2, pp. 119–192, 1985.

[82] S. B. Pope, 'Small scales, many species and the manifold challenges of turbulent combustion', *Proceedings of the Combustion Institute*, vol. 34, no. 1, pp. 1–31, 2013.

[83] H. Wang, M. Juddoo, S. H. Starner, A. R. Masri and S. B. Pope, 'A novel transient turbulent jet flame for studying turbulent combustion', *Proceedings of the Combustion Institute*, vol. 34, no. 1, pp. 1251–1259, 2013.

[84] A. Masri, R. Cao, S. Pope and G. Goldin, 'PDF calculations of turbulent lifted flames of H˜ 2/N˜ 2 fuel issuing into a vitiated co-flow', *Combustion Theory and Modelling*, vol. 8, no. 1, pp. 1–22, 2004.

[85] R. R. Cao, S. B. Pope and A. R. Masri, 'Turbulent lifted flames in a vitiated coflow investigated using joint PDF calculations', *Combustion and Flame*, vol. 142, no. 4, pp. 438–453, 2005.

[86] C. Heye, V. Raman and A. R. Masri, 'Influence of spray/combustion interactions on auto-ignition of methanol spray flames', *Proceedings of the Combustion Institute*, vol. 35, no. 2, pp. 1639–1648, 2015.

[87] W. Jones and S. Navarro-Martinez, 'Large eddy simulation of autoignition with a subgrid probability density function method', *Combust. Flame*, vol. 150, pp. 170–187, 2007.

[88] L. Valiño, 'A field Monte Carlo formulation for calculating the probability density function of a single scalar in a turbulent flow', *Flow, turbulence and combustion*, vol. 60, no. 2, pp. 157–172, 1998.

[89] Y. B. Zeldovich, *Selected Works of Yakov Borisovich Zeldovich, Volume I: Chemical Physics and Hydrodynamics*. Princeton University Press, 2014.

[90] F. S. Mirhashemi and H. Sadrnia, 'NOx emissions of compression ignition engines fueled with various biodiesel blends: A review', *Journal of the Energy Institute*, vol. 93, no. 1, pp. 129–151, 2020.

[91] K. Mollenhauer and H. Tschoke, *Handbook of diesel engines*. Springer Berlin, 2010, vol. 1.

[92] Y. Li, M. Jia, Y. Chang, W. Fan, M. Xie and T. Wang, 'Evaluation of the necessity of exhaust gas recirculation employment for a methanol/diesel reactivity controlled compression ignition engine operated at medium loads', *Energy Conversion and Management*, vol. 101, pp. 40–51, 2015.

[93] K. M. Leung, R. P. Lindstedt and W. Jones, 'A simplified reaction mechanism for soot formation in nonpremixed flames', *Combustion and flame*, vol. 87, no. 3-4, pp. 289–305, 1991.

[94] K. M. Pang, M. Jangi, X.-S. Bai and J. Schramm, 'Evaluation and optimisation of phenomenological multi-step soot model for spray combustion under diesel engine-like operating conditions', *Combustion Theory and Modelling*, vol. 19, no. 3, pp. 279–308, 2015.

[95] H. G. Weller, G. Tabor, H. Jasak and C. Fureby, 'A tensorial approach to computational continuum mechanics using object-oriented techniques', *Computers in Physics*, vol. 12, no. 6, p. 620, 1998, ISSN: 08941866.

[96] G. Wanner and E. Hairer, *Solving ordinary differential equations II*. Springer Berlin Heidelberg, 1996.

[97] M. Jangi and X.-S. Bai, 'Multidimensional chemistry coordinate mapping approach for combustion modelling with finite-rate chemistry', *Combustion Theory and Modelling*, vol. 16, no. 6, pp. 1109–1132, 2012.

[98] R. Solsjö, M. Jangi, C. Chartier, Ö. Andersson and X.-S. Bai, 'Lift-off and stabilization of n-heptane combustion in a diesel engine with a multiple-nozzle injection', *Proceedings of the Combustion Institute*, vol. 34, no. 2, pp. 3031–3038, 2013.

[99] The OpenFOAM Foundation, *OpenFOAM*, `https://www.openfoam.gov`, 2021.

[100] H. Wang, P. Zhang and T. Pant, 'Consistency and convergence of Eulerian Monte Carlo field method for solving transported probability density function equation in turbulence modeling', *Physics of Fluids*, vol. 30, no. 11, p. 115 106, 2018.

[101] C. Zhen and X. Zhou, *The PDF simulation of the turbulent reacting flow*. Huazhong University of Science & Technology Press, 2005.

[102] V. Sabel'nikov and O. Soulard, 'Rapidly decorrelating velocity-field model as a tool for solving one-point Fokker-Planck equations for probability density functions of turbulent reactive scalars', *Physical Review E*, vol. 72, no. 1, p. 016 301, 2005.

[103] L. Valiño, R. Mustata and K. B. Letaief, 'Consistent behavior of Eulerian Monte Carlo fields at low Reynolds numbers', *Flow, Turbulence and Combustion*, vol. 96, no. 2, pp. 503–512, 2016.

[104] H. Wang, 'Fully consistent Eulerian Monte Carlo fields method for solving probability density function transport equations in turbulence modeling', *Physics of Fluids*, vol. 33, no. 1, p. 015 118, 2021.

[105] T. Pant, U. Jain and H. Wang, 'Transported PDF modeling of compressible turbulent reactive flows by using the Eulerian Monte Carlo fields method', *Journal of Computational Physics*, vol. 425, p. 109 899, 2020.

[106] A. Avdić, G. Kuenne, F. di Mare and J. Janicka, 'LES combustion modeling using the Eulerian stochastic field method coupled with tabulated chemistry', *Combustion and Flame*, vol. 175, pp. 201–219, 2017.

[107] V. N. Prasad, 'Large eddy simulation of partially premixed turbulent combustion', Ph.D. dissertation, Imperial College London (University of London), 2011.

[108] A. Garmory, 'Micromixing effects in atmospheric reacting flows', Ph.D. dissertation, University of Cambridge, 2008.

[109] T. Pant, U. Jain and H. Wang, 'Transported PDF Modeling of Compressible Turbulent Reactive Flows by using the Eulerian Monte Carlo Fields Method', *Journal of Computational Physics*, p. 109 899, 2020.

[110] W. Jones, A. Marquis and V. Prasad, 'LES of a turbulent premixed swirl burner using the Eulerian stochastic field method', *Combust. Flame*, vol. 159, pp. 3079–3095, 2012.

[111] W. Jones and V. Prasad, 'LES-PDF simulation of a spark ignited turbulent methane jet', *Proc. Combust. Inst.*, vol. 33, pp. 1355–1363, 2011.

[112] T. Nilsson, 'Direct numerical simulation of turbulent premixed flames at high Karlovitz numbers: structure and modelling', eng, Ph.D. dissertation, Lund University, 2019, ISBN: 978-91-7895-110-9.

[113] T. Nilsson, I. Langella, N. A. K. Doan, N. Swaminathan, R. Yu and X.-S. Bai, 'A priori analysis of sub-grid variance of a reactive scalar using DNS data of high Ka flames', *Combustion Theory and Modelling*, vol. 23, no. 5, pp. 885–906, 2019.

[114] B. Franzelli, E. Riber, L. Y. Gicquel and T. Poinsot, 'Large eddy simulation of combustion instabilities in a lean partially premixed swirled flame', *Combustion and flame*, vol. 159, no. 2, pp. 621–637, 2012.

[115] E. Mastorakos, 'Turbulent combustion in opposed jet flows', Ph.D. thesis, Imperial College London, 1993.

[116] H. Chelliah, C. K. Law, T. Ueda, M. Smooke and F. Williams, 'An experimental and theoretical investigation of the dilution, pressure and flow-field effects on the extinction condition of methane-air-nitrogen diffusion flames', *Symp. (Int.) on Combustion*, vol. 23, pp. 503–511, 1991.

[117] J. S. Park, D. J. Hwang, J. Park, J. S. Kim, S. Kim, S. I. Keel, T. K. Kim and D. S. Noh, 'Edge flame instability in low-strain-rate counterflow diffusion flames', *Combust. Flame*, vol. 146, pp. 612–619, 2006.

[118] M. D. Smooke, *Reduced kinetic mechanisms and asymptotic approximations for methane-air flames. In: Lecture Notes in Physics book series (LNP, volume 384)*. Springer, 1991.

[119] S. Yu, X. Liu, X. Bai, A. M. Elbaz and W. L. Roberts, 'LES/PDF modeling of swirl-stabilized non-premixed methane/air flames with local extinction and re-ignition', *Combust. Flame*, vol. 219, pp. 102–119, 2020.

[120] F. Mauß, D. Keller and N. Peters, 'A lagrangian simulation of flamelet extinction and re-ignition in turbulent jet diffusion flames', *Symp. (Int.) on Combustion*, vol. 23, pp. 693–698, 1991.

[121] E. Mastorakos, A. Taylor and J. Whitelaw, 'Extinction and temperature characteristics of turbulent counterflow diffusion flames with partial premixing', *Combust. Flame*, vol. 91, pp. 40–54, 1992.

[122] ——, 'Extinction of turbulent counterflow flames with reactants diluted by hot products', *Combust. Flame*, vol. 102, pp. 101–114, 1995.

[123] K. Seshadri and N. Peters, 'Asymptotic structure and extinction of methane/air diffusion flames', *Combust. Flame*, vol. 73, pp. 23–44, 1988.

[124] K. Seshadri and X. Bai, 'Rate-ratio asymptotic analysis of the structure and extinction of partially premixed flames', *Proc. Combust. Inst.*, vol. 31, pp. 1181–1188, 2007.

[125] S. Lapointe, K. Zhang and M. McNenly, 'Reduced chemical model for low and high-temperature oxidation of fuel blends relevant to internal combustion engines', *Proceedings of the Combustion Institute*, vol. 37, no. 1, pp. 789–796, 2019.

[126] C.-W. Zhou, Y. Li, E. O'Connor, K. P. Somers, S. Thion, C. Keesee, O. Mathieu, E. L. Petersen, T. A. DeVerter, M. A. Oehlschlaeger *et al.*, 'A comprehensive experimental and modeling study of isobutene oxidation', *Combustion and Flame*, vol. 167, pp. 353–379, 2016.

[127] L. M. Pickett, C. L. Genzale, G. Bruneaux, L.-M. Malbec, L. Hermant, C. Christiansen and J. Schramm, 'Comparison of diesel spray combustion in different high-temperature, high-pressure facilities', *SAE International Journal of Engines*, vol. 3, no. 2, pp. 156–181, 2010.

[128] F. Payri, J. M. García-Oliver, R. Novella and E. J. Pérez-Sánchez, 'Influence of the n-dodecane chemical mechanism on the CFD modelling of the diesel-like ECN Spray A flame structure at different ambient conditions', *Combustion and Flame*, vol. 208, pp. 198–218, 2019.

[129] T. Yao, Y. Pei, B.-J. Zhong, S. Som, T. Lu and K. H. Luo, 'A compact skeletal mechanism for n-dodecane with optimized semi-global low-temperature chemistry for diesel engine simulations', *Fuel*, vol. 191, pp. 339–349, 2017.

[130] D. K. Dalakoti, B. Savard, E. R. Hawkes, A. Wehrfritz, H. Wang, M. S. Day and J. B. Bell, 'Direct numerical simulation of a spatially developing n-dodecane jet flame under Spray A thermochemical conditions: Flame structure and stabilisation mechanism', *Combustion and Flame*, vol. 217, pp. 57–76, 2020.

[131] S. Lapointe, S. Mondal and R. A. Whitesides, 'Data-driven selection of stiff chemistry ODE solver in operator-splitting schemes', *Combustion and Flame*, vol. 220, pp. 133–143, 2020.

[132] H. S. Sim, N. Maes, L. Weiss, L. M. Pickett and S. A. Skeen, 'Detailed measurements of transient two-stage ignition and combustion processes in high-pressure spray flames using simultaneous high-speed formaldehyde PLIF and schlieren imaging', *Proceedings of the Combustion Institute*, 2020.

[133] S. Xu, S. Zhong, K. M. Pang, S. Yu, M. Jangi and X.-s. Bai, 'Effects of ambient methanol on pollutants formation in dual-fuel spray combustion at varying ambient temperatures: A large-eddy simulation', *Applied Energy*, vol. 279, p. 115 774, 2020.

[134] Y. Zhang, S. Xu, S. Zhong, X.-S. Bai, H. Wang and M. Yao, 'Large eddy simulation of spray combustion using flamelet generated manifolds combined with artificial neural networks', *Energy and AI*, p. 100 021, 2020.

[135] S. Hu, C. Gong and X.-S. Bai, 'Dual Fuel Combustion of N-heptane/methanol-air-EGR Mixtures', *Energy Procedia*, vol. 105, pp. 4943–4948, 2017.

[136] L. Xu, X.-S. Bai, M. Jia, Y. Qian, X. Qiao and X. Lu, 'Experimental and modeling study of liquid fuel injection and combustion in diesel engines with a common rail injection system', *Applied Energy*, vol. 230, pp. 287–304, 2018.

[137] R. REITZ *et al.*, 'Modeling atomization processes in high-pressure vaporizing sprays', *Atomisation and Spray Technology*, vol. 3, no. 4, pp. 309–337, 1987.

[138] J. C. Beale and R. D. Reitz, 'Modeling spray atomization with the Kelvin-Helmholtz/Rayleigh-Taylor hybrid model', *Atomization and sprays*, vol. 9, no. 6, 1999.

[139] L. M. Ricart, R. D. Reltz and J. E. Dec, 'Comparisons of diesel spray liquid penetration and vapor fuel distributions with in-cylinder optical measurements', *Journal of Engineering for gas turbines and power*, vol. 122, no. 4, pp. 588–595, 2000.

[140] M. Jangi, R. Solsjo, B. Johansson and X.-S. Bai, 'On large eddy simulation of diesel spray for internal combustion engines', *International Journal of Heat and Fluid Flow*, vol. 53, pp. 68–80, 2015.

[141] L. Bravo and C.-B. Kweon, 'A review on liquid spray models for diesel engine computational analysis', United States Army Research Laboratory Technical Report, Tech. Rep., 2014.

[142] Y. Zhang, M. Jia, H. Liu, M. Xie, T. Wang and L. Zhou, 'Development of a new spray/wall interaction model for diesel spray under PCCI-engine relevant conditions', *Atomization and sprays*, vol. 24, no. 1, pp. 41–80, 2014.

[143] L. Xu, X.-S. Bai, C. Li, P. Tunestål, M. Tunér and X. Lu, 'Combustion characteristics of gasoline DICI engine in the transition from HCCI to PPC: Experiment and numerical analysis', *Energy*, vol. 185, pp. 922–937, 2019.

[144] U. Burke, W. K. Metcalfe, S. M. Burke, K. A. Heufer, P. Dagaut and H. J. Curran, 'A detailed chemical kinetic modeling, ignition delay time and jet-stirred reactor study of methanol oxidation', *Combustion and Flame*, vol. 165, pp. 125–136, 2016.

[145] Combustion Chemistry Centre, *National University of Ireland Galway*, `http://c3.nuigalway.ie/combustionchemistrycentre`, 2021.

[146] M. Christensen, E. Nilsson and A. Konnov, 'A systematically updated detailed kinetic model for CH2O and CH3OH combustion', *Energy & Fuels*, vol. 30, no. 8, pp. 6709–6726, 2016.

[147] H. Xu, C. Yao and G. Xu, 'Chemical kinetic mechanism and a skeletal model for oxidation of n-heptane/methanol fuel blends', *Fuel*, vol. 93, pp. 625–631, 2012.

[148] C. K. Westbrook, 'Chemical kinetics of hydrocarbon ignition in practical combustion systems', *Proceedings of the combustion institute*, vol. 28, no. 2, pp. 1563–1577, 2000.

[149] K. Ryu, 'Effects of pilot injection timing on the combustion and emissions characteristics in a diesel engine using biodiesel–CNG dual fuel', *Applied Energy*, vol. 111, pp. 721–730, 2013.

[150] Z. Chen, C. Yao, A. Yao, Z. Dou, B. Wang, H. Wei, M. Liu, C. Chen and J. Shi, 'The impact of methanol injecting position on cylinder-to-cylinder variation in a diesel methanol dual fuel engine', *Fuel*, vol. 191, pp. 150–163, 2017.

[151] J. Shen, J. Qin and M. Yao, 'Turbocharged diesel/CNG dual-fuel engines with intercooler: combustion, emissions and performance', SAE Technical Paper, Tech. Rep. 2003-01-3082, 2003.

[152] M. T. Chaichan, 'Performance and emission characteristics of CIE using hydrogen, biodiesel, and massive EGR', *International Journal of Hydrogen Energy*, vol. 43, no. 10, pp. 5415–5435, 2018.

[153] M. Mehl, W. J. Pitz, C. K. Westbrook, K. Yasunaga, C. Conroy and H. J. Curran, 'Autoignition behavior of unsaturated hydrocarbons in the low and high temperature regions', *Proceedings of the Combustion Institute*, vol. 33, no. 1, pp. 201–208, 2011.

[154] Q. Wang, C. Yao, Z. Dou, B. Wang and T. Wu, 'Effect of intake preheating and injection timing on combustion and emission characteristics of a methanol fumigated diesel engine at part load', *Fuel*, vol. 159, pp. 796–802, 2015.

[155] G. Decan, T. Lucchini, G. D'Errico and S. Verhelst, 'A novel technique for detailed and time-efficient combustion modeling of fumigated dual-fuel internal combustion engines', *Applied Thermal Engineering*, vol. 174, p. 115 224, 2020.

Summary of Publications

Author contributions

Co-authors are abbreviated as follows:
Shijie Xu (SX), Xue-Song Bai (XB), Shenghui Zhong (SZ), Kar Mun Pang (KP), Ahmad Hadadpour (AH), Yan Zhang (YZ), Yaopeng Li (YL), Senbin Yu (SY), Fan Zhang (FZ), Mehdi Jangi (MJ).

Paper I: LES/TPDF investigation of the effects of ambient methanol concentration on pilot fuel ignition characteristics and reaction front structures.

The candidate (SX) carried out the numerical simulations, data post-processing and analysis, and wrote the manuscript. The candidate received assistance from XB and KP while writing the paper. The manuscript was revised by XB, KP, YL and SY. The solver is originally developed by MJ, improved by SZ. The case was set up by SX based on AH's configurations. Rui Li provided assistance in the chemical reaction path analysis. All simulations, analysis and writing processes were done with the collaboration, supervision and support of the supervisor (XB).

Paper II: Effects of ambient methanol on pollutants formation in dual-fuel spray combustion at varying ambient temperatures: A large-eddy simulation.

The candidate (SX) carried out the numerical simulations, data post-processing and analysis, and wrote the manuscript. SZ tested the solver performance under different configurations. KP provided suggestions and discussions on the soot

modelling. The manuscript was written by the candidate, revised by XB, KP and SY. All simulations, analysis and writing processes were done with the collaboration, supervision and support of the supervisor (XB).

Paper III: Large-eddy simulation of the injection timing effects on the dual-fuel spray flame.

Shijie Xu, Shenghui Zhong, Ahmad Hadadpour, Yan Zhang, Kar Mun Pang, Mehdi Jangi, Xue-Song Bai*.The candidate (SX) set up the cases, performed the numerical simulation and post-processing, analysed the results and wrote the paper. SZ, YZ and AH contributed to the code development, and results discussions. The manuscript was written by the candidate, revised by KP and XB. All simulations, analysis and writing processes were done with the collaboration, supervision and support of XB and KP.

Paper IV: On the element mass conservation in Eulerian stochastic field modelling of turbulent combustion.

The candidate (SX) set up the cases, performed the numerical simulation and post-processing, analysed the results and wrote the paper. The topic selection is done by XB. The case setup is suggested by SX while the solution is originally suggested by SZ. SZ and SX finished the code development together. The paper is written under the assistance of XB, revised by XB, SZ and FZ. All simulations, analysis and writing processes were done with the collaboration, supervision and support of the supervisor (XB).

Paper V: Effects of pre-injection on ignition, combustion and emissions of spray under engine-like conditions.

The candidate (SX) provided the soot modelling and discussion. AH developed a code for FGM database generation, carried out the simulations. The manuscript was written by AH, revised by KP, SX, MJ and XB. All simulations, analysis and writing processes were done with the collaboration, supervision and support of the supervisors (MJ and XB).